Analysis of the ultra-peripheral events in heavy-ion collisions in the CMS experiment at the Large Hadron Collider

Marek Walczak
University of Warsaw

Doctoral Thesis

Doctoral dissertation prepared under the supervision of dr hab. Artur Kalinowski

February 2021

Abstract

This thesis presents the first measurement of the total cross-section of the coherent ultra-peripheral photoproduction of the Υ meson in lead-lead collisions at $\sqrt{s_{NN}} = 5.02$ TeV. The data used in the analysis has been collected in 2018 by the CMS experiment at the CERN's Lage Hadron Collider. The considered channel is the muon decay of the Υ meson, $\Upsilon \to \mu^+\mu^-$. The obtained value of the total cross-section is $\sigma_{\mathrm{PbPb}\to\Upsilon(1S),\mathrm{coh}} = 38.4 \pm 6.2\ (\mathrm{stat}) \pm 3.6\ (\mathrm{syst})\ \mu\mathrm{b}$. This process is sensitive to the nuclear Parton Distribution Functions for gluons.

To my Parents

Contents

1 Theoretical Introduction

1.1 Introduction

The mass of the visible Universe is composed almost entirely of hadrons, which in turn are built up by quarks and gluons. It occurs that the mass of bare quarks (current mass) that can be explained by the Higgs mechanism is less then 1% of the final mass of hadrons which they form. The remaining 99%, is composed by the strong interactions between quarks mediated by gluons [1] and described by the Quantum Chromodynamics. Thus investigation of interactions of partons inside the hadrons is fundamental to our understanding of the Universe.

About 20 μs after the Big Bang the Universe is thought to have existed in a state of deconfined hadronic matter known as the Quark-Gluon Plasma (QGP). In this state quarks and gluons are free to move relatively independently – this feature of QCD is called asymptotic freedom. It is possible that this state of matter is reproduced in relativistic heavy-ion collisions at the Large Hadron Collider (LHC) in CERN. In order to be certain of the existence of QGP in heavy-ion collisions, it is first necessary to understand the initial state of the nuclei in the absence of QGP. In QCD the partonic structure of a nucleon can be described via the Parton Distribution Functions.

The distributions of gluons inside hadrons can be probed by measuring the cross-section of ultra-peripheral vector meson photoproduction, where a photon produced by the charged particle passing close to the hadron interacts with a pomeron from that hadron. The probability of this interaction is thus sensitive the gluon distributions for hadrons. This thesis presents first measurement of the process where an Υ meson is produced during ultra-peripheral lead-lead collisions, which probes new range of momentum fraction and hard scale; and thus further extends the current description of the effect of the nuclear shadowing. The result is compared to the available theoretical models.

1.2 Quantum Chromodynamics

Fundamental particles and their interactions are described by the Standard Model[1], a theory, that has been developed by many scientists and finally formulated in mid-1970s, when the existence of quarks has been experimentally comfirmed. It is built on top of two fundamental quantum field theories: Elektroweak providing a unified approach to the weak and electromagnetic interactions and Quantum Chromodynamics (QCD) describing the strong and nuclear interactions. Together with the General Relativity, which still does has not been successfully described by any quantum theory, Elektroweak and QCD are the most fundamental theories in modern physics. They encompass the description of four fundamental interactions - electromagnetic, week and strong describing elementary particles and their dynamics and the gravity. Table 1 shows the main properties of the four fundamental interactions.

Table 1: Table shows the four fundamental forces and their carrier bosons. The relative strengths are approximate values of force between the fermions subject to given fundamental interaction at a distance of 1 fm – about the radius of a nucleon. Graviton has not yet been discovered.

Interaction	Mediators	Spin	Relative strength
Strong	gluons, g	1	1
Electromagnetic	photons, γ	1	10^{-3}
Weak	W and Z bosons	1	10^{-8}
Gravitation	gravitons (hypothetical)	2	10^{-37}

All known matter consists of two kinds of fundamental particles: quarks and leptons. Quarks come in 6 flavors: (u), down (d), charm (c), strange (s), top (t) and bottom (b), and each has its antiquark. They carry fractional charge of the electron, e: -1/3 e or +2/3 e. They fall into three generations (see Tab. 2). Additionally each of them comes in three colors, so there are 36 quarks in total. The quarks which determine the quantum numbers of hadrons are called constituent or valence quarks. Hadrons also consist of virtual quark-antiquark pairs generated by gluons and gluons themselves what is referred to as quark-gluon sea. Quarks are fermions with 1/2 spin and gluons are bosons with spin = 1. The six leptons are also divided into three generations: according to their electron, muon and tau lepton quantum numbers. There also are six corresponding antileptons with opposite quantum numbers and charges (Q). The interactions have their carrier particles, photon for electromagnetism, W^+, W^- and Z^0 for weak force and eight gluons for the strong force. Standard Model also includes the Higgs boson responsible for the mass of fundamental particles.

Table 2: Table presents fundamental fermions building up all the known matter. They are divided into quarks and leptons. [2].

	Leptons				Quarks			
	Particle		Q	mass/GeV	Particle		Q	mass/GeV
First generation	electron	(e^-)	−1	0.0005	down	(d)	−1/3	0.003
	neutrino	(ν_e)	0	$< 10^{-9}$	up	(u)	+2/3	0.005
Second generation	muon	(μ^-)	−1	0.106	strange	(s)	−1/3	0.1
	neutrino	(ν_μ)	0	$< 10^{-9}$	charm	(c)	+2/3	1.3
Third generation	tau	(τ^-)	−1	1.78	bottom	(b)	−1/3	4.5
	neutrino	(ν_τ)	0	$< 10^{-9}$	top	(t)	+2/3	174

The existence of quarks was first proposed by Gell-Mann and Zweig in 1964 [3] [4]. The idea of quarks occured as a consequence of symmetries observed in hadrons. Hadrons are composite particles consisting of quarks. Mesons are hadrons composed of a quark-antiquark pair, baryons are composed of three quarks, tetraquarks are composed of four quarks and pentaquarks of five. The dependencies between know hadrons were explained in an elegant way by the introduction of u, d and s quarks as their components. The hadrons were grouped into $SU(3)_{uds}$ multiplets. A multiplet is a set of particles having similar properties, e.g. the spin multiplet consists of particles having the same value of spin. Figure 1 shows the decuplet of observed baryons with spin 3/2 and positive parity (+). Panel a) shows the the quark composition of those baryons. In parenthesis are the masses in MeV. They are similar with differences of few a MeV for the particles belonging to the izospin multiplet. The masses of particles with different strangeness differ largely and the differences are approximately proportional to the differences in strangeness. On the basis of observation of this regularity the existence of the Ω^- baryon was predicted three years before its observation in 1964 [6].

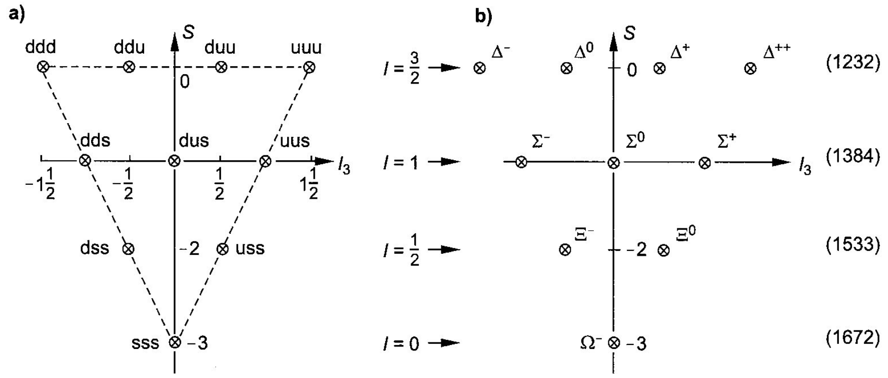

Figure 1: Quark composition of the particles of baryon decuplet. S is the strangeness I is the izospin ans I_3 is the third component of the izospin. In parenthesis is the mass in MeV. [7]

After the Quark Model has been accepted the physicists started the search for free quarks, but it soon became clear that they do not occur as free particles. Around that time Richard Feynman postulated the existence of partons to explain the process of Deep Inelastic Scattering (DIS) of leptons on nucleons [8]. They were assumed to be quasi-free and point-like particles that build up nucleons. It soon occurred that quarks are partons, and cannot be found free because of interaction potential that is increasing with the distance between the quarks. This strong interaction is carried by massless particles called gluons. Therefore partons are quarks and gluons.

The quarks are fermions and hence they obey the Pauli exclusion principle stating that two identical fermions cannot simultaneously occupy same quantum state. Quarks seemed to break this rule (for example Ω^- baryon). To solve this problem the new quantum number, color, was introduced. One of the evidences of the existence of color quantum number is the measurement of the ratio of the cross-sections of the processes:

$$\frac{\sigma\left(e^+e^- \to \text{hadrons}\right)}{\sigma\left(e^+e^- \to \text{leptons}\right)}. \tag{1}$$

The cross-section σ is a measure of probability for a given process to occur during a two-particle collision. It is expressed in terms of the the area that the particle must hit in order for the given interaction to take place. The units of σ are thus m^2 or barns b, where b= 10^{-28} m^2 = 100

fm^2. The measured value of the ratio in Eq. 1 is three times greater than expected without introducing color [5]. This indicated that the quarks have additional quantum number with three degrees of freedom, $N_c = 3$. This new quantum number gave name to the theory of strong interactions: Quantum Chromodynamics.

QCD describes strong interaction between particles caring color degree of freedom. The accepted convention is that the three color quantum numbers that quark can possess is red, blue or green. The antiquarks possess anti-colors. Only "white" particles can be formed, e.g. blue and antiblue quark and antiquark building up a meson or red, green blue quarks and antiquarks building up a hadron and so on. These are called color singlet states.

The two important features of QCD are the color confinement and the asymptotic freedom.

The confinement is the phenomenon that color charged particles cannot be isolated, as the force between quarks grows as they are separated. Therefore quarks and gluons have never been observed free, only SU(3) color singlet states i.e. with zero color quantum number can exist. The interaction potential between quarks in the non-relativistic QCD approximation is given by:

$$V_s = -\frac{4}{3}\frac{\alpha_s}{r} + kr, \tag{2}$$

where α_s is the strong coupling constant, r is the distance between quarks and value of the constant k is ~ 0.85 GeV·fm^{-1}. The first part of the formula is similar to the one for electromagnetic interactions. The second one explains why the quarks are never observed free. This is shown in Figure 2. It illustrates the process where a new pair of quarks is created after enough energy is provided to the system while separating the quarks from the first pair (panel a) and b)). The panel (c) shows the decay of the ρ^+ meson to two pions π^+ and π^0. The colour confinement can be qualitatively understood by considering pulling appart two quarks. The interaction between them is caused by the exchange of virtual gluons, which carry colour charge. Because of this they interact with themselves as shown in Figure 3, panel a). It results in squeezing of the color field into a tube, in contrast to spreading out as in case of electrodynamical interactions (Figure 3, panel b)). It results in confining the color field tightly as shown on panel c) of Figure 3. At large distances the density of energy in the tube is constant, therefore the energy of the interaction is proportional to the distance, giving the second term in equation (2). Figure 4 shows the form of the non-relativistic QCD potential between quark anti-quark pair. The values of k and α_s constants have been approximated to $k = 1$ GeV/fm and $\alpha_s = 0.2$. The potential is negative below about 0.25 fm. At larger radii the linear term is dominating setting the confinement scale.

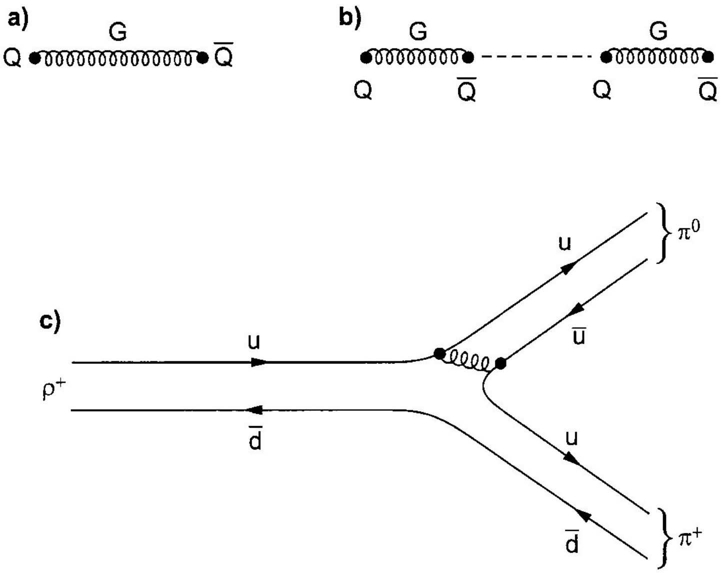

Figure 2: Stretching the "gluon string" that connects quarks requires force proportional to the constant k and distance between the quarks. When there is enough additional energy stored in the gluon field a new pair of quark and antiquark is created (b). Panel (c) illustrates the decay of the ρ^+ meson to two pions π^+ and π^0. [7]

The asymptotic freedom states, that the partons (quarks and gluons) at small distances (corresponding to high energies) interact very weakly and can be considered as free particles. The reason for this is the running of α_s – it varies considerably with the energy scale of the interaction. At high interaction energies above 100 GeV the α_s is of the order of 0.1 and is sufficiently small for the partons to be quasi-free particles instead of being strongly bound within the hadron. On the other hand, for low-energy scales,

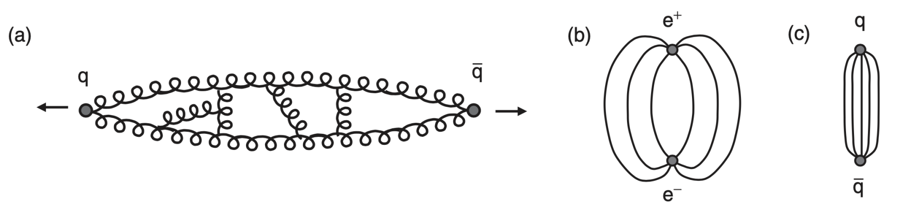

Figure 3: Qualitative explanation of the effect of the long-range color interaction between quarks (panels a) and c)) compared to electro-dynamical interactions (panel b)). [2]

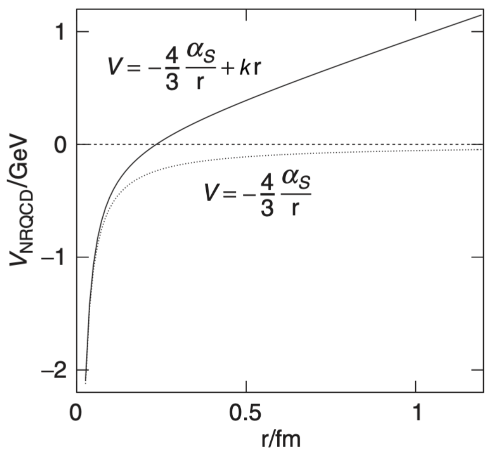

Figure 4: The non-relativistic QCD potential between quark anti-quark pair for $k = 1$ GeV/fm and $\alpha_s = 0.2$. [2]

at ~ 1 GeV the α_s is large, of the order of 1. Therefore higher-order contributions to given process do not converge rapidly and have to be included in the calculations. Because of that QCD is non-perturbative at low-energy regime, unlike QED, where higher order Feynman diagrams can be treated as a correction i.e. perturbation to leading-order diagrams.

1.3 Parton Distribution Functions

1.3.1 Deep Inelastic Scattering

In order to see the structure of a composite object a probing particle of wavelength λ small compared to the size of this object R is needed – $\lambda \ll R$ (see Figure 5). This can be achieved in process called Deep Inelastic Scattering (DIS). For instance in case of the scattering of high energy electrons on nucleons the electron and parton can exchange a photon or Z boson (Figure 6, panel (a)) or W boson (panel (b)).

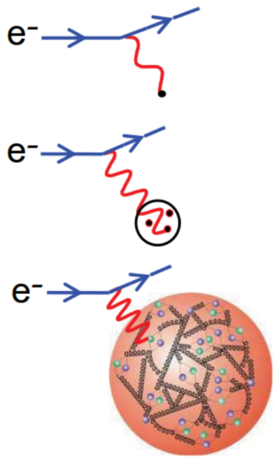

Figure 5: Figure shows the dependence of electron-proton scattering process on the photon wavelength λ. In first case $\lambda \gg R$ and the photon interacts with the point-like proton. When λ is smaller than the size of a proton, the photon is scattered from the quarks. For very high energies of an electron, when $\lambda \ll R$, the proton appears to be a quark-gluon sea. [10]

The wavelength of the photon is proportional to the inverse of the four-momentum transfer Q to the hadron ($\lambda \sim 1/Q$). In case of electron-nucleon DIS $Q^2 \gg M^2$ is needed, where M is the mass of the nucleon, and $W^2 \gg M^2$, where W is the invariant mass of the outgoing system.

Depending on the variables measured in the experiment the scattering is divided into three kinds. In case of restricting to two variables; the energy of scattered lepton and its detection angle the process is called inclusive. When the information on the whole final system is obtained the process is called exclusive, and semi-inclusive (SIDIS) when it is partially reconstructed.

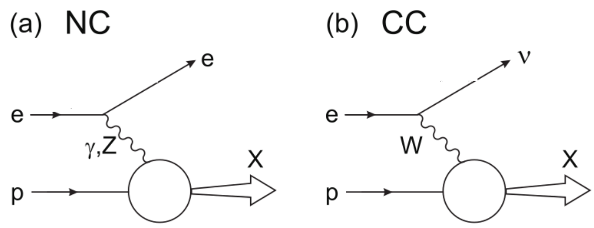

Figure 6: Neutral- and charged-current DIS mediated by γ or Z and W. Panel (a) shows the DIS ,ep $\rightarrow$ eX process. The neutral current (NC) DIS is mediated by γ and Z exchange. Panel (b) shows charged-current (CC) DIS mediated by W boson (ep $\rightarrow$ ν X). [9]

If one considers a frame in which the target nucleon has a very large momentum, the target can be seen as a stream of free partons (because of asymptotic freedom), each carrying a fraction x (also called Bjorken-x) of the nucleon's longitudinal momentum (see figure 7).

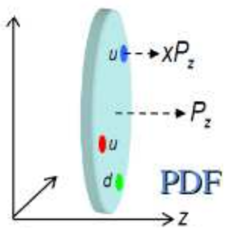

Figure 7: Diagram showing a proton moving in z direction with momentum P_z and a quark within it with momentum $x \cdot P_z$. [10]

1.3.2 Parton Distribution Functions

Parton Distribution Functions (PDFs) are the distributions of longitudinal momenta of the partons within the proton. By increasing Q^2 we start to observe three valence quarks and more and more quark-antiquark pairs (sea quarks) which originate from gluons via g $\rightarrow$ q$\bar{\text{q}}$ and gluons themselves. All those partons carry fraction of the longitudinal nucleon's momentum, what is described by the PDFs. Therefore PDFs also depend on square of the four-momentum transfer to the hadron Q^2.

The observable in DIS is the cross-section. It is conventionally written in terms of scalar structure functions $F_i(x, Q^2)$ ($i = 1, 2, 3$) which are a measure related to hadron's partonic structure. Because of asymptotic freedom the quarks inside the nucleon can be treated as free particles for high energies (as explained above). The electron-proton double differential cross-section is given by:

$$\frac{\mathrm{d}^2\sigma(\mathrm{ep})}{\mathrm{d}x\mathrm{d}Q^2} = \frac{4\pi\alpha^2}{Q^4}\frac{F_2^{\mathrm{ep}}(x)}{x}\left[\frac{1+(1-y)^2}{2}\right], \tag{3}$$

where y is the the inelasticity of the scattered lepton. Because of a simplifying feature called Bjorken scaling $F_2(x, Q^2) \to F_2(x)$. Due to this feature some properties of hadrons probed in high-energy scattering experiments are not determined by the energy of an experiment, but instead by dimensionless kinematic quantities e.g. the ratio of the energy to a momentum transfer. For more details on Bjorken scaling see chapter 1 of [9].

Let $u(x)\mathrm{d}x$ be the number of u quarks in a proton caring the fraction of the momentum of the proton within $(x, x + dx)$ and accordingly for other quarks. The structure function $F_2^{ep}(x)$ is given by quark distributions with squares of charge as weights

$$\frac{F_2^{ep}(x)}{x} = \frac{4}{9}\left[u(x) + \bar{u}(x)\right] + \frac{1}{9}\left[d(x) + \bar{d}(x) + s(x) + \bar{s}(x)\right]. \tag{4}$$

Note the contribution of strange quarks, which come from the quark-gluon sea mentioned earlier. For a general overview of structure functions see chapter 2 of [9].

The idea for obtaining PDFs is to parametrize its x dependence at some low, yet perturbative, scale Q_0^2. It is not possible to directly calculate the proton PDFs from the QCD, but the Q^2 dependence of the PDFs can be obtained with parton evolution functions called DGLAP (Dokshitzer Gribov Lipatov Altarelli Parisi, see chapter 6 of [9]). They are based on parton splitting functions for the QCD processes and describe the relation between parton densities and the energy scale. After using the DGLAP evolution equations to evolve PDFs up in Q^2 the remaining parameters included in the given model are obtained by fitting to data. These equations can be formulated at different levels of approximation relative to different power of QCD coupling constant $\alpha_s(Q^2)$:

- Leading-Order (LO): first order in $\alpha_s(Q^2)$,
- Next-to-Leading-Order (NLO): second order in $\alpha_s(Q^2)$,
- Next-to-Next Leading-Order (NNLO): third order in $\alpha_s(Q^2)$.

With higher order approximation the calculations get much more complex. The example Feynman diagrams representing different approximations are shown in Figure 8.

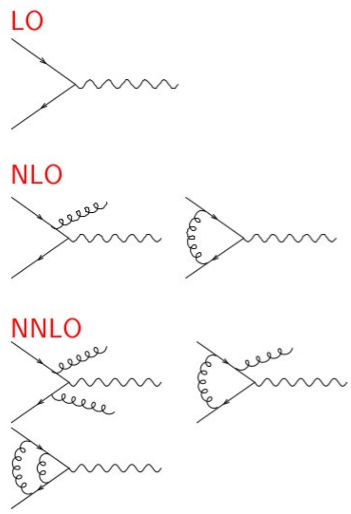

Figure 8: Feynman diagrams representing different approximations. The diagram at LO represents interaction of quark (straight line) with a photon (wave). At NLO emission and absorption of gluon (curly line) by quark is taken into account. At NNLO and higher orders problem starts to be more and more complex.

1.3.3 Nuclear Parton Distribution Functions

PDFs for nuclei (nPDFs) are not determined as precisely as the nucleonic PDFs. They are usually defined for each parton in terms of nuclear modifications $R_i^A(x, Q^2)$ to the corresponding free proton PDF $f_i^p(x, Q^2)$:

$$f_i^A(x, Q^2) = R_i^A(x, Q^2) f_i^p(x, Q^2). \tag{5}$$

The nuclear modifications of the structure function F_2 are typically 10-20% [9]. Accurate determination of the nPDFs is important for better understanding of non-perturbative QCD.

There are a few groups which have been investigating the nPDFs by analyses of world data on high-energy nuclear reactions. Table 3 summarizes three contemporary global analyses: EPPS16[12], NCTEQ15[13] and DSSZ12[14]. EPPS16 is the most comprehensive datawise, as it includes e.g. proton-lead data on electroweak bosons and dijets form the LHC.

Table 3: Specifications of contemporary nPDF analyses.

	NCTEQ15	EPPS16	DSSZ12
DIS in ℓ^-+A	✓	✓	✓
Drell-Yan in p+A	✓	✓	✓
RHIC pions d+Au	✓	✓	✓
ν-nucleus DIS		✓	✓
Drell-Yan in π+A		✓	
LHC p+Pb dijets		✓	
LHC p+Pb W, Z		✓	
Order in α_s	NLO	NLO	NLO
Q cut in DIS	2 GeV	1.3 GeV	1 GeV
datapoints	708	1811	1579
free parameters	16	20	25

Figure 9 shows results as the PDF nuclear modifications defined as ratios between the bound and free proton PDFs ($R_i^A(x,Q^2)$ from equation 5) from EPPS16, nCTEQ15 and DSSZ12. In case of the valence quarks (u_V and d_V) the nCTE15 and EPPS16 are consistent within uncertainty bands – in those groups valence quarks were independently parametrised. The uncertainties are artificially smaller for DSSZ12 group because of lack of the flavour freedom in their parametrisation. In case of the sea quarks (u,d,s) EPPS16 uncertainties are larger because only this group had sea-quark flavours parametrised independently. On the other hand this results in less biased for EPPS16 compared to the nCTEQ15 and DSSZ12. Because of the dijet data used in the EPPS16 analysis the uncertainty bands are narrower at large x compared to the nCTEQ15. In case of the DSSZ12 results there is almost no nuclear effects for gluons. Figure 10 shows EPPS16 results for gluons for two different energy scales Q^2.

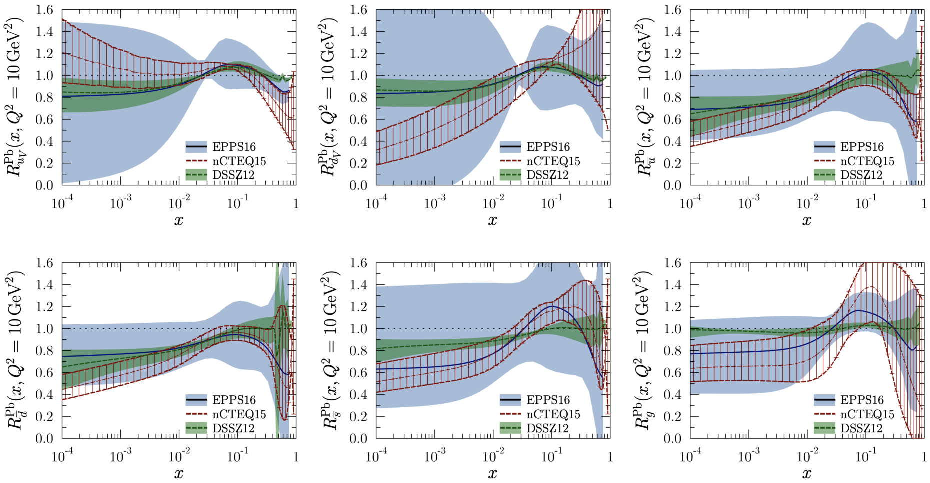

Figure 9: Nuclear modifications for lead from the NLO fits at Q^2=10 GeV obtained by three groups: EPPS16n shown in blue, CTEQ15 in red and DSSZ12 in green. The results are presented for u, d, ū, d̄, s̄ quarks and for gluons. The uncertainties are shown as bands. [11]

Parton Distribution Functions are widely used in experimental particle physics. They are crucial for calculation of the cross-section which is the fundamental input in analysis in collider physics e.g. nowadays at the LHC. The differences in nPDFs obtained by various groups are sometimes vast due to different approaches to parametrization and datasets used. Nevertheless there are many groups and they are constantly working on improving their calculations. New data is provided by many experiments, as discussed above. The PDFs and nPDFs are exceptionally important in era of a hadron colliders as Large Hadron Collider, where they are indispensable for investigation of internal structure of hadrons. The precise information about the initial stage of the collision is also important for finding new phenomena in hadron and nuclear physics and physics beyond the standard model as it allows to better interpret obtained results. In addition a proper description of processes in high-energy collisions involving nuclei in natural circumstances such as interactions of cosmic rays with the atmosphere benefits from the proper knowledge of the nPDFs.

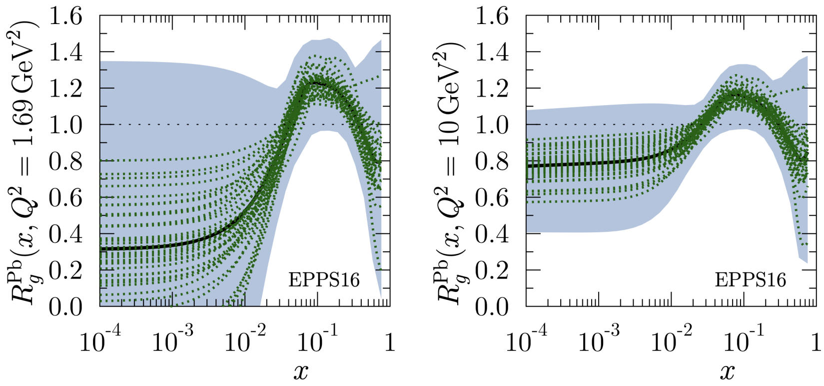

Figure 10: The EPPS16 nuclear modifications for lead. Largest uncertainty for gluon distributions is for $x < 10^{-2}$ and low Q^2. This is because of lack of data in this region. Green dotted lines represent all components to the total uncertainty, which is shown as the blue region. [12]

1.3.4 Gluon Shadowing

As shown above, the nuclei cannot be understood as a simple superposition of their constituent nucleons. There is something more that modifies its nature. In particular QCD predicts that at and below $x \sim 10^{-2}$ the nuclear modification factor for gluons will be less than 1. The behaviour of the modification factor in this region is called the gluon shadowing effect. It can be seen in Fig. 10 where the change in form factor plotted as a function of Bjorken-x for different Q^2 is shown. Large uncertainty bands in this region are a result of lack of sufficient experimental data. Previous analysis done by ALICE (A Large Ion Collider Experiment) collaboration at LHC used the ultra-peripheral coherent J/ψ photoproduction (see subsection 1.4) to constrain models of shadowing [15]. The analysis performed by ALICE provided direct evidence of nuclear shadowing during heavy-ion collisions [16]. The data is consistent with models that include nuclear shadowing modification to the gluon distribution of the nuclei (see Fig. 11).

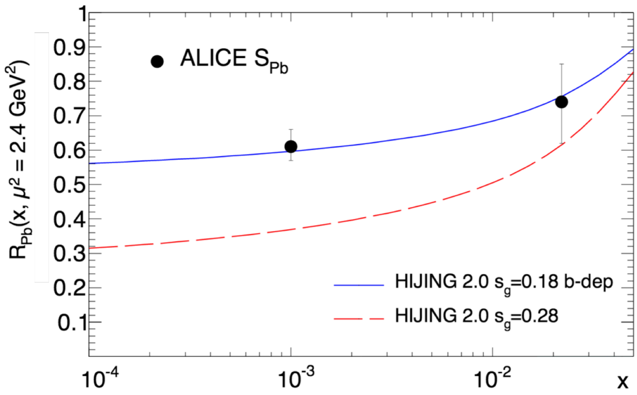

Figure 11: Comparison of the ALICE suppression factors with predictions of the nuclear gluon shadowing in HI-JING 2.0 with impact parameter dependence (b-dep) and without this dependence. The nuclear gluon shadowing is characterized by the parameter s_g; data is consistent with $s_g = 0.18$. [16]

1.4 Photoproduction

Photoproduction occurs when one or more particles are produced upon an action of an incident photon. In case of nucleus-nucleus collision the photon produced by one hadron can interact with partons of the second hadron or with a photon. To calculate the photon flux the Weizsäcker-Williams approximation can be used [17] [18]. It relates the electric field of charged particle at rest to the photon field created at ultra-relativistic velocities. This is semi-classical approach – quantum mechanical equation for the energy of the photon is combined with the Fourier transform of Maxwell's equations. For the detailed derivation of the photon flux on the target nucleus, N see Appendix A).

Photoproduction can take place in few production modes which depends on the momentum of the photon. When the photon's wavelength is large compared to the hadron's size, it interacts coherently with the whole nucleus, which stays intact after the interaction. For higher momentum photons, i.e. shorter wavelength, interaction is incoherent, which means that the photon interacts with a single nucleon rather than whole nucleus. This interaction is responsible for the nucleu's break-up.

1.5 Ultra-peripheral Collisions

The LHC apart from QCD driven interactions is a very powerful source photoproduced interactions such as γ-γ and γ-hadron (see Fig. 12). A photon generated by one of the passing hadrons can interact with another photon or with a partons inside a second hadron producing a variety of final state particles (e.g. vector mesons (VM) such as J/ψ or Υ). In particular the ultra-peripheral collisions (UPC) are events, where two hadrons do not collide head on, but they pass close to one another (see Fig. 13). UPCs in proton-proton (pp), proton-nucleus (pA) and nucleus-nucleus (AA) interactions constitute a interesting path of measurements in the LHC. For example exclusive VM photoproduction can be related to the square of the gluon density at zero-momentum transfer (see Fig. 12, panel a)) and therefore are sensitive to the nPDFs [19]. These events offer a unique opportunity to study fundamental aspects of QED and QCD via photon-induced processes, what leads to better description of how hadrons are built.

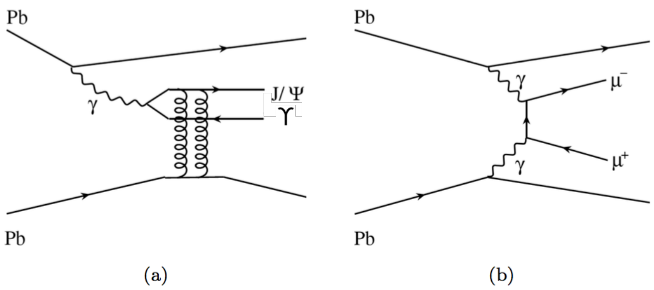

Figure 12: The Feynman diagrams of an ultra-peripheral collision for Pb+Pb. Diagram a) shows photoproduction process of mesons, b) is a $\gamma\gamma$ interaction producing two muons. VM photoproduction can be related to the square of the gluon density.

In experimental particle physics an observable called rapidity y is often used. For a particle of non-zero rest mass m the energy $E = \gamma mc^2$ and scalar momentum $|\vec{p}| = \gamma mv$, where γ is a Lorentz factor and v is the velocity. Then the rapidity is defined as:

$$y = \frac{1}{2} \ln \frac{E + p_z c}{E - p_z c}, \tag{6}$$

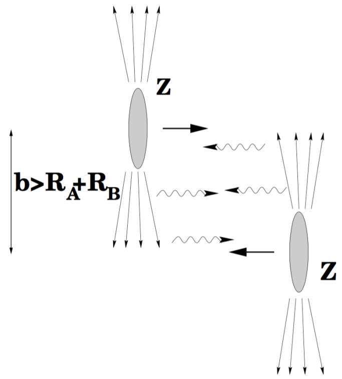

Figure 13: A representation of an ultra-peripheral collision. The pancake–like shape of the nuclei is due to relativistic Lorentz contraction.

where p_z is the the momentum component along the the beam axis. The differential cross-section with respect to y for the UPC VM photoproduction in PbPb collisions is given by:

$$\frac{d\sigma_{\mathrm{PbPb}}(y)}{dy} = N_{\gamma\mathrm{Pb}}(y, M)\sigma_{\gamma\mathrm{Pb}}(y) + N_{\gamma\mathrm{Pb}}(-y, M)\sigma_{\gamma\mathrm{Pb}}(-y) \tag{7}$$

where $\sigma_{\gamma\mathrm{Pb}}(y)$ is the photoproduction cross-section, M is the mass of produced VM and $N_{\gamma\mathrm{Pb}}$ photon flux on the target Pb nucleus. Rapidity y of a photon is given as

$$y = \ln\left(\frac{2k}{M}\right), \tag{8}$$

where k is the energy of a photon. There are two terms in equation 7 because both colliding lead nuclei may produce the photon. Figure 14 shows the photon flux produced by a lead nucleus as a function of rapidity y. Results are presented for two different LHC beam energies and for photon energies corresponding to the production of a J/ψ and a Υ vector mesons.

In heavy-ion physics analyses it is always necessary to distinguish between final state particles produced directly by the nuclei themselves from those originating from the QGP. Therefore there is a great need to study the nature of the initial state forming during collisions. Lack of understanding of these states leads to uncertainties of the measured properties of QGP, e.g. viscosity.

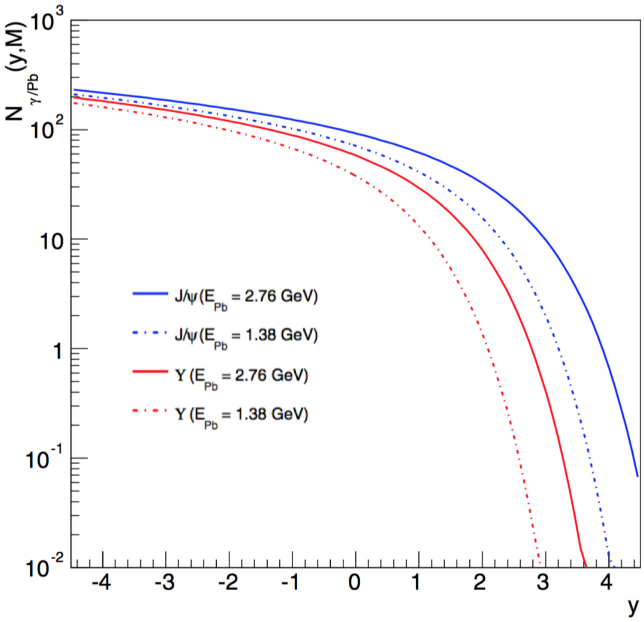

Figure 14: Photon flux produced by a Pb nucleus as a function of rapidity y. Results are shown for two LHC beam energies and for photon energies corresponding to the production of a J/ψ and a Υ mesons. [20].

1.6 Ultra-peripheral Υ photoproduction in PbPb

As discussed above, most recent nPDFs show, that gluon distributions are still poorly known. This is especially true at small Bjorken-$x < 10^{-2}$ (see Fig. 10). A photo-nuclear interaction that has attracted a lot of interest is exclusive VM photoproduction. In this reaction only a vector meson is produced in the final state (see Fig. 15). Figure 16 presents event displays of the typical heavy collision in the CMS detector (panel (a)) and a UPC Υ photoproduction candidate (panel (b)).

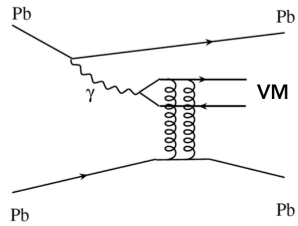

Figure 15: The Feynman diagram presents the exclusive vector meson (VM) photoproduction.

Photoproduction in ultra-peripheral heavy-ion collisions is a powerful probe of nuclear structure. The PDF phase space, accessible by different experiments and measurements, can be seen in Fig. 17. The studies of UPCs allow to set constrains on the theoretical models in a little known kinematic region of $x < 10^{-2}$.

For example, a meson produced at rapidity y is sensitive to the gluon distribution at Bjorken-x, and hard scales Q^2:

$$x = \frac{M_{\mathrm{meson}}}{\sqrt{s}} e^{\pm y}, \tag{9}$$

$$Q^2 \sim \frac{M^2_{\mathrm{meson}}}{4}, \tag{10}$$

where M_{meson} is the meson's mass and $\sqrt{s}$ is the center-of-mass energy. The J/ψ particle mass is equal to 3.01 GeV. Analysis presented in this work allow to access poorly known, low-x region of parton distributions by focusing on the UPC Υ meson photoproduction in PbPb collisions. The mass of Υ meson is M_{Υ}=9.46 GeV. The cross-section for the UPC Υ photoproduced

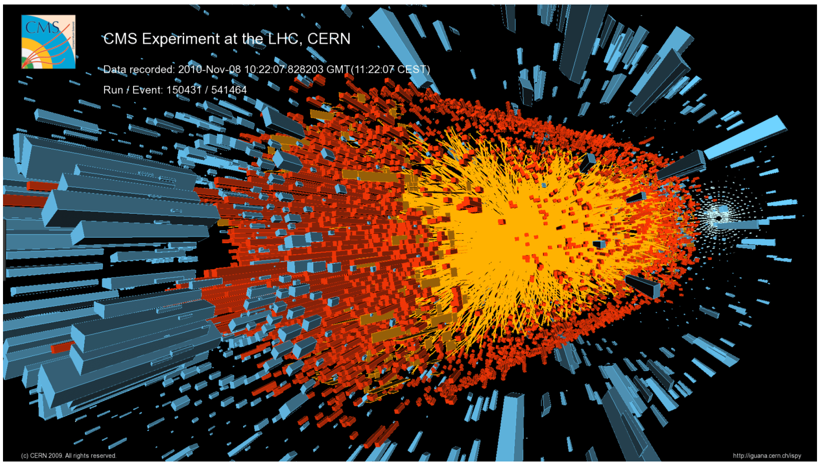

(a)

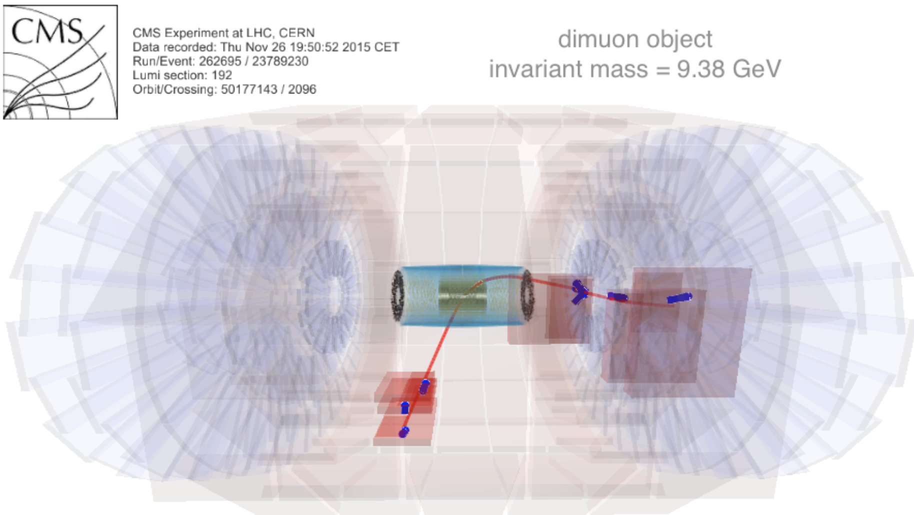

(b)

Figure 16: Visualisation of the heavy-ion collisions in CMS from the real data. Panel (a) shows a typical, head-on heavy ion event with thousands of produced tracks, while panel (b) presents an event collected during PbPb collisions where there are only two muons reconstructed in otherwise empty detector. The calculated mass of the muon pair is 9.38 GeV.

mesons is sensitive to a new range of momentum fraction and hard scale; thus this measurement will further extend the current description of nuclear

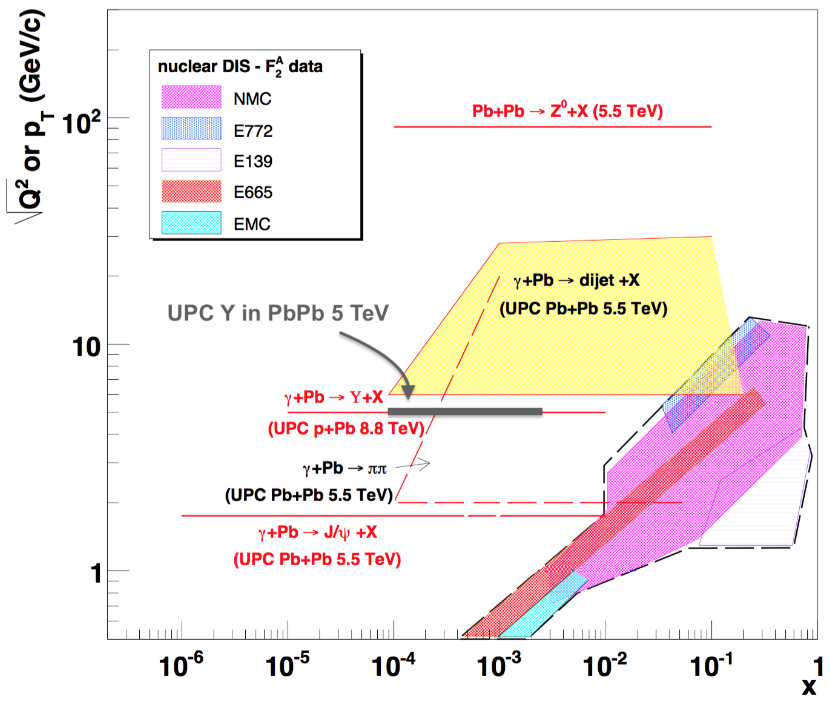

Figure 17: The kinematic range in which various ultra-peripheral processes can probe gluons distributions in protons and nuclei in dijet, quarkonium and dihadron production. The values of Q^2 for typical gluon virtuality in exclusive UPC quarkonium photoproduction is shown for two mesons – J/ψ and Υ. In grey color the approximate range covered by the UPC Υ photoproduction in PbPb collisions is shown. The kinematic ranges available for Z^0 hadron production at the LHC are also shown for comparison. Measurements were performed by the European Muon Collaboration (EMC), E139 (Stanford Linear Accelerator Center), E772 and E665 at Fermilab and the New Muon Collaboration (NMC). [19]

shadowing. The Υ meson is capable of probing the parton distribution at a higher value of Q^2 than that of the J/ψ meson. A more precise model of shadowing ultimately requires the exploration of this new kinematic region. Specifically, the data collected in 2018 during PbPb collisions offer an abundance of events of Υ production which can serve as a measure of the nuclear gluon density distribution. This thesis presents first measurement of ultra-peripheral Υ meson photoproduction in PbPb collisions. The data for presented analysis has been collected by the CMS experiment at the LHC.

2 CMS experiment at the LHC

2.1 The Large Hadron Collider

The Large Hadron Collider (LHC)[21] is, as of 2020, the most powerfull particle collider. The LHC was built by the European Organization for Nuclear Research (CERN) near Geneva between 1998 and 2008. It was designed to collide protons at $\sqrt{s} = 14$ TeV in the center of mass system and heavy-ions including lead-proton and lead-lead interactions at highest energies ever achieved. The LHC is build in a 27 km long tunnel, about 100 m underground (see Fig. 18). The tunnel was originally built for the Large Electron Positron (LEP)[22] collider which was working until 2000.

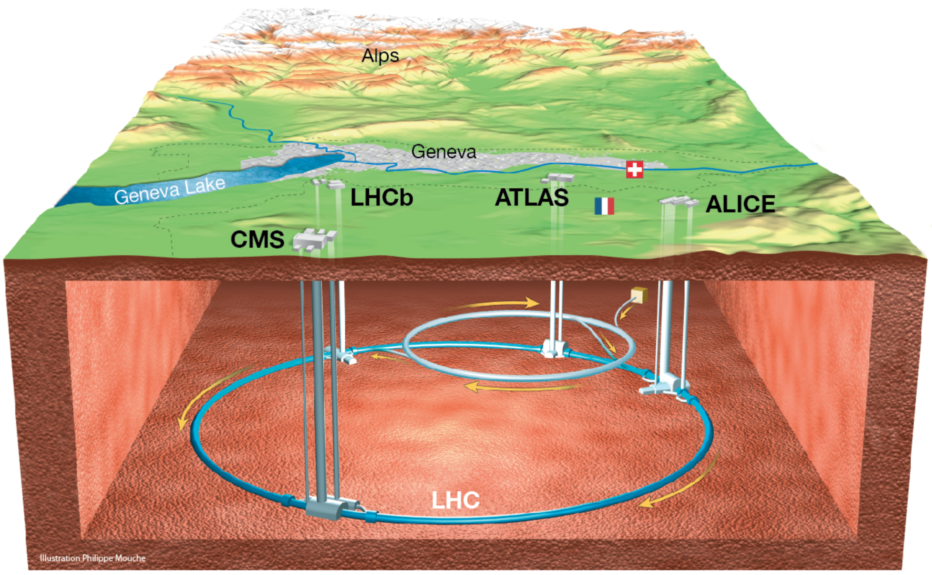

Figure 18: Location of the LHC and its experiments in the vicinity of Geneva, Switzerland. [24]

Before entering the LHC machine hadrons are accelerated increasingly in a large complex (see Fig. 19).

The source of protons is a bottle of hydrogen. The hydrogen atoms are first stripped of their electrons when passing through electric field, thus forming a proton beam. Protons are first fed to Linear accelerator 2 (Linac 2,

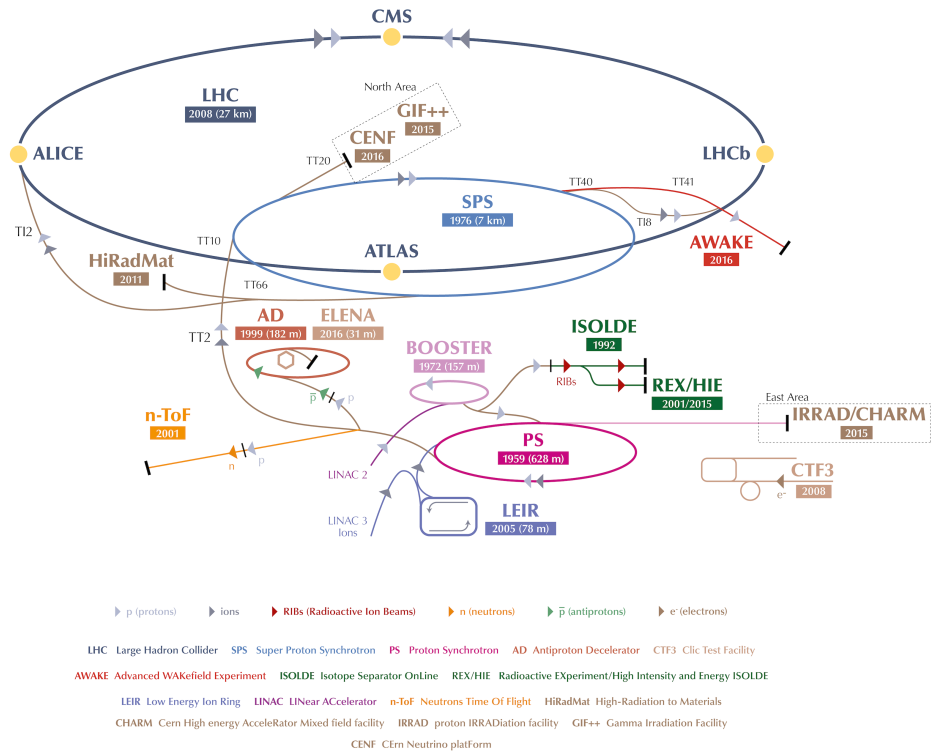

Figure 19: Accelerator and detector complex at CERN. The LHC is the dark blue ring. The particles are boosted by the chain of smaller machines. Apart from LHC and its detectors there is a whole set of smaller experiments. [25]

replaced by Linac 4 in 2020). In linear accelerators the radio-frequency (RF) cavities are used to accelerate particles by giving them electrical impulses. The shape of the conductor that forms a cavity is such that it causes the electromagnetic waves at certain frequencies to resonate forming a standing wave. When the protons pass through the standing electromagnetic wave they are accelerated. After passing through Linac 2 they gain the energy of 50 MeV. After this phase the hadrons within a beam are not spread homogeneously, they form separated bunches. Moreover the beam is tightly compressed what is ensured by the small quadrupole magnets.

After that beam is injected to the Proton Synchrotron Booster which accelerates the protons further to 1.4 GeV. Then they are are injected in sequence to Proton Synchrotron (PS) which has the circumference of 628 metres. PS has 277 conventional electromagnets, including 100 dipole magnets, which bend the beams into the ring. PS operates at up to 25 GeV. Next the beam is fed to the Super Proton Synchrotron (SPS), second-largest accelerator in CERN. It has a circumference of almost 7 km, has has 1317 room-temperature electromagnets, including 744 dipoles. The SPS accelerates protons up to 450 GeV. After the SPS the beam is separated into two and enter the LHC ring in opposite directions in separate beam pipes. The whole injection process takes about 30 minutes.

In order to keep the beams on circular and opposite trajectories inside the LHC's rings, there are 1232 main superconducting dipole magnets installed around the beam pipes (see Fig. 20). They are capable of producing magnetic field of 8.3 T. They are built of 15 mm cables made from niobium-titanium alloy which becomes superconducting at 10 K. With use of liquid nitrogen and helium they are kept at 1.9 K. The cables carry current of 11850 A. There are also 392 quadrupole magnets that focus the beams. In total, the LHC contains 9593 magnets. In order to keep the accelerated particles from interacting with gas molecules the ultra-high vacuum of 10^{-13} atmospheres is kept inside the beam pipes.

After entering the LHC rings particles are accelerated to desired energy with 16 RF cavities, 8 per ring. This phase is called ramp up and takes around 15 minutes. The electric field causes the charged particles to accelerate each time they pass through the cavity during this stage of the LHC, yielding a total gain of 2 MeV per pass.

During the next stage the beams are squeezed by the quadrupole magnets to ensure small transverse size. At this point the beams are ready to be directed one on another by the corrector magnets. The collisions typically last for several hours until the density of the beams drops below certain level and they are dumped. Then the procedure is repeated.

In case of lead the ions, they are produced from a highly purified ^{208}Pb sample heated to about 800 °C. The resulting Pb vapor is partly ionized by an electron current and the ions are fed to Linac3 and accelerated to 4.2 MeV/u (MeV per atomic mass unit). Then they are further ionised by passing them through a carbon foil. After that they are injected into the Low Energy Ion Ring (LEIR) and further accelerated to 72 MeV/u. Also at this point the beam's emittance (divergence, size and energy spread) is shrinked with use of electron cooling method [28] in order to ensure high

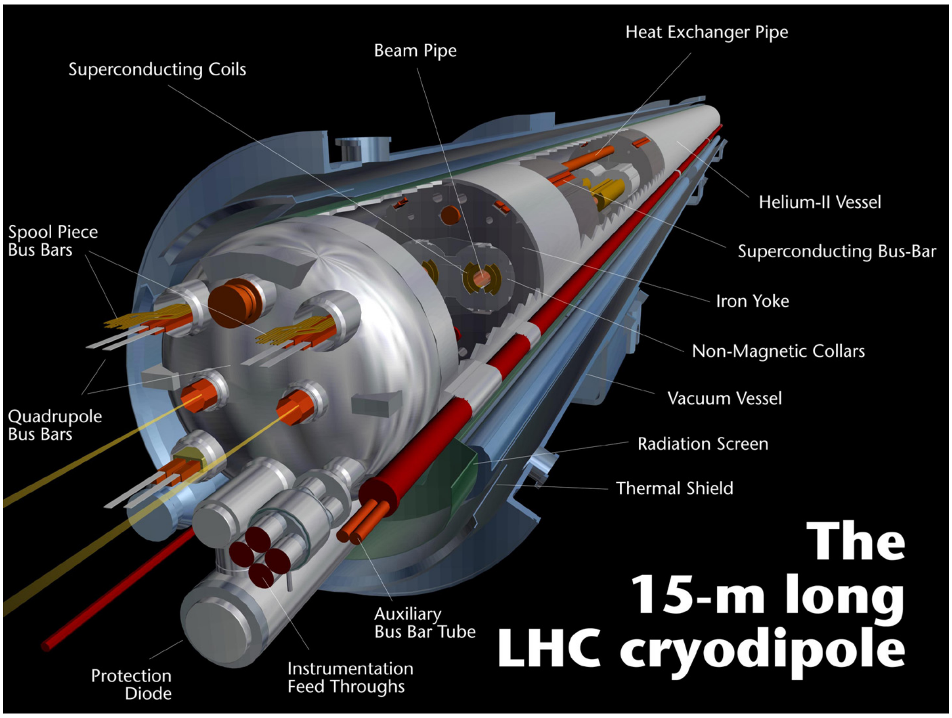

Figure 20: A cutaway diagram of an LHC dipole magnet. The superconducting coils surrounding the beam pipes are responsible for bending the beams along the 27 km ring. There are 1232 magnets of this kind in the LHC tunnel. [27]

luminosity of the LHC beam. This process takes around 10 minutes – it takes 2.5 seconds per two bunches and there are 592 ion bunches used in one LHC fill. Next the beams are stored in the PS, where they undergo further acceleration up to 5.9 GeV/u. After being completely ionised by the second foil they are sent to the SPS, which accelerates them to 177 GeV/u. At this point they are ready to be injected into both rings of the LHC. The LHC machine is also capable of running with different ions (e.g. argon, xenon and oxygen) and in proton-ion configuration.

The LHC operated during two periods called Runs – Run 1 from 2009 till 2013 and Run 2 from 2015 till 2018. The period between these runs, from 2013 till 2015 is called the Long Shutdown 1 (LS1) and was dedicated for upgrading the collider and the detectors. As of 2020 LHC is in the LS2 stage, which is planned to last until 2021. The LHC has ben designed to be capable of achieving collision energies of 14 TeV in center mass system for protons and 5.52 TeV per nucleon pair for lead-lead collisions. During Run 1 LHC has been colliding protons with energy of 7 and 8 TeV in center-mass system. During heavy-ion (HI) PbPb runs it achieved 2.76 TeV per nucleon pair and 5.02 per nucleon pair for pPb collisions. During Run 2 the colisilon energies were were increased to 13 TeV for pp, 5.02 TeV for PbPb and 8.16 for pPb collisions. The nominal bunch spacing for protons is 7.5 m, what results in 25 ns between collisions. The LHC setup is also characterised by instantaneous luminosity,

$$L_{inst} = \frac{1}{\sigma}\frac{dN}{dt}, \tag{11}$$

where N is the number of produced events with the interaction cross-section σ in a certain time t, and is proportional to the densities of the beams. L_{inst} is expressed in units of [$\mathrm{cm}^{-2}\mathrm{s}^{-1}$] or with use of barns, where b=cm^{-28}. By integrating the L_{inst} over some period of time one gets the integrated luminosity,

$$L_{int} = \int L_{inst} dt. \tag{12}$$

Fig. 21 presents the integrated luminosity delivered by the LHC to the CMS for pp and heavy-ion collisions. Fig. 22 presents the integrated luminosity as a function of time during 2018 PbPb collisions. The product of the cross-section for given process and L_{int} gives the expected number of events during given period of data-taking. Another parameter specific for the machine setup is the pile-up P_u, which is equal to the number of independent hadron-hadron interactions in a bunch crossing reduced by 1.

There are four points along the LHC ring where the circulating beams are intersecting and the collisions take place (see Fig. 19). At these interaction points four main experiments are located to collect the data:

- Compact Muon Solenoid (CMS)[30],
- A Large Toroidal LHC Aparatus (ATLAS)[31],
- A Large Ion Collider Experiment (ALICE)[32],

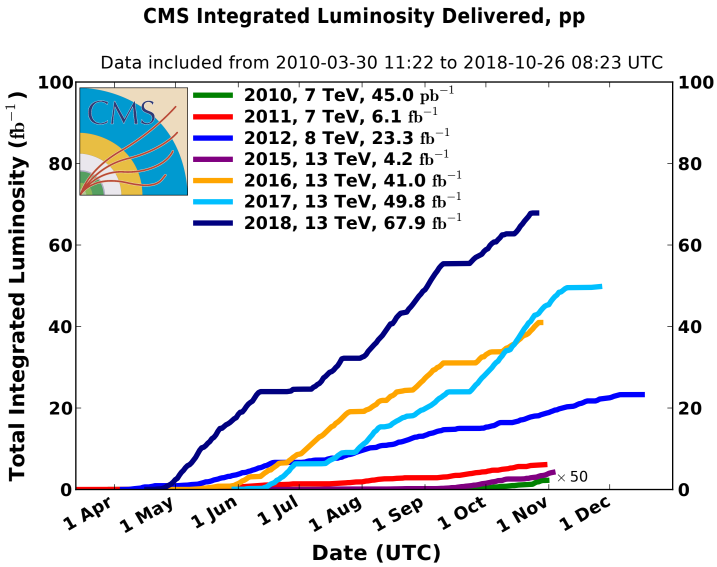

(a)

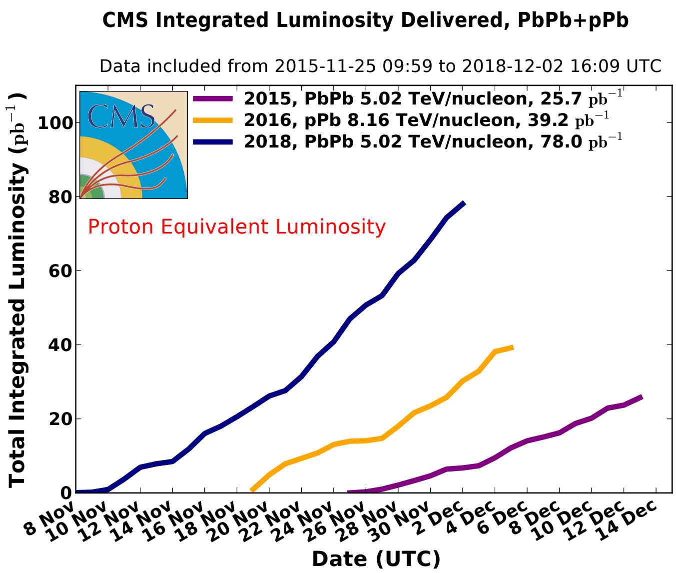

(b)

Figure 21: Integrated luminosity delivered by the LHC to the CMS for each year of data taking during pp collisions (panel (a)) and proton-equivalent luminosity delivered by the LHC to the CMS versus for each year of data taking during Run 2 HI collisions (panel (b)). In order to obtain a proton-equivalent luminosity the values for the PbPb data are scaled by a factor of $A^2 = 208^2$ and for the pPb data by a factor of $A = 208$. [29]

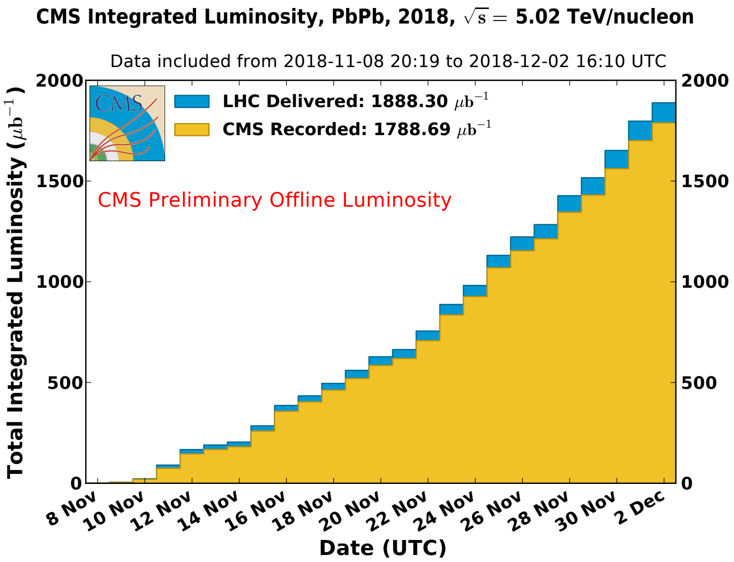

Figure 22: Integrated luminosity as a function of time during 2018 PbPb collisions. Blue region presents the luminosity delivered by the LHC and the yellow region the luminosity recorded by the CMS experiment. [29]

- LHC-beauty (LHCb)[33],

together with three smaller ones:

- Total Cross Section, Elastic Scattering and Diffraction Dissociation (TOTEM)[34],
- LHC-forward (LHCf)[35] and
- Monopole and Exotics Detector At the LHC (MoEDAL)[36].

The main purpose for designing and building the LHC was to understand the nature of electroweak symmetry breaking, the Higgs mechanism, and in general the consistency of the Standard Model at the energy above 1 TeV. There also were high hopes for discoveries of new physics as of supersymmetry or extra dimensions. The Higgs boson has been confirmed in 2012 [37] [38], but unfortunately there are no signs of anticipated new physics discoveries. Nevertheless the LHC is by far the most powerfull hadron-hadron collider, previous one being Tevatron at Fermilab which was operational from 1983 till 2011[39] and achieved energies of 2 TeV for proton-antiproton collisions. As such is very capable of precision measurements in the Standard

Model and possibly will be able to deliver surprising results with increasing luminosity during future runs. Furthermore, the high-energy heavy-ion (HI) beams at unprecedented energies allow to further extend the study of QCD matter under extreme conditions of temperature and density.

2.2 The Compact Muon Solenoid

CMS is a general-purpose detector. It has a broad physics programme covering e.g. the Standard Model measurements, dark matter and extra dimensions search and is designed to work in pp as well as HI modes. The main element of the CMS detector is a superconducting solenoid magnet (see Fig. 23). It delivers a magnetic field of 3.8 T. The tracker, electromagnetic and hadronic calorimeters are placed inside the magnet coil, while the muon detectors are built on the outside.

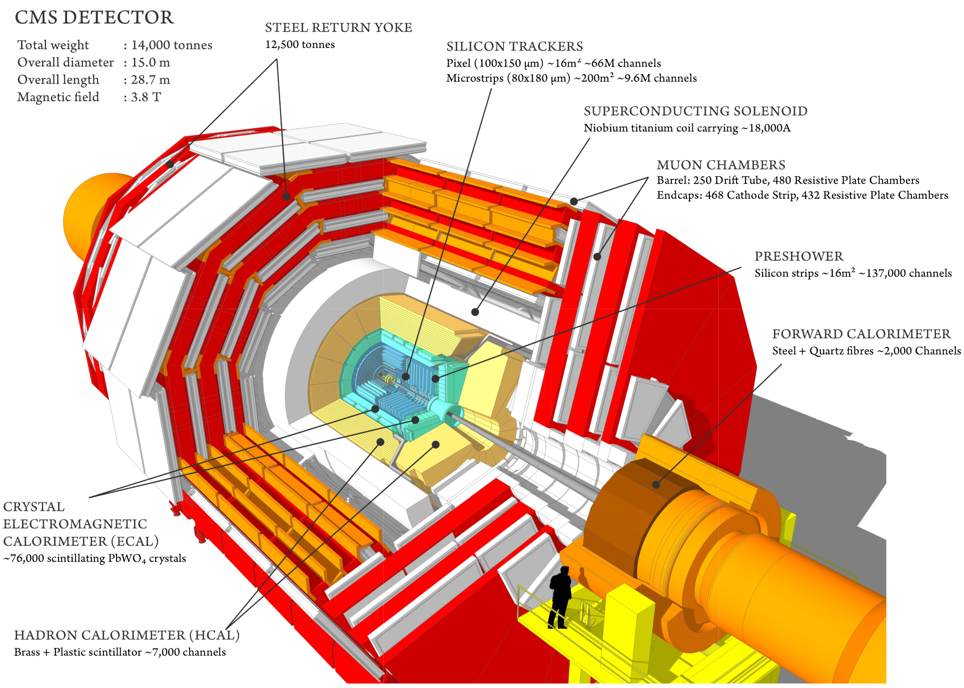

Figure 23: View of CMS experiments with its subdetectors.

In the CMS experiment the following coordinate system is used:

- y-axis is pointing upward,
- x-axis is pointing towards the center of the LHC,
- z-axis points along the beam direction (in counterclockwise direction),
- azimuthal angle ϕ is measured in the x-y plane and from the x-axis,
- r is the radial coordinate in this plane,

- the polar angle Θ is measured from the z-axis,
- η is pseudorapidity and is defined as $\eta = -\ln \tan(\Theta/2)$,
- the momentum and energy transverse to the beam direction are p_T and E_T respectively,
- E_T^{miss} is the imbalance of energy measured in the transverse plane.

The missing transverse energy E_T^{miss} in a collision is a part of the energy, that is not detected in a detector, but is expected because of the laws of conservation of energy and momentum. It is assumed to be carried out by particles that cannot be observed in the detector, such as neutrinos. In order to precisely measure the momenta of charged particles a strong magnetic field is needed.

The CMS detector can be divided into four main parts covering different regions of η: barrel, endcaps, Hadronic Forward calorimeters and very forward detectors. The experiment has been designed to meet the following requirements for the LHC programme:

- muons;
  - good identification,
  - good momentum resolution over a wide range of trajectory directions and momenta (see Fig. 24),
  - dimuon mass resolution of about 1% at 100 GeV,
  - unambiguous information on the charge of muons with transverse momenta < 1 TeV,
- good resolution for charged particles momenta,
- good reconstruction efficiency in the inner tracker,
- efficient triggering and offline tagging of b-jets and τ particles (pixel detectors close to the interaction region),
- good electromagnetic energy resolution (see Fig. 25),
- mass resolution of diphotons and dielectrons of about 1% at 100 GeV and wide geometric coverage,

- π^0 rejection,
- efficient isolation of photons and leptons and
- good resolution for missing-transverse-energy and dijets (see Fig. 26).

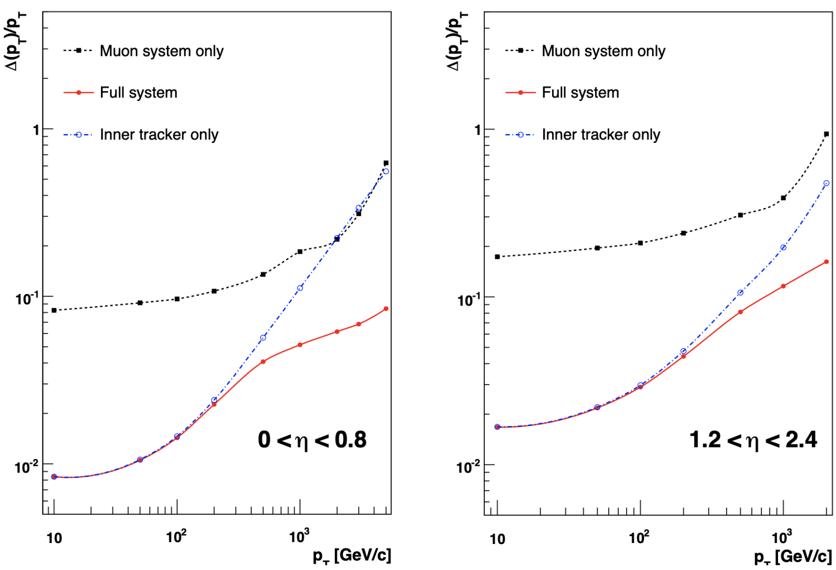

Figure 24: The expected muon p_T resolution as a function of muon p_T. Results are shown for three cases – for muon system only, inner tracker only, and using both sub-detectors. The pseudorapidity range on the left panel is $|\eta| < 0.8$ and on the right panel $1.2 < |\eta| < 2.4$. [30]

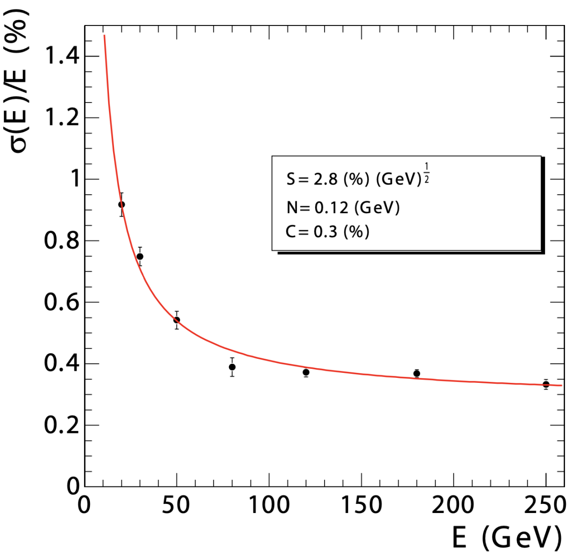

Figure 25: The energy resolution of the electromagnetic calorimeter as a function of electron energy E. The results were obtained from a test, where the beam of electrons impacted the central crystal in a 3 by 3 array. The stochastic (S), noise (N), and constant (C) terms were determined from a fit to the measured points. [30]

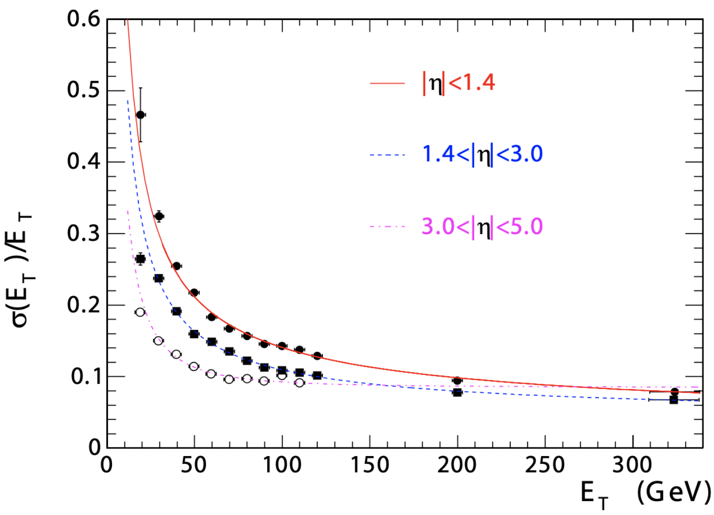

Figure 26: The expected jet E_T resolution as a function of jet's E_T in various pseudorapidity regions – barrel ($|\eta| < 1.4$), endcap ($1.4 < |\eta| < 3.0$), and forward ($3.0 < |\eta| < 5.0$). [30]

2.2.1 The Solenoid Magnet

The superconducting solenoid magnet is a vital part of the CMS detector. Its length is 12.9 m and an inner diameter is 5.9 m (see Fig. 27). It is made of 2168 turns of niobium-titanium (NbTi). The magnet stores 2.6 GJ of energy at full current of 19.5 kA. The 3.8 T field created by the magnet curves the particle's trajectories radially. The curvature of paths of the particles is obtained from the information delivered by the silicon tracker and (for the muons) by the muon detectors. It is used to determine the transverse momenta of the charged particles, p_T.

Figure 27: The picture presents the central device around which the CMS experiment is built: the superconducting magnet. [40]

2.2.2 The Silicon Tracker

The silicon tracker in CMS covers pseudorapidity range of $|\eta| < 2.4$ (see Fig. 28). It allows to accurately reconstruct the tracks of an ionizing particles in that region. This type of detectors are built from a semiconducting material, such as silicon, connected to an electrical circuit. When a ionizing particle passes through the material of the detector it increases the energetic state of the electrons inside its atoms. The electrons that were elevated to the conduction band constitute a pulse of current because of the potential difference applied across the semiconductor. This pulse is then measured as a signal. Because of the high pileup the pixel detector has very high granularity – the size of the pixels is 100×150 μm^2. A microstrip detector on the other hand is built out of a number of identical semiconductor paralel strips.

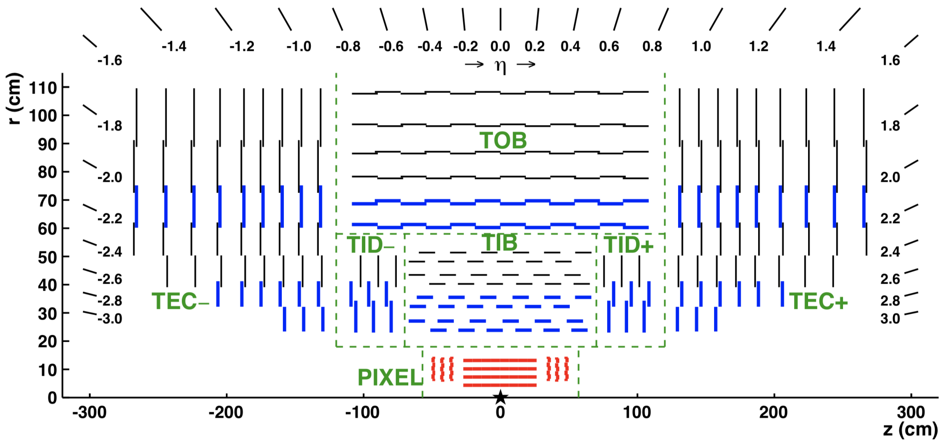

Figure 28: Cross-section diagram of one half of the silicon tracker. [41]

The tracker in CMS consists of two parts: small pixel detector close to the interaction point and a large microstrip detector that surrounds it. The innermost layer, the pixel detectors, are placed from 4.4 cm to 10.2 cm from the beam axis. The barrel part is 53 cm long, consists from 4 layers and ends with the 3 endcap discs. Surrounding the pixel detector is the strip detector. It contains 9.6 million strips and has a total area of 198 m^2. It is made of four sections. Between 20 and 55 cm from the beam axis 4 layers of the silicon microstrip Tracker Inter Barrel (TIB) detectors are placed. Next are 6 layers of silicon microstrips with lower granularity – the Tracker Outer Barrel (TOB). The encdaps are built form the Tracker End Cap (TEC) (9 disks) and the Tracker Inner Disks (TID) (3 disks). The microstrip detectors are cooled down to around -20 °C in order to ensure stable operation. The TIB and TID cover the region of $|z| < 118$ cm and $r < 55$ cm. TIB and TID provide the resolution of 23-34 µm in $r\phi$ and 230 µm in z. The TOB part is built of six layers and covers $|z| < 118$ cm and $r > 55$ cm region. The resolution of TOB is 35-52 µm in $r\phi$ and 530 µm in z. On each end of the strip detector are nine disks of the TEC. The resolution in $r\phi$ is similar to the TOB. TEC covers $124 < |z| < 228$ cm range.

2.2.3 ECAL

The next layer, on the outside of the tracker is the Electromagnetic Calorimeter (ECAL). Its geometric view is presented in Fig. 29. The barrel part of the ECAL detector (EB) covers the pseudorapidity range $|\eta| < 1.479$, while the endcaps (EE) cover the rapidity range $1.479 < |\eta| < 3.0$.

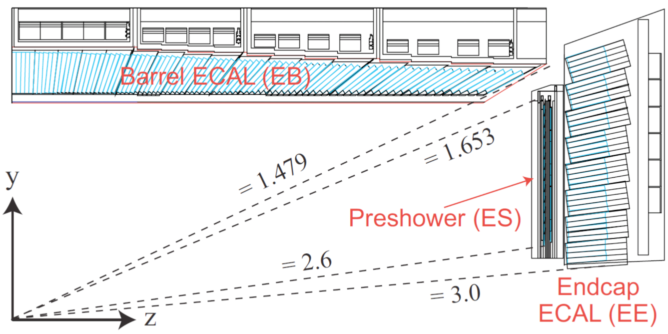

Figure 29: Geometric view of a cross-cestion of one quarter of the ECAL. [43]

ECAL is a scintillation detector with a purpose to measure the energy of photons, electrons and positrons. Scintillation detectors are in general made of solid or liquid materials called phosphors. When struck by an incoming particle these materials emit the energy they have gained as light in a process called scintillation. The light emitted in scintillating material is collected by a photomultiplier tube, which converts it to electric signal, proportional to the number of the emitted photons. The electrical current can then be directly measured. The intensity of light emitted by scintillating material is also proportional to the energy of the particle. Because of this features scintillation detectors are optimal for measuring the energy of the particles. ECAL is built from 75848 high density lead tungstate ($PbWO_4$) crystals. They are characterised by short radiation length $\lambda_0 = 0.89$ cm, which means, that they absorb the energy of photons or electrons/positrons over a short distance. Barrel crystals are 23 cm long (about 26 λ_0) and have a cross-section of 2.2×2.2 cm^2, while in the endcaps the crystals are 22 cm long (about 25 λ_0), and a cross-section of 2.86×2.86 cm^2. Tungstate crystals have high radiation tolerance and a fast response time: 80% of the light in the event is emitted within 25 ns. The ECAL is kept at 0.1 °C.

2.2.4 HCAL

The next layer is the Hadronic Calorimeter (HCAL). It is mostly placed inside the solenoid magnet, with some components are positioned outside the magnet and in forward region. HCAL is divided into four parts (see Fig. 30) – in the central region there is the Hadron Barrel (HB) consisting of of 32 towers and covering $|\eta| < 1.3$ and its extension outside the solenoid, the Hadron Outer (HO). In the forward region the Hadron Endcap (HE) consists of 14 towers, covers a region of $1.3 < |\eta| < 3.0$, containing about 34% of the final-state particles. The Hadronic Forward (HF) covers very high rapidity region up to $|\eta| < 5.0$.

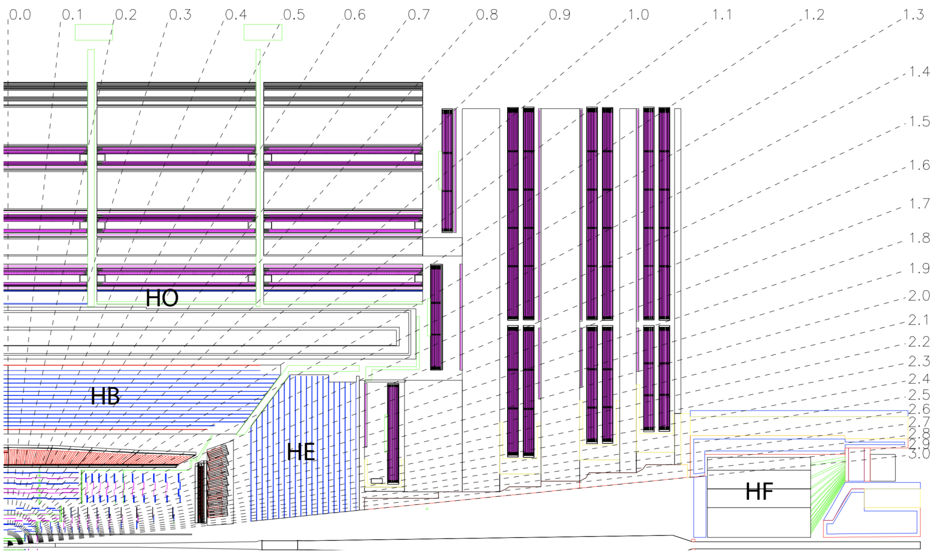

Figure 30: Cross-sectional layout of the HCAL showing its four general sections and the corresponding η ranges. [30]

The HCAL is a scintillation detector. Its purpose is to measure the energy of hadrons i.e. protons, neutrons, pions, etc. For the measurement of the energies and positions of jets it works with the assistance of the ECAL. Compared to the ECAL there is an additional challenge. The scintillation is caused by the ionization of the material, but the interactions of the hadrons with the detector material typically occur by means of the strong nuclear force (e.g. in case of neutrons, which do not directly ionize the material). Therefore the HCAL is built from layers of absorber, where the hadronic interactions take place interspersed with tiles made of scintillation material. The absorber cartridges are made from brass composed in 70% of copper and in 30% of zinc. In order to enable good measurement of the missing transverse energy E_T^{miss}, HCAL was optimised to provide a good hermeticity for hadrons, especially for high $|\eta|$.

2.2.5 HF

The HF is situated at 11.2 m from the interaction point along the beam pipe. The position of the forward calorimeter is shown in Fig. 30 in bottom-right corner. It is a cylinder of an outer radius of 130.0 cm. The internal hole for the beam pipe has a radius of 12.0 cm. The HF has two parts: the HF+ and HF- corresponding to positive and negative values of pseudorapidities. It consists of 36 azimuthal towers – 18 per side of interaction point. The cross-section of the HF is shown in Fig. 31.

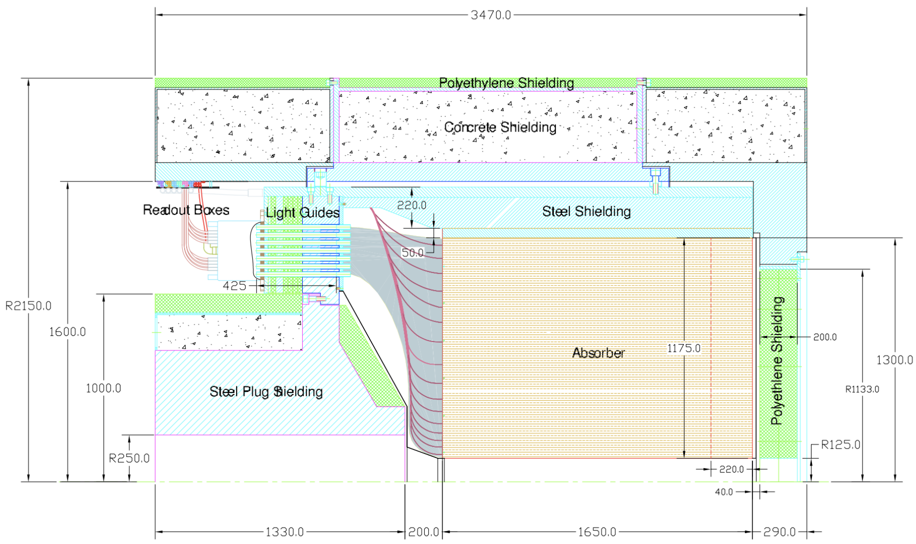

Figure 31: The cross-sectional view of the HF calorimeter. The interaction point of the CMS is to the right-hand side with respect to the presented diagram. All dimensions are given in mm.

This calorimeter is built of 5 mm thick grooved steel plates. In these grooves the fibres are inserted. The fibres are the active medium, made of quartz and hard, polymer coating. The reason for choosing quartz is very high particle fluxes, both HF calorimeters are experiencing. About 760 GeV per proton-proton interaction is deposited into HF calorimeters, while for the rest of the detector it is only 100 GeV. Therefore, as the detector is expected to survive at least a decade in this environment, quartz has been chosen for its radiation hardness. When the particle produces Cherenkov light, the signal is generated and transferred by the fibres. Half of the fibers run through whole depth of the steel absorber, while the other half start after the first 22 cm from the front of the detector i.e. the part facing the interaction point (right-hand side in Fig. 31). The reason for this is that electrons and photons deposit a large fraction of their energy during the first 22 cm, hadrons, on the other hand, produce equal signal on average. By having part of the fibres starting after this first 22 centimeters it is possible to distinguish between showers produced by those particles. The steel absorber alone weights 108 tones and both HF calorimeters are aligned within 1 mm with respect to the CMS experiment.

2.2.6 The Muon System

One of the central importances for CMS is precise and robust measurement of muons. The fundamental requirements for the muon system are good muon identification and precise measurement of their momenta. This subdetector is a key part of the experiment from the point of view of the analysis presented in this thesis.

The muon system is the outermost part of the CMS detector. The only charged particles that reach this region are muons, all others are stopped in ECAL and HCAL. The system is built out of three types of gas-filled chamber detectors (see Fig. 32):

- Drift Tubes (DT),
- Cathode Strip Chambers (CSC),
- Resistive Plate Chambers (RPC).

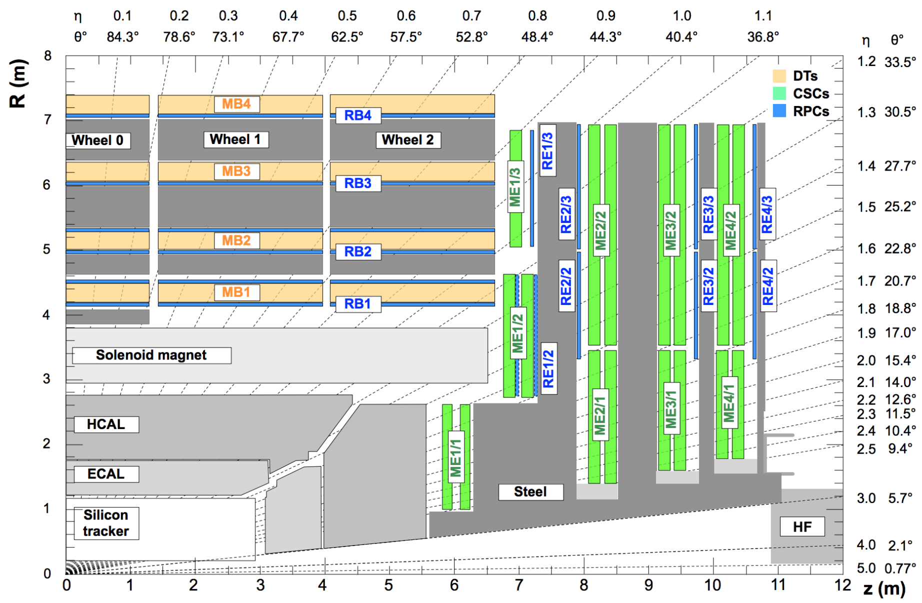

Figure 32: Figure shows the R-z cross-section of the CMS detector. The interaction point is located at the bottom-left corner. All three muon subsystems, DT, CSC nad RPC are marked.

Gas-filled chamber detectors are built from a conducting cylinder filled with gas. Along the cylinder's axis runs a wire. A high voltage is applied between the cylinder (cathode) and the wire (anode). When a particle passes through the detector it causes the molecules of the gass to ionize. The electric potential accelerates the ions in the gas what results in a pulse of current corresponding to the signal. This technology allows to build relatively large detectors.

DT chambers are located in the barrel, they cover the pseudorapidity region of $|\eta| < 1.2$. DT consists of 4 stations that form concentric cylinders around the beam line – MB1, MB2, MB3 and MB4 with radii measured from the beam axis 4.0, 4.9, 5.9 and 7.0 m accordingly. In z direction the system has been divided into 5 wheels, each segmented into 12 sectors in the azimuthal angle ϕ. In each sector of 30 ° and given layer there is one DT chamber, the exception being the most outer layers in each of the five wheels, where in two sectors, the top and the bottom one, there are two chambers.

CSCs are located in the endcaps, as shown in Fig. 32. The CSCs are multiwire proportional chambers made of 6 anode wire planes placed inbetween 7 cathode panels. Wires run azimuthally and give information on track's radial coordinate. Strips run at constant width in ϕ coordinate. This system extends up to $|\eta| < 2.4$. In each endcap they form four disks perpendicular to the beam direction (ME1, ME2, ME3 and ME4, where the first of these is the innermost disk). Disks are divided into 2 (ME2, ME3) or 3 (ME1) concentric rings. During Run 1 the last disk (ME4) consisted of only one ring. In 2013-2014, during the Long Shutdown 1 (LS1), few important upgrades of the muon system have been performed. The outermost rings of CSC and RPC chambers in the fourth station of endcaps have been completed (ME4/2, RE4/2 and RE4/3). Since the Run 2 the new rings cover the $1.2 < |\eta| < 1.8$ region.

RPC's goal is to combine good spatial and a very high time resolution. They operate in an avalanche mode and their time response comparable to that of scintillators. RPC is tagging the time of an ionising event in a much shorter time than the 25 ns between two LHC bunch crossings. Their position granularity is worse than for the DT and CSC. They cover the region up to $|\eta| < 1.6$. There are four layers of RPC in the endcaps region.

2.2.7 Forward Detectors

CMS is designed to have high coverage in pseudorapidity (see Fig. 33), i.e. it has additional detectors in forward region (high $|\eta|$).

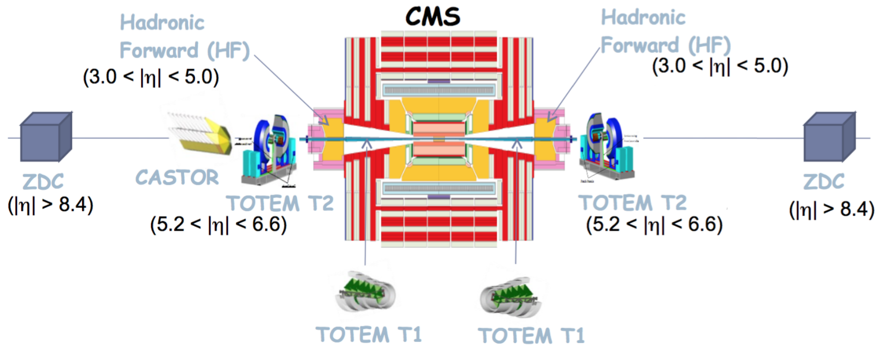

Figure 33: Forward sub-detectors in the CMS. On both sides there are HF calorimeters, TOTEM and ZDC detectors. CASTOR calorimeter is installed on one side only.

The CASTOR (Centauro And STrange Object Research) calorimeter is one of very forward detectors in CMS. It is located 14.37 m from the interaction point at the negative pseudorapidity region. It was originally planned that there would be the second detector of same type, POLLUKS located at the positive side, but it was never built due to financial constraints. CASTOR covers a pseudorapidity range of $5.2 <| \eta |< 6.6$. That corresponds to particles scattered at an angle of around 0.2° with respect to the z-axis. CASTOR and its readout design permits the observation of the cascade development of the particles inside of the calorimeter. The typical energies can be measured with a resolution better than 1%. The calorimeter absorber material has been selected to minimize the size of the shower. It is made of tungsten which forms a number of plates with thinner quartz plates placed between them. Electrons and positrons from a developing cascade produce Cherenkov light in the quartz plates. The main advantages of quartz calorimeters are radiation hardness, compact dimensions and fast response. This makes CASTOR suitable for the harsh conditions in the very forward region in CMS.

A set of two identical Zero Degree Calorimeters (ZDC) are designed to complement the CMS very forward region. They cover the pseudorapidity region of $|\eta| > 8.3$ for neutral particles and are located between the two LHC beam pipes at about 140 m on each side of the CMS interaction region. ZDCs measure only the forward neutral component of the interaction. The charged particles are bent by the superconducting dipole magnets steering the beams and therefore are not in the calorimeters acceptance region. The ZDC detector made of tungsten absorber interleaved with quartz fibers as an active material. The ZDCs are 74 cm long and have a radius of 4 cm. ZDCs were designed especially for heavy-ion and proton-proton diffractive studies. Each ZDC detector consists of two parts – the electromagnetic (EM) with 5 logical units and hadronic (HAD) with 4 units in depth (see Fig. 34).

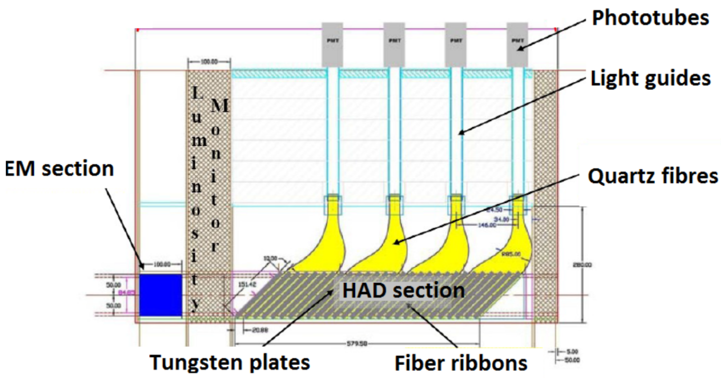

Figure 34: A side view of the ZDC with the EM section in front and the HAD section behind. The interaction point of the CMS is to the left-hand side with respect to the presented diagram.

The EM section measures forward photons. The electromagnetic showers produced by the photons are stopped in the EM part. This section is 19 electron radiation lengths long. The forward 50 GeV photons can be measured with an energy resolution of 10%. The HAD section measures forward neutrons. The length of the HAD section is 5.6 hadronic interaction lengths.

Due to its high coverage in the forward region and advanced muon system CMS is well suited for heavy ions analyses.

2.2.8 Trigger

During pp collisions in the LHC the bunch spacing is 25 ns, what results in 40 MHz interaction rate. The pile-up during Run 2 was very high, exceeding 60. Due to limited computing and storage resources it is not possible to save that amount of data for all collisions. Furthermore, most of these events are not interesting. As shown in Fig. 35 the rates of the processes that can be studied at LHC span many orders of magnitude and the most interesting ones are the very rare phenomena. Therefore only the most interesting events are chosen for the offline storage by a trigger system.

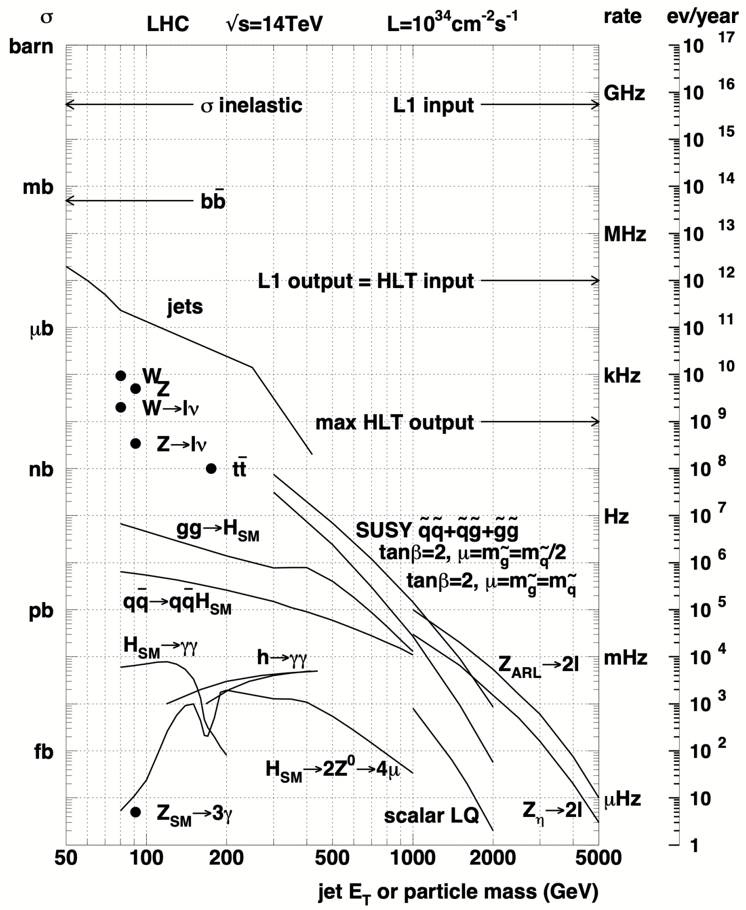

Figure 35: Inclusive pp cross-sections for basic physics processes that can be studied at the LHC shown as a function of jet's E_T or mass of a particle. On the right-hand scale the yearly rates are shown for luminosity of $L = 10^{34}$ cm^{-2} s^{-1}. [44]

The CMS trigger is a two-level system consisting of Level 1 (L1) triggers implemented in hardware and High Level Triggers (HLT) software algorithms running on approximately 26000 commercial cores. The L1 triggers have less then 4 microseconds for the decision based on the coarsely segmented data from the muon detector and calorimeters. The high-resolution data is holded in pipelined memories during this time. The information from the tracker is not available at the L1 and the selection is based on data from calorimeters and muon system. The input to the calorimeter trigger system comes from ECAL, HCAL and HF, while to the muon trigger from its three subdetectors, DT, CSC and RPC. All the information from calorimeter and muon triggers is merged and the Global Trigger decides on rejecting or accepting an event and sending it to the HLT for more detailed analysis. After the L1 the rate is reduced to 100 kHz. In the case of the HI runs there is no pile-up and the interaction rates are lower due to the typically very high occupancy for these events and limitations of the readout system. For example during the 2018 PbPb run the bunch spacing was 75 ns i.e. the interaction rate was about 13.3 MHz. Therefore during HI collisions only a factor of the order of 10 reduction in L1 trigger rate is needed.

The HLT reduces the data rate down to approximately 1 kHz. It uses full detector information enabling complex calculations similar to the off-line analysis.

The HLT consists of hundrets of algorithms corresponding to a dedicated trigger. Each of them is composed of a sequence of reconstruction and filters – when an event does not pass the filter the next modules are not run. The resulting data at the rate of up to 1 kHz is stored on disk for full reconstruction and further analysis. In order to avoid the saturation of the data taking bandwidth the output rate of the L1 trigger and the HLT can be decreased by prescaling the number of events that pass the algorithms. The prescale value determines what fraction of events is passing after the HLT selection. During the offline analysis the prescale factor for given dataset and used trigger has to be evaluated in order to get the actual integrated luminosity of the used data sample.

2.2.9 Physics Objects

For the reconstruction of physics object in CMS the Particle Flow (PF)[45] method is used. This is a holistic approach, which uses and correlates information from all detector layers to give the event description with final-state particles' and their properties. CMS is well suited for PF reconstruction because of its precise tracking system, highly segmented calorimeters, strong magnetic filed and a robust muon subsystem. The sketch showing hermetic CMS design is presented in Fig. 36. The PF algorithm allows to identify electrons, muons, photons, neutral and charged hadrons. With this list of particles it is possible to determine missing energy, jets, hadronic taus etc.

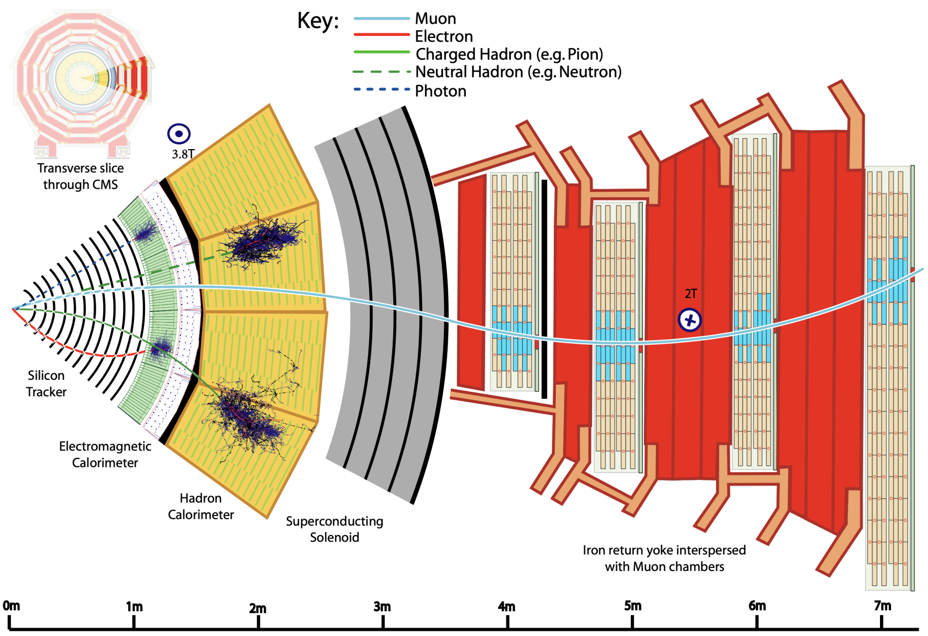

Figure 36: Cross-sectional sketch of interactions of specific particles in all layers of the CMS detector. The showers of particles in calorimeters are detected as clusters of deposited energy. Only neutrinos can escape the detector undetected.[45]

In case of the muons the tracks are reconstructed based on the information from the tracker and the muon segments. The tracker gives very precise measurement of the muon's momenta and the muon subsystem, because of it's placement on the outside of the calorimeters absorbing most of the particles other than muons and neutrinos (see Fig. 36), has very high reconstruction purity. There are three types of reconstructed muons:

- global muons have a tracker track matched to the track from muon system. Hits in at least two layers in the tracker are required. They are most efficient for high p_T muons.
- tracker muons have reconstructed track from the tracker matched to at least one muon segment. They have good reconstruction efficiency for low p_T muons.
- standalone muons, which are built only based on the muon system information, and therefore usually have higher cosmic muon contamination and worse p_T resolution compared to the previous types.

For the rest of the PF-particles the tracks are reconstructed together with building separate clusters form ECAL and HCAL. The tracks are linked with clusters what defines the blocks from witch the particles together with their properties such as energies and directions are created. All reconstructed PF particles can be straightforwardly used in physics analyses.

The jets are created starting with protojets, which can be individual PF particles or bunches of overlapping particles. Then the anti-kT algorithm [46] is employed to cluster either all PF particles (PF jets), or the sum of the energy deposited in the calorimeter towers, which in turn are composed of an HCAL tower and 25 ECAL crystals below it (Calo jets).

The presence of final state particles, that cannot be directly observed in the detector, e.g. neutrinos are concluded from the missing transverse momentum $\vec{p}^{miss}_{\mathrm{T,PF}}$ (which is often referred to as missing transverse energy). The raw missing transverse momentum $\vec{p}^{miss}_{\mathrm{T,PF}}(\mathrm{raw})$ balances the sum of $\vec{p}_T$ of all the particles:

$$\vec{p}^{miss}_{\mathrm{T,PF}}(\mathrm{raw}) = -\sum_{i=1}^{N_{\mathrm{particles}}} \vec{p}_{\mathrm{T},i}. \tag{13}$$

3 Recent measurements of UPC vector meson production

There are not many results of the UPC vector meson production in the hadron collisions. In particular the Υ photoproduction has been measured only in pPb data. In this chapter two recent analyses performed by the CMS collaboration are presented.

3.1 Exclusive Υ photoproduction in pPb data

In a recent analysis[47] the CMS collaboration measured the exclusive photoproduction of Υ meson in pPb data from Run 1 with the integrated luminosity of 32.6 nb^{-1}. The center-of-mass energy per nucleon pair was $\sqrt{s_{NN}}$ = 5.02 TeV. The studied process is the photoproduction of the Υ meson, $\gamma p \rightarrow \Upsilon(nS)p$ (with n = 1, 2, 3) in the ultra-peripheral collisions. The Υ(nS) resonance has ben studied in the $\mu^+\mu^-$ decay chanel. The STARLIGHT Monte Carlo generator [48] is used for the simulation of the background and signal processes. The following event selection has been applied: at least one candidate from the muon detectors and 1-6 tracks in the event at the trigger level. Only muon pairs of opposite charge with reconstructed p_T between 0.1 and 1 GeV are considered in the offline analysis.

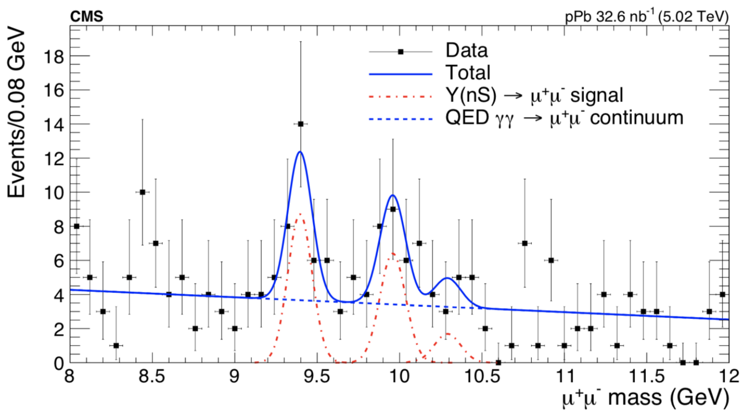

Figure 37: Invariant mass distribution of the $\mu^+\mu^-$ pairs. The fit consists of a linear function for the continuum (dashed line) and three Gaussian distributions for the three Υ states (dashed-dotted curves). [47]

Both muons must have $p_T^{\mu} > 3.3$ GeV, a single vertex (come from the same interaction point) and no extra charged particles with $p_T > 0.1$ GeV can be associated with that vertex. The exclusivity of the event is ensured by additional requirement on the largest Hadronic Forward subdetector tower energy deposit to be below 5 GeV. The resulting invariant mass distribution of the muon pairs is presented in Fig. 37. Figure 38a presents the $\Upsilon(1S)$ cross-section values for the rapidity range $|y| < 2.2$, corresponding to the photon-proton centre-of-mass energies in the range $91 < W_{\gamma p} < 826$ GeV. It can be seen, that the differential cross-section, $d\sigma/dy$, varies for different theoretical modeling. The results are consistent with most theoretical predictions and JMRT-LO (Jones, Martin, Ryskin and Teubner [49]) gives systematically higher values. The statistical precision will increase with more data and as can be seen this measruement will be able to distinguish between the different models. During Run 2, in 2016 CMS experiment collected about 180 nb^{-1} of pPb data (36 nb^{-1} in 2013) at $\sqrt{s_{NN}} = 8.16$ TeV. Fig. 38b presents the cross-section as a function of $W_{\gamma p}$. The results are compared against the measurements from H1 and ZEUS at the Deutsches Elektronen-Synchrotron (DESY) and Large Hadron Collider beauty (LHCb) together with theoretical models. The CMS results bridges the previously unexplored W region between LHCb and HERA. The JMRT-LO results show the steepest increase of the cross-section.

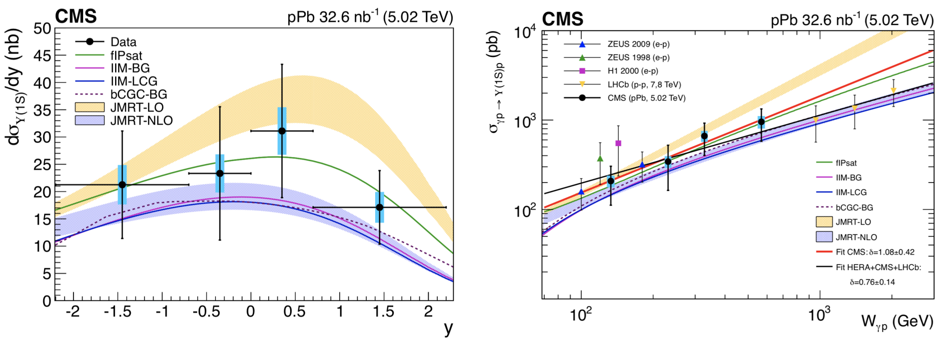

(a) (b)

Figure 38: Panel (a): differential $\Upsilon(1S)$ photoproduction cross-section as a function of rapidity y. Panel (b): cross-section for exclusive $\Upsilon(1S)$ photoproduction as a function of photon-proton centre-of-mass energy W. [47]

3.2 Exclusive J/ψ photoproduction in PbPb data

The CMS collaboration also studied UPC coherent photoproduction of J/ψ meson in PbPb data[50]. The used data sample has been collected during 2011 at $\sqrt{s_{NN}} = 2.76$ TeV. The integrated luminosity was 159 μb^{-1}. The cross-section has been obtained for the case, when there was at least one neutron on one side and no neutron activity on the other side of the interaction point, denoted by $X_n 0_n$. This requirement suppresses the background contribution from the hadronic interactions between the ions. The neutrons were detected using the ZDC. The process has been studied in the $\mu^+\mu^-$ decay chanel. The dedicated L1 trigger selecting events with at least one neutron in the ZDC and at least one muon without requirement on the p_T has ben used. To ensure the exclusivity it was required, that there are exactly two tracks and that the energy deposited in any HF cell is below 3.85 GeV. Then the opposite-sign muon pairs with $p_\mathrm{T} < 1.0$ GeV, rapidity $1.8 < |y| < 2.3$ and reconstructed invariant mass in the range 2.6 GeV $< m <$ 3.5 GeV were selected. The contributions from the coherent and incoherent processes and

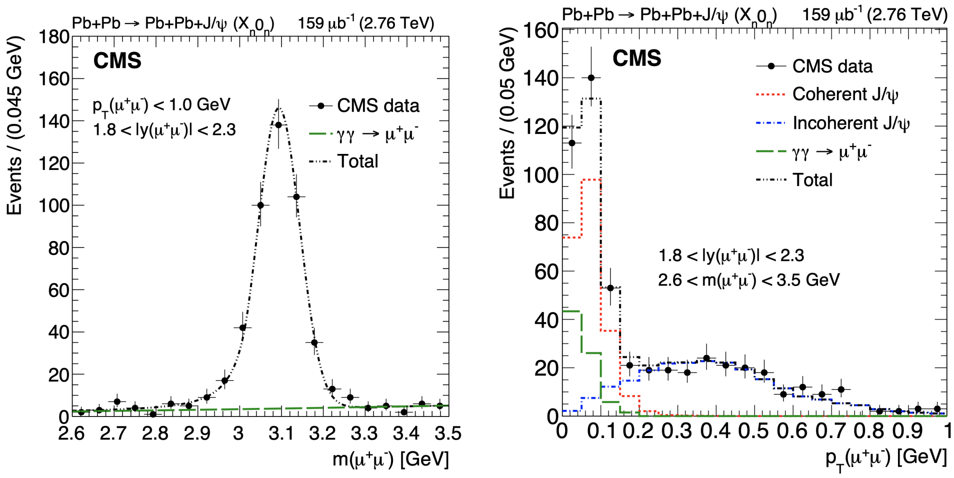

(a) (b)

Figure 39: The plots show the results from the simultaneous fit to dimuon invariant mass (panel (a)) and p_T (panel (b)) distributions. The red, blue and green curves represent coherent J/ψ, incoherent J/ψ and γγ components respectively. The shapes of the contributions have been obtained from the STARLIGHT MC after the detector response simulation. [50]

QED background have been obtained by simultaneous fitting to the dimuon invariant mass and p_T distributions. The results are presented in Fig. 39. The ratio of the cross-section of the $X_n 0_n$ mode to the total cross-section has been obtained with STARLIGHT and the total cross-section of the coherent photoproduction has been also evaluated in this analysis. The resulting cross-section is presented in Fig. 40. The data from CMS and ALICE disfavour the impulse approximation which does not include nuclear effects and are consistent with the leading twist approximation model prediction, which includes nuclear gluon shadowing effect.

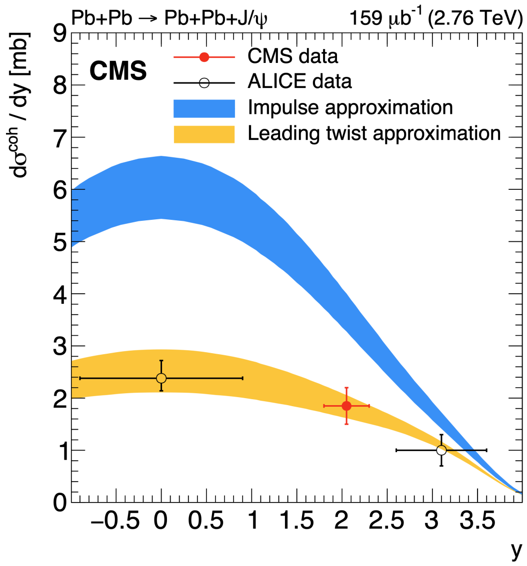

Figure 40: Differential cross-section versus rapidity for coherent J/ψ production in PbPb UPC data at $\sqrt{s_{NN}} = 2.76$ TeV is presented together with result by ALICE[15] and theoretical predictions. The vertical bars represent the systematic and statistical uncertainties. The data is consistent with the leading twist approximation model, which includes nuclear gluon shadowing. [50]

4 The analysis

4.1 Monte Carlo simulations

In order to understand an outcome of a measurement in particle physics it is indispensable to properly account for the response of the detector, that has been used. The measured value is a product of detector's properties and underlying physical processes. In case of complex aparatus such as CMS the analytic approach is not possible. In order to account for the interplay between all the parts of the detector the numerical Monte Carlo (MC) simulations are used. First step is to generate the particles according to given theoretical predictions (generation level – GEN). During the next step the statistical effects of particles interacting with parts of the detector are modeled and the output of the detector's electronics is simulated (simulation – SIM). Next this output is reconstructed with the same software as the real data and the produced files can be directly compared to the collision data (reconstruction level – RECO).

4.1.1 STARLIGHT

In order to generate MC samples the STARLIGHT event generator [48] has been used. Three samples were prepared: the coherent and incoherent Υ photoproduction (Fig. 41 panel a) and b) respectively), and the exclusive QED process, $\gamma\gamma \rightarrow \mu^+\mu^-$, where the two photons from both nuclei interact with each other to produce oppositely charged muon pair (panel c) in Fig. 41). The coherent and incoherent Υ photoproduction samples simulate the signal process, that need to be separated into these two modes. The main background is simulated by the QED $\gamma\gamma \rightarrow \mu^+\mu^-$ sample, where the muon pairs are produced in a wide invariant mass spectrum.

STARLIGHT is a C++ MC program that focuses on simulations of ultra-relativistic collisions at CERN's LHC and Brookhaven's RHIC (Relativistic Heavy Ion Collider) and is capable of simulating a range of photo-nuclear and two-photon interactions with a variety of possible final states including vector mesons. In case of purely electromagnetic interaction, the two photons from nuclei's electromagnetic fields interact and can couple to any charged particles. In the photonuclear interaction on the other hand, the most common final state is a vector meson, which decay is simulated with

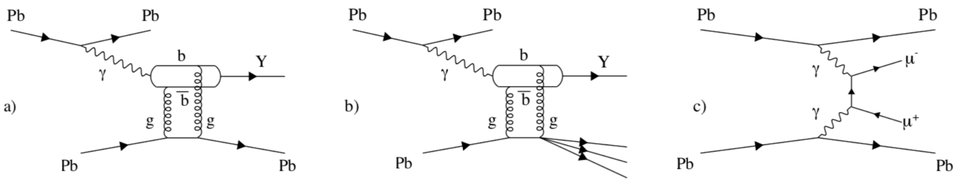

Figure 41: The Feynman diagrams of the UPC processes. Panel a) shows the exclusive Υ photoproduction, panel b) hadron dissociative (incoherent) Υ photoproduction and panel c) the exclusive $\mu^+\mu^-$ QED continuum production, the main background to the analysed process.

consideration of its parity and spin. The masses and widths of the particles are the standard Particle Data Group values [5].

In the STARLIGHT model the probe is provided by the photon flux from the incoming hadrons described by the Weizsäcker-Williams approximation. The initial state of the nucleus is given by the vector meson dominance (VMD) model [51] fit to the HERA (Hadron-Electron Ring Accelerator) proton-electron data, Glauber model [52]. In the VMD picture, photons have hadronic components and can fluctuate to quark-antiquark pairs, which scatter elastically from the nucleus. The semiclassical Glauber formalism describes the nucleus-nucleus interactions in terms of the constituent nucleons with a given density distribution. The nuclear cross-sections in STARLIGHT are obtained from this model.

STARLIGHT takes an input configuration file, where the atomic and charge numbers of projectile and target ions and their energies, center-of-mass energy W of the produced system, kinematic ranges of the produced particles, and break-up modes are set. This step can be done on personal computer and the output is in ASCII format. In the produced QCD $\gamma\gamma \rightarrow \mu^+\mu^-$ sample it is required that the enter-of-mass energy, $W > 6$ GeV. Without this requirement most of the events would be simulated in a region of low W, not useful for this analysis, unnecessarily using the computational and storage resources. The threshold of 6 GeV has been set below the range of the considered invariant mass spectrum (8 - 12 GeV). All three produced STARLIGHT samples have only a $\mu^+\mu^-$ pair in the final state. No constraints are set on rapidity or p_{T} of the produced particles for any sample. The distribution of the invariant mass M of the dimuon system, $\mu^+\mu^-$ for generated level QCD sample is shown in Fig. 42. The p_T and rapidity distributions for single muons, which were normalised to 1 are shown in Figures 43 and 44. The distributions for dimuons are presented in Figures 45 and 46. The QCD sample has 2×10^6 events and coherent and incoherent Υ samples have 5×10^5 events each.

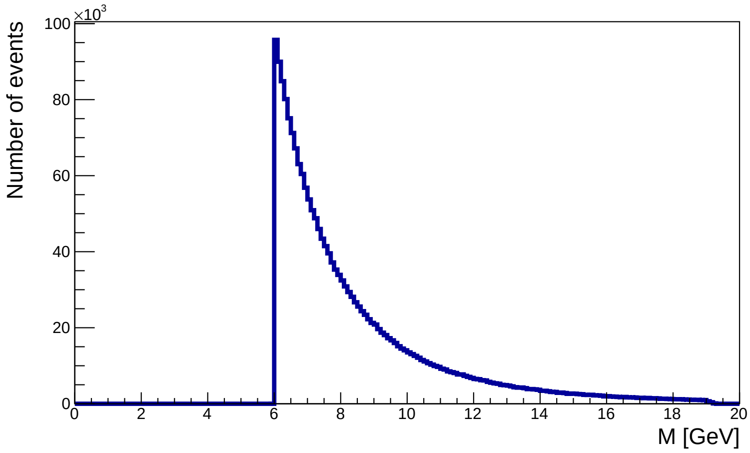

Figure 42: The generator level dimuon invariant mass distribution of the $\gamma\gamma$ MC sample obtained with STARLIGHT. The center-of-mass energy W is required to be above 6 GeV.

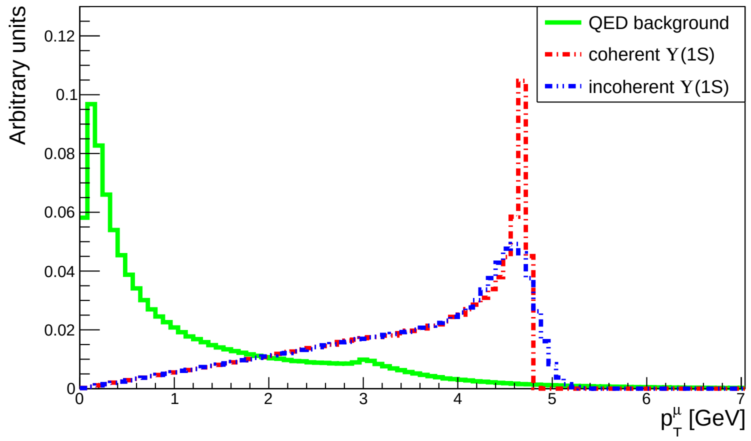

Figure 43: The normalised generator level single muon p_{T} distributions of the $\gamma\gamma$, coherent and incoherent Υ photoproduction MC sample obtained with STARLIGHT. The small peak at 3 GeV for the QED sample is due to $W > 6$ GeV requirement. Most of muons for both coherent and incoherent Υ samples have p_{T} around half of the Υ mass.

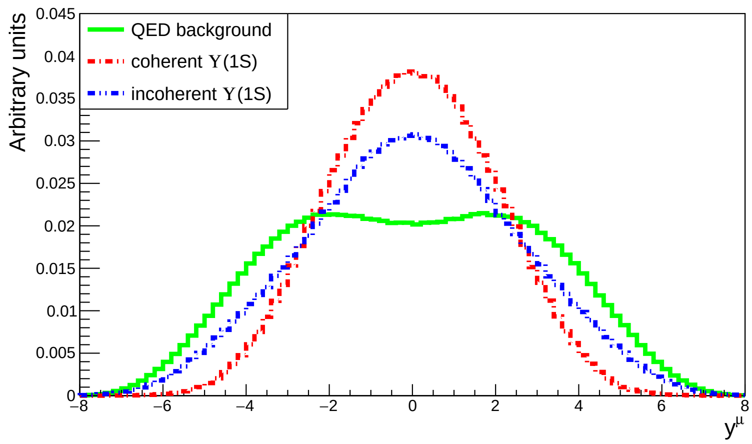

Figure 44: The normalised generator level single muon rapidity distributions of the $\gamma\gamma$, coherent and incoherent Υ photoproduction MC sample obtained with STARLIGHT. The muon system subdetectors in CMS have a range of $-2.4 < \eta < 2.4$, which coveres about a half of the number of produced particles.

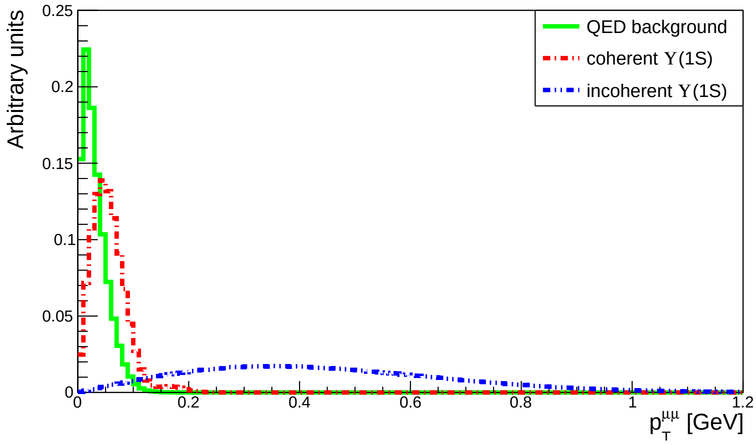

Figure 45: The normalised generator level dimuon p_{T} distributions of the $\gamma\gamma$, coherent and incoherent Υ photoproduction MC sample obtained with STARLIGHT.

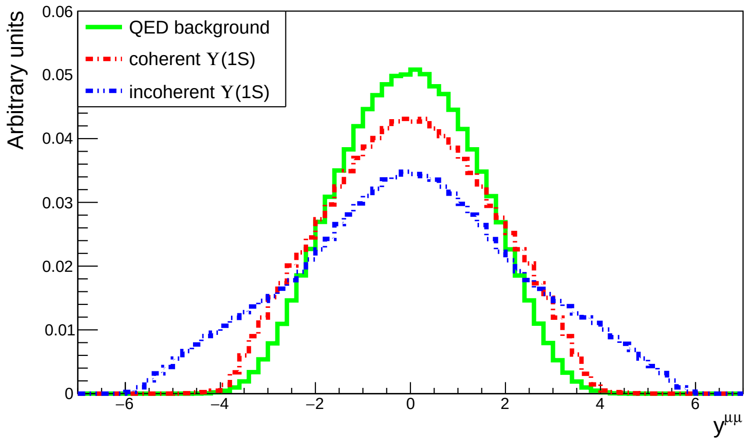

Figure 46: The normalised generator level dimuon rapidity distributions of the $\gamma\gamma$, coherent and incoherent Υ photoproduction MC sample obtained with STARLIGHT.

4.2 Data Preparation

The output files obtained from STARLIGHT are converted to the Les Houches Event (LHE) [53] format. The LHE files are divided into subsamples in order to be further processed in parallel. During the next step the files are used as an input to the CMS software framework (CMSSW). This and next steps are done with use of the Worldwide LHC Computing Grid (WLCG)[56], a global collaboration of around 170 computer clusters. The generated particles are propagated through the GEANT4 [54] simulation, which accounts for all the interactions with the CMS detector. Next the reconstruction software (the same as the one used for the data taking) is used to produce the final files in the Analysis Object Data (AOD) format. These files contain reduced information that will be needed for the analysis. Finally, for both collision data and MC simulations, the skimmed files are produced. They contain only information useful for given analysis and are small enough to be used on personal computer. They were finally analysed with ROOT[55], a framework developed by CERN and designed for the analysis of the particle physics data.

The analysed data sample[1] used in this analysis has been collected during 3 week period of the PbPb collisions at the end of 2018 at $\sqrt{s_{NN}} = 5.02$ TeV. It has integrated luminosity of $L_{\text{int}} = 1621.6\ \mu\text{b}^{-1}$.

[1]The dataset used in the analysis is denoted as "/HIForward/HIRun2018A-04Apr2019-v1/AOD".

4.3 Muon Acceptance and Efficiency

Because of its broad coverage for muon's η and p_{T} and high number of produced events, the $\gamma\gamma$ MC sample has been used for the muon acceptance and efficiency studies. In order to select a kinematic region for the analysis, the efficiency, $\epsilon_{\mathrm{ID,trigger}}$, dependence in the muon's η and p_{T} bins is evaluated as a fraction of the number of reconstructed muons that pass the given muon identification (ID) and fulfil the given trigger requirement, $N_{\mathrm{RECO}}^{\mathrm{soft,triggered}}$ to the number of the generated muons, $N_{\mathrm{GEN}}^{\mathrm{muon}}$:

$$\epsilon_{\mathrm{ID,trigger}} = \frac{N_{\mathrm{RECO}}^{\mathrm{soft,triggered}}}{N_{\mathrm{GEN}}^{\mathrm{muon}}}. \tag{14}$$

The muon ID used in this analysis is the "Soft Muon ID": muon tracks need to be high purity tracks (as defined in Section 4.4 of [57]), have at least 6 tracker layers and at least one hit in the pixel detector. They have to be consistent with a hit in at least one segment in any station of the muon system and the tracks can be at most 3 mm in the transverse direction and 20 cm in the longitudinal direction from the nearest primary vertex.

Events have to match the trigger[2], which requires that there is at least one muon which is required to match 2 or more stations in the muon system without any requirement on the p_{T}. Additionally at least one HF is required to have low deposit of energy.

In Fig. 47 the scatter plot of the generated muons is presented in the η and p_{T} bins from the $\gamma\gamma$ MC sample. Muons cover a wide range of η and p_{T} and can therefore be used for the efficiency study. Fig. 48 presents all the muons form this sample, that passed the reconstruction algorithms. The η and p_{T} of the muons are taken at the generation level. The kinematic region for the muons selected for this analysis is shown in Fig. 49 with red line. The acceptance selection is set to reach least 10% efficiency. This threshold is a standard value used by the heavy-ion Physics Object Group in CMS and is a compromise between number of muons kept in the analysis and the uncertainty. The selected region details are presented in Table 4.

[2]The used trigger is called "HLT_HIUPC_SingleMu0_NotMBHF2AND_v1".

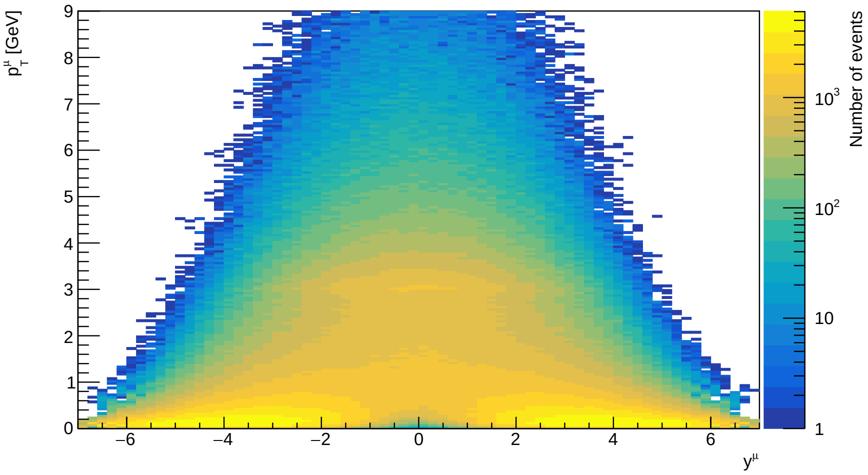

Figure 47: Generator level muons obtained with the $\gamma\gamma$ MC sample simulated with STARLIGHT as a function of muon's rapidity and p_{T}. Most of the muons are produced at low transverse momenta, $p_{\mathrm{T}} < 1$ GeV, but thanks to large number of 2 M produced events (i.e. 4 M muons) there is high number of muons covering wide kinematic region.

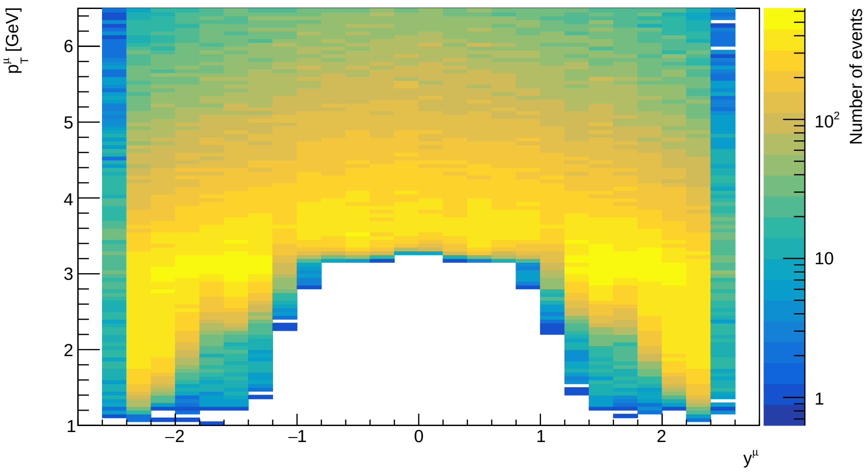

Figure 48: Reconstruction level muons obtained with the $\gamma\gamma$ MC sample simulated with STARLIGHT fulfilling the Soft ID and trigger requirement as a function of muon's generator level rapidity and p_{T}.

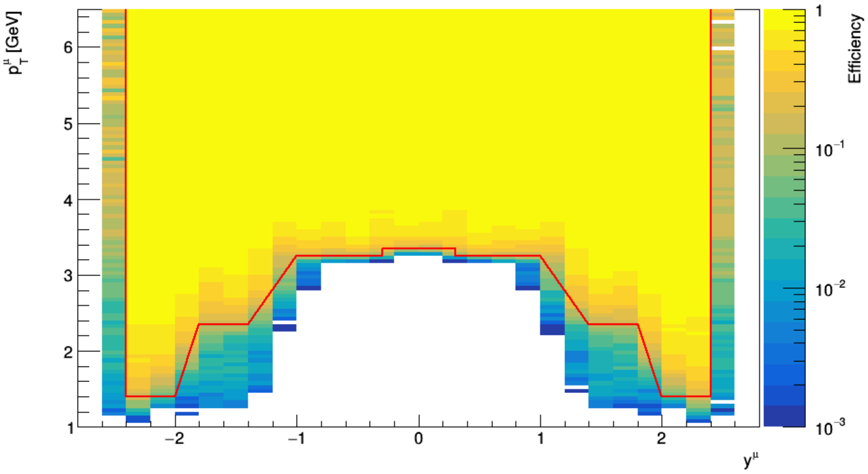

Figure 49: Efficiency obtained with the $\gamma\gamma$ MC sample simulated with STARLIGHT. The red line represents the acceptance selection profile around a regions with at least 10% efficiency.

Table 4: Acceptance region based on the 10% efficiency profile obtained form the MC. The p_T is given in GeV units. Additional $|\eta| < 2.4$ requirement is applied for the whole p_T range.

$\|\eta\|$ region	p_T thresholds
$\|\eta\| < 0.3$	$p_T > 3.35$
$0.3 < \|\eta\| < 1.0$	$p_T > 3.25$
$1.0 < \|\eta\| < 1.4$	$p_T >$ (-2.25$\times\|\eta\| + 5.5$)
$1.4 < \|\eta\| < 1.8$	$p_T > 2.35$
$1.8 < \|\eta\| < 2.0$	$p_T >$ (-4.75$\times\|\eta\| + 10.9$)
$2.0 < \|\eta\| < 2.4$	$p_T > 1.4$

4.4 Event selection

Events are required to pass the trigger and both muons have to fulfil the Soft ID requirements. Additionally, in order to suppress events with hadronic interactions, exclusivity cuts are applied. First, it is required that there are exactly two tracks in the detector. Only events with maximal energy deposited in any tower in HF detectors below noise threshold are selected. The values are slightly different for HF+ and HF- because of different radiation damage and are set to 7.3 GeV for HF+ and 7.6 GeV for HF-. They are determined from data collected by the Forward CMS group when the beams were not present in the LHC and are selected so that 99% of the events with lowest HF occupancy are kept. In Fig. 50 the energy spectra together with the obtained energy spectrum thresholds are presented. The trigger thresholds are much looser than the ones shown in Fig. 50. This ensures, that there are no events rejected before the offline analysis. Additionally both muons are required to have $|\eta| < 2.4$ and be of the opposite sign.

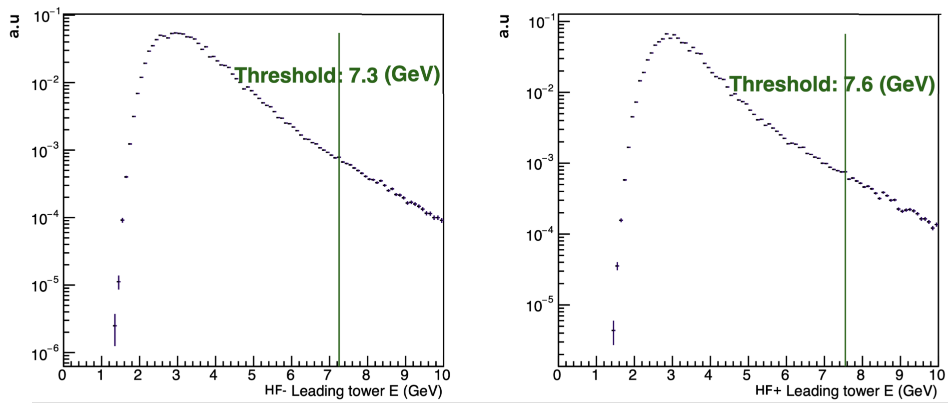

Figure 50: Plots present leading tower energy distributions for No BPTX data in the HF- (left) and HF+ (right) calorimeters. Green vertical lines represent thresholds keeping 99% of the events in the spectrum.

Figures 51 and 52 present normalised distributions of single muon p_{T} and dimuon acoplanarity for all three MC samples and the data after all the described selections. Acoplanarity, A is defined by the following formula:

$$A = \frac{|\pi - |\Delta\phi||}{\pi}. \quad (15)$$

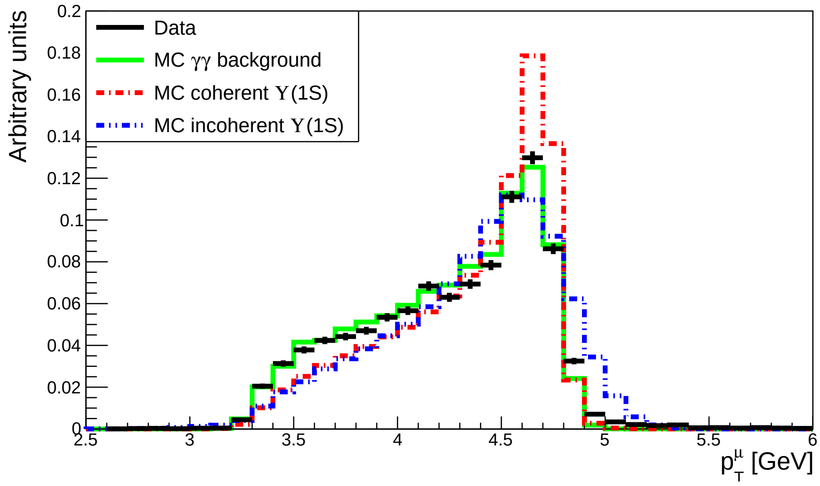

Figure 51: Normalised distributions of single muon transverse momenta for the data (black crosses) and all three MC samples: the $\gamma\gamma$ events in the invariant mass signal region, 9.2 to 9.7 GeV (green line), coherent Υ photoproduction (red line) and incoherent Υ photoproduction (blue line). Most of the muons have p_{T} around half of the Υ(1S) mass, because the system is produced at rest.

The coherent Υ and $\gamma\gamma$ background events have very low acoplanarity, $A < 0.02$, the incoherent Υ sample has a broader distribution with the acoplanarity $A < 0.1$ and in the data there is small fraction of events with $A > 0.1$. Fig. 53 show the dependence of the dimuon p_{T} on the acoplanarity in the data. Based on the distributions shown if Figures 51 and 52 two additional requirements are added in order to suppress background: only events with acoplanarity below 0.075 are selected and the single muon p_{T} is required to be above 3.0 GeV for both muons. Table 5 presents number of events in the data after applying all the selection criteria for the dimuon invariant mass region of the signal, 9.2 GeV $< M <$ 9.7 GeV.

Resulting kinematic distributions of the single muons and reconstructed dimuons obtained for the data after applying all the selection criteria for the events with the invariant mass in the signal range, 9.2 GeV $< M <$ 9.7 GeV are presented in Fig. 54. Figures 55, 56 and 57 show the invariant mass distributions for the data, $\gamma\gamma$ MC sample, coherent Υ(1S) MC sample and incoherent Υ(1S) MC sample accordingly. A Υ(1S) peak can be seen

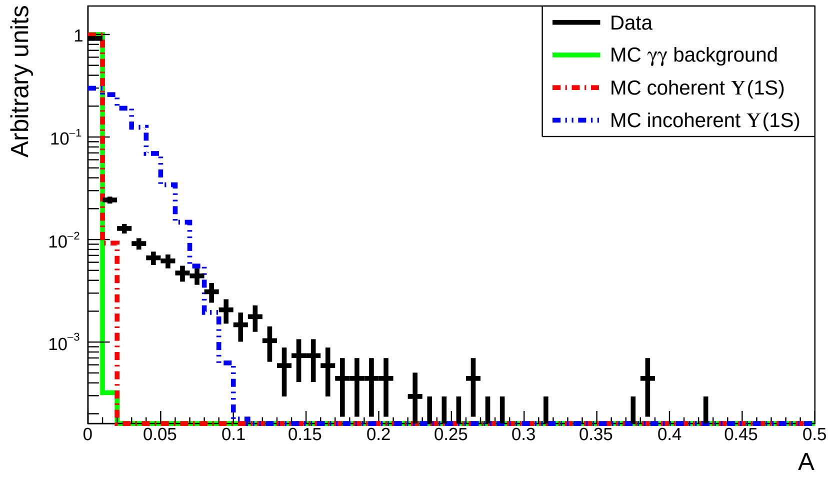

Figure 52: Normalised distributions of the acoplanarity for the data (black crosses) and all three MC samples: the $\gamma\gamma$ events with the invariant between 9.2 to 9.7 GeV (green line), coherent Υ photoproduction (red line) and incoherent Υ photoproduction (blue line).

around 9.46 GeV, the rest of the distribution is mostly due to the $\gamma\gamma$ events. Figures 58 and 59 show the normalised distributions for the dimuon rapidity, y and transverse momenta, $p_{\mathrm{T}}^{\mu\mu}$ for the data and all three MC samples. The rapidity distributions have very similar shapes while the $p_{\mathrm{T}}^{\mu\mu}$ distributions are similar for the $\gamma\gamma$ and coherent $\Upsilon(1S)$ MC samples and much broader for the incoherent $\Upsilon(1S)$ sample, which coveres a region of 0 GeV $< p_{\mathrm{T}}^{\mu\mu} <$ 1.1 GeV. The $\Upsilon(1S)$ MC samples have been obtained without any kinematic requirements on the produced particles and, on the generation level, they correspond to the total cross-section for these processes. Therefore the efficiency for the process to be included in the signal sample can be obtained as the number of events passing all the selection criteria applied for the data to the overal number of produced particles. For the coherent $\Upsilon(1S)$ MC sample this efficiency is $E_{\mathrm{MC}} = 145224/500000 = 0.290448$

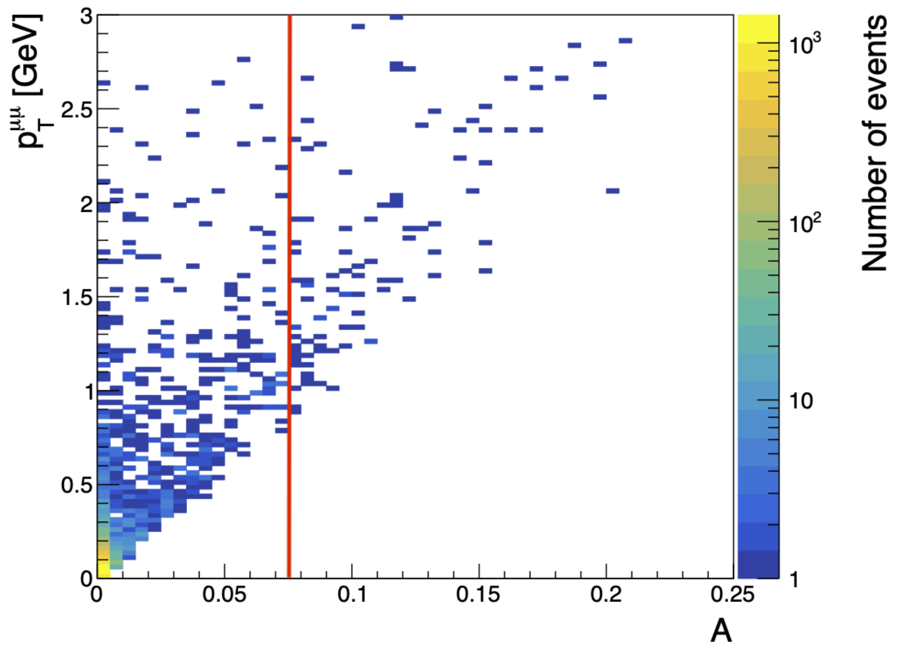

Figure 53: The dependence of the dimuon transverse momenta, $p_{\mathrm{T}}^{\mu\mu}$ on the acoplanarity, A in the data.

Table 5: Table presents the number of data events for the dimuon invariant mass region of the signal, 9.2 GeV $< M <$ 9.7 GeV after fullfiling consecutive requirements described in the text.

requirement	number of events
9.2 GeV $< M <$ 9.7 GeV, trigger, 1 reconstructed dimuon	11699
acceptance selection (Tab. 4)	10835
Soft ID	10645
2 tracks of opposite sign	9241
HF requirement	6784
muon $p_{\mathrm{T}} > 3.0$ GeV	6760
acoplanarity requirement	6644

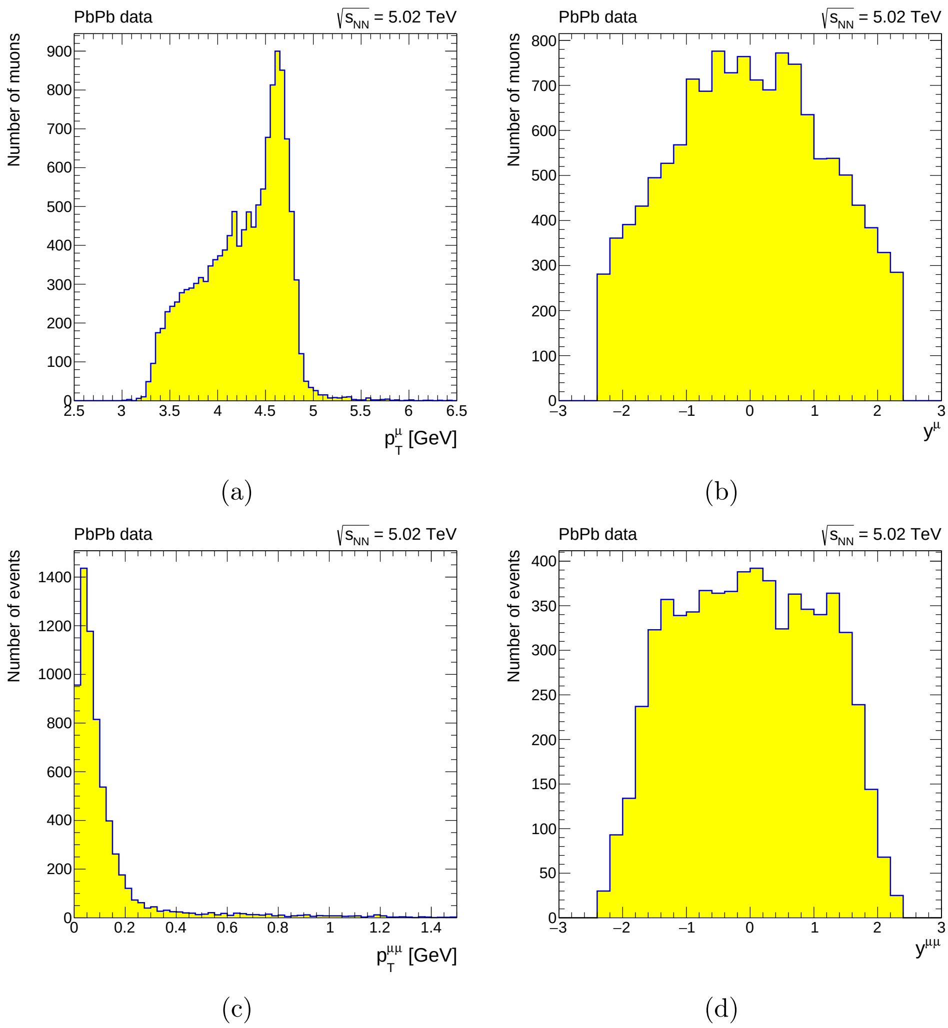

Figure 54: Distributions of data events with the invariant mass in the 9.2 GeV $< M <$ 9.7 GeV range obtained after applying all the selection criteria. Panel (a) presents the single muon transverse momenta, panel (b) – single muon rapidity, panel (c) – dimuon transverse momenta and panel (d) – dimuon rapidity distribution.

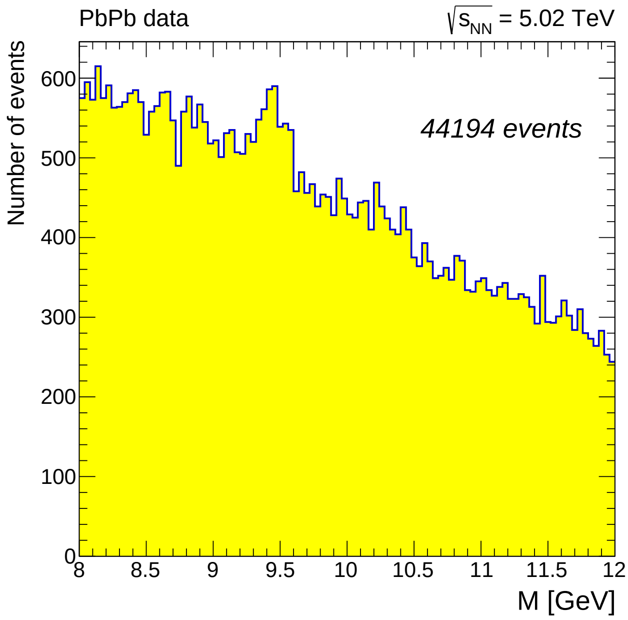

Figure 55: Distribution of the dimuon invariant mass in the data. A peak at a $\Upsilon(1S)$ mass can be observed and there is no clear contribution from higher states. A linear contribution across whole mass range is mostly due to the $\gamma\gamma$ events.

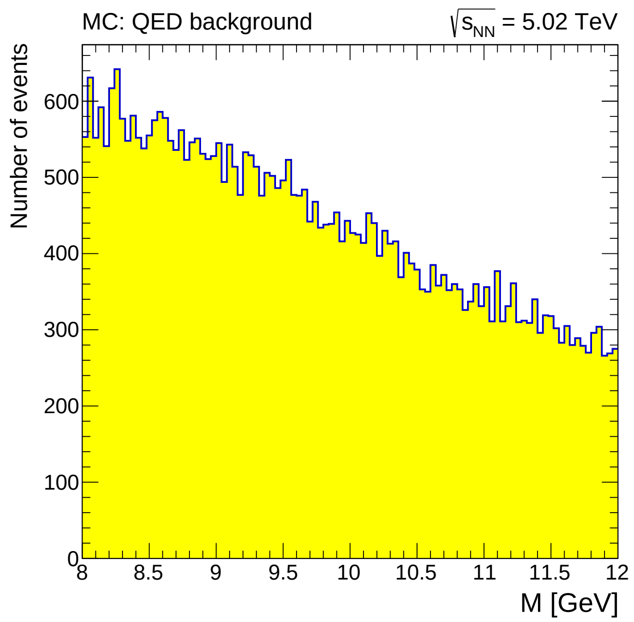

Figure 56: Distribution of the dimuon invariant mass in the STARLIGHT MC $\gamma\gamma$ sample.

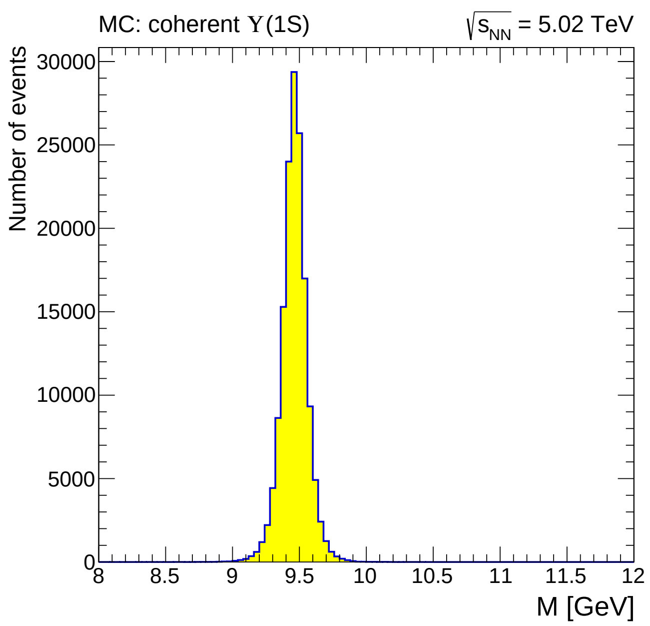

Figure 57: Distribution of the dimuon invariant mass in the STARLIGHT MC coherent Υ(1S) sample.

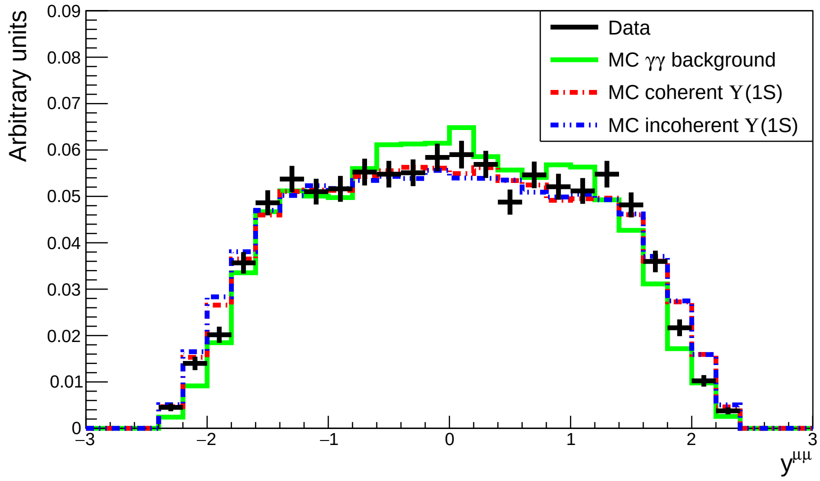

Figure 58: Normalised distributions of dimuon transverse momenta for the data (black crosses) and all three MC samples: the $\gamma\gamma$ events in the invariant mass signal region, 9.2 to 9.7 GeV (green line), coherent $\Upsilon(1S)$ photoproduction (red line) and incoherent $\Upsilon(1S)$ photoproduction (blue line).

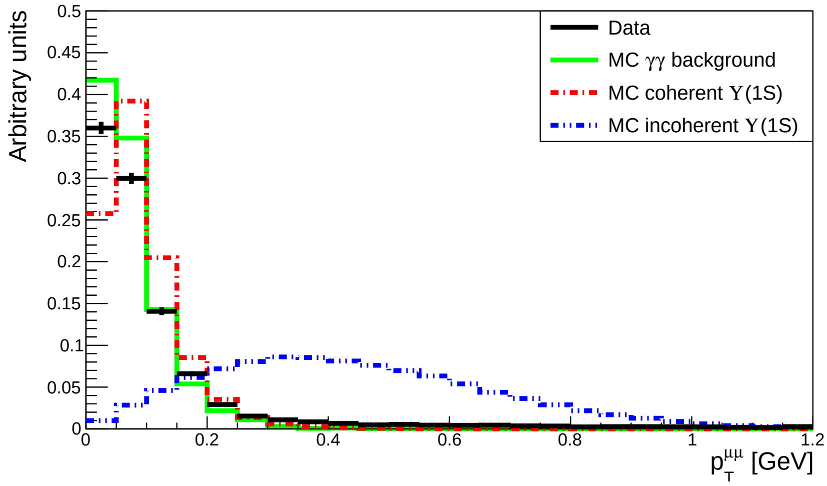

Figure 59: Normalised distributions of dimuon transverse (in GeV units) momenta for the data (black crosses) and all three MC samples: the $\gamma\gamma$ events in the invariant mass signal region, 9.2 to 9.7 GeV (green line), coherent $\Upsilon(1S)$ photoproduction (red line) and incoherent $\Upsilon(1S)$ photoproduction (blue line).

4.5 Signal Extraction

4.5.1 Invariant mass distribution

Figure 60 presents the invariant mass distribution spectrum of $\mu\mu$ pairs in the range 8 - 12 GeV satisfying the analysis selection criteria (see Table 5) except the mass window requirement. The unbinned fits to the mass spectrum have been performed with the RooFit package [58] with a linear function describing the $\gamma\gamma$ QED background and Gaussian functions for the Υ peaks. The free parameers of the fit presented in panel (a) are the Υ(1S) mass and width, the number of the QED background events and the slope parameter of the linear background function. The masses (widths) of Υ(2S) and Υ(3S) states are obtained by multiplying the fitted Υ(1S) mass (width) by the ratio of the masses of given state to the Υ(1S) mass taken from the Particle Data Group. The obtained number of the UPC Υ(1S) events (coherent and incoherent) is 630 ± 97. The estimation of the number of Υ(2S) and Υ(3S) events is compatible with 0, therefore only the Υ(1S) production process is considered in the analysis. In panel (b) for comparison a fit has been performed for background and Υ(1S) peak only. This result will be used for systematic uncertainty studies.

4.5.2 Separation of Υ(1S) production modes

In order to distinguish between background, coherent and incoherent Υ(1S) photoproduction the method based on the dimuon transverse moment spectrum is used. First a data-based sideband invariant mass region subtraction approach is used to obtain the $p_{\mathrm{T}}^{\mu\mu}$ of the coherent and incoherent Υ(1S) spectrum and then they are separated based on the distributions obtained from MC samples. The assumption is that the $p_{\mathrm{T}}^{\mu\mu}$ spectrum in a given invariant mass range can be approximated by an average of the spectra from the invariant mass bands below and above weighted by the number of events in each region. In order to check this assumption the test has been performed with three mass regions: 8.0 - 8.3 GeV, 8.3 - 8.7 GeV and 8.7 - 9.0 GeV. The results are presented in Fig. 61. Panel (b) presents the distribution obtained after subtracting the spectra from the sideband regions weighted by the number of the events in each region. The resulting distribution is flat and does not show a dependence on $p_{\mathrm{T}}^{\mu\mu}$ within the uncertainties, which is

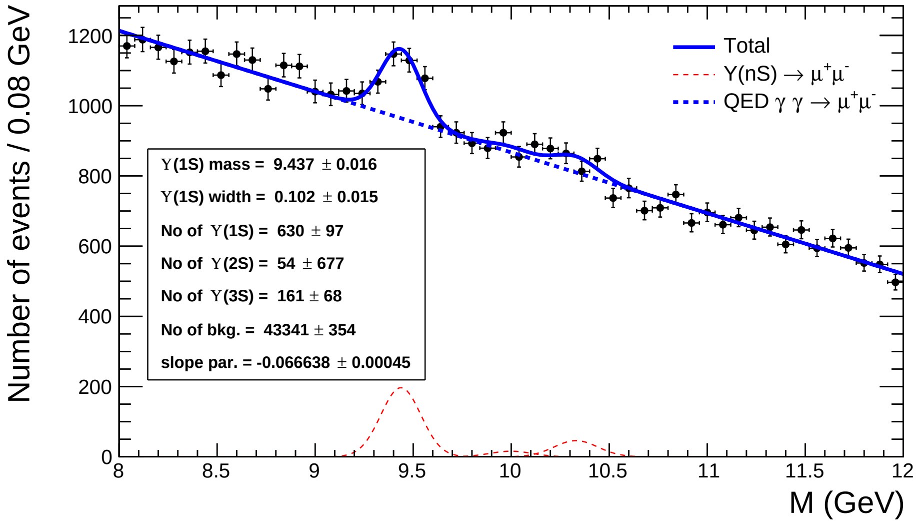

(a)

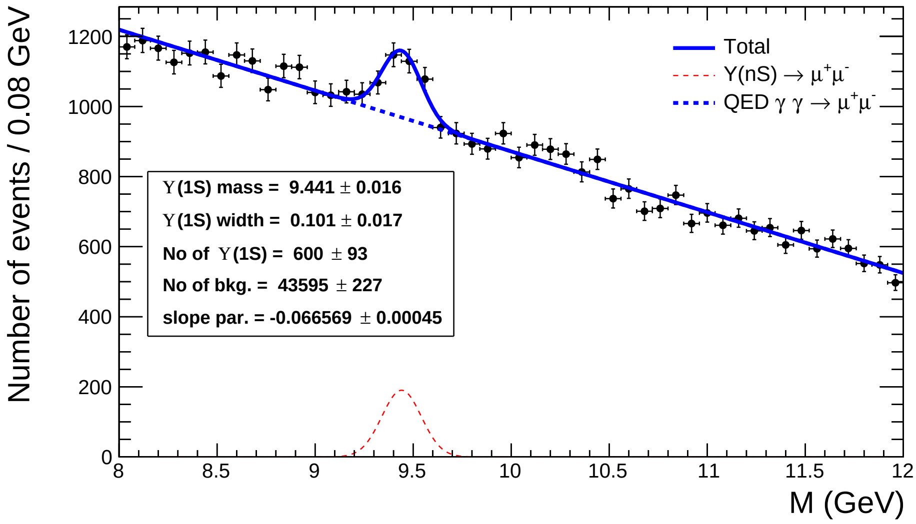

(b)

Figure 60: Invariant mass distribution spectrum of the $\mu\mu$ pairs satisfying the described selection criteria. Details of the fitting procedure are described in the text. In panel (a) the resulting yields for all Υ states and background, mass and width of $\Upsilon(1S)$ and the slope parameter of the background function are shown. The obtained number of the $\Upsilon(1S)$ events (coherent and incoherent) is 630 ± 97. In panel (b) only $\Upsilon(1S)$ peak has been fitted for comparison.

consistent with the assumption, that the shape of the weighted average of the sideband region distributions can be approximated by the distribution from the middle invariant mass region. Fig. 62 presents a similar test where the Υ(1S) mass region (9.2 - 9.7 GeV) has been used as the signal, and the two sideband regions are 8.0 - 9.0 GeV and 10.6 - 11.6 GeV – the second region is selected so that it is outside of possible contribution from the Υ(2S) and Υ(3S) states events. The obtained distribution shown in panel (b) is not flat in this case, what indicates additional contribution in the signal region. Although the error bars are significant, it can be seen, that there are less events for $p_{\mathrm{T}}^{\mu\mu} < 0.2$ GeV and excess for $p_{\mathrm{T}}^{\mu\mu} > 0.5$ GeV, which is expected if in the signal region there is a contribution from the incoherent Υ(1S) events.

The obtained averaged sideband distribution is normalised to the number of events in the signal region reduced by 630 and then subtracted from the signal sample. This results in a coherent and incoherent Υ signal $p_{\mathrm{T}}^{\mu\mu}$ spectrum normalised to 630 events. The dimuons from coherent Υ sample have very low p_{T}, most of them are below 0.1 GeV. The incoherent Υ sample has a noticeably different distribution with only small fraction of events overlapping with the dimuon p_{T} range of the coherent Υ sample. This difference in the shape of the $p_{\mathrm{T}}^{\mu\mu}$ spectra is used to distinguish between these two processes. The normalised coherent (red) and incoherent (blue) Υ(1S) $p_{\mathrm{T}}^{\mu\mu}$ distributions obtained with STARLIGHT are fitted to the spectrum obtained form the data and the contributions from both processes are evaluated. The $p_{\mathrm{T}}^{\mu\mu}$ distributions obtained with the sideband region subtraction method are presented in Fig. 63. In panel (a) the sideband regions are 8.0 - 9.0 GeV and 10.6 - 11.6 GeV. In panel (b) the right-hand sideband region is 9.9 - 10.9 GeV. The methods give consistent results: 432 $\pm$ 21 coherent Υ(1S) UPC events in panel (a) (nominal model) and 441 $\pm$ 23 coherent Υ(1S) events in panel (b) (cross-check model). The difference in the obtained yields contribute to the systematic uncertainty. Based on the obtained result the number of coherent UPC Υ(1S) events is

$$N_{\Upsilon(1\mathrm{S}),\mathrm{coh}} = 432 \pm 70,$$

where the statistical uncertainty includes the contribution from the yield from the invariant mass fit (630 $\pm$ 97 events).

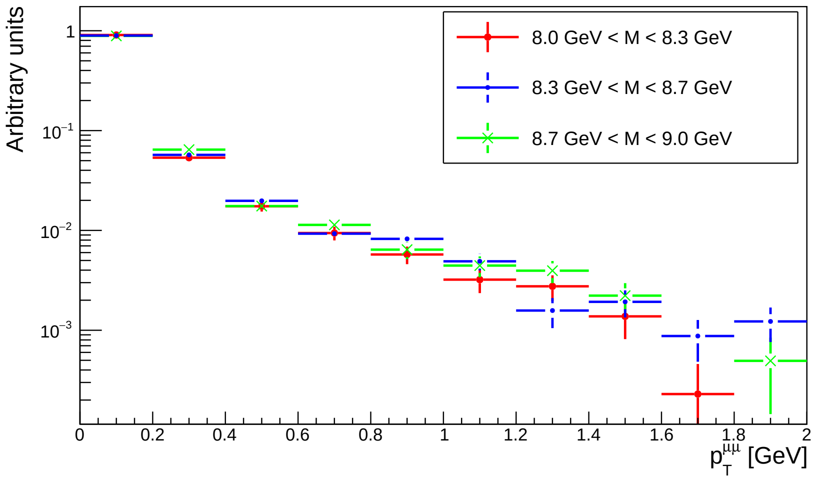

(a)

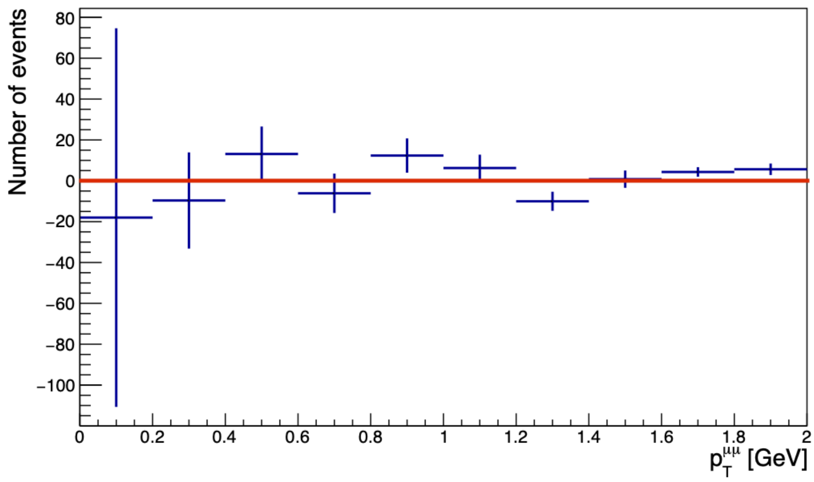

(b)

Figure 61: The test of the sideband subtraction of the transverse distributions approach. The test has been performed with three mass regions: 8.0 - 8.3 GeV (red), 8.3 - 8.7 GeV (blue) and 8.7 - 9.0 GeV (green). Panel (a) shows three $p_{\mathrm{T}}^{\mu\mu}$ distributions normalised to 1 unit. Panel (b) presents the distribution obtained after subtracting the spectra from the sideband regions weighted by the number of the events in each region. The red line presents empty bins for reference.

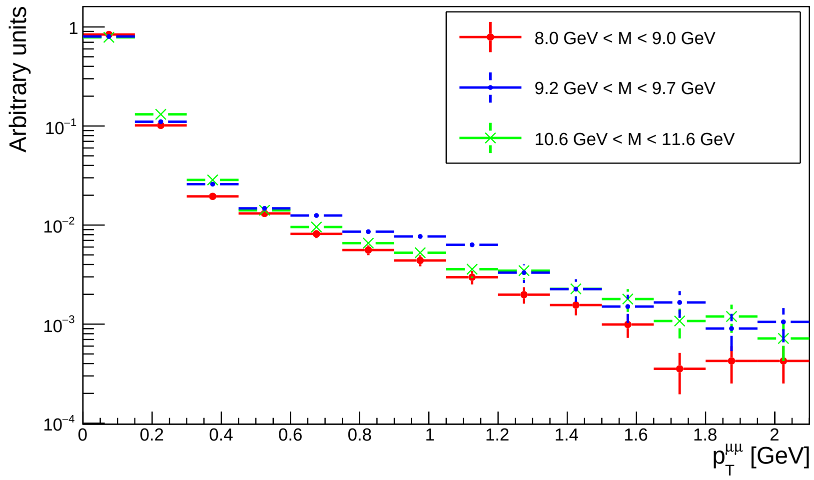

(a)

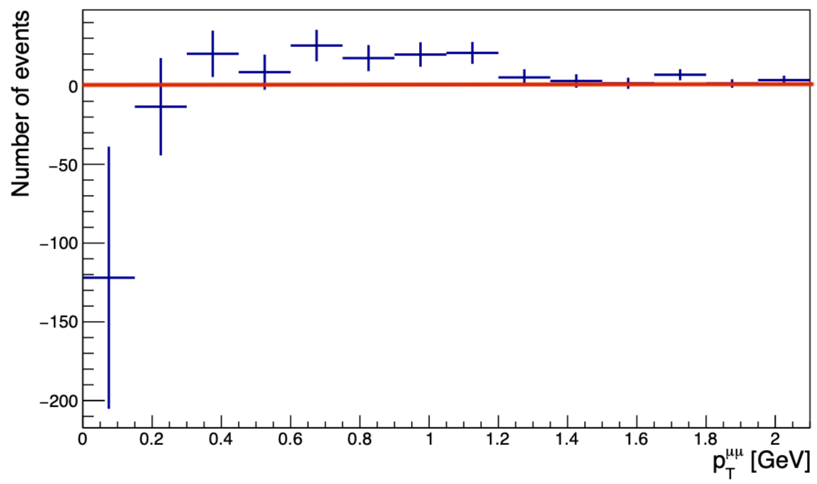

(b)

Figure 62: The test of the sideband subtraction of the $p_T^{\mu\mu}$ distributions approach. The test has been performed with three mass regions: 8.0 - 9.0 GeV (red), 9.2 - 9.7 GeV (blue) and 10.6 - 11.6 GeV (green). Panel (a) shows three $p_T^{\mu\mu}$ distributions normalised to 1 unit. Panel (b) presents the distribution obtained after subtracting the spectra from the sideband regions weighted by the number of the events in each region. The red line presents empty bins for reference.

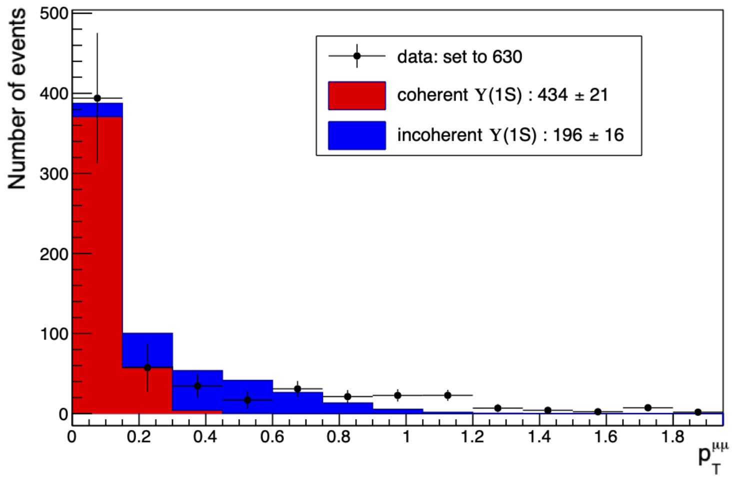

(a)

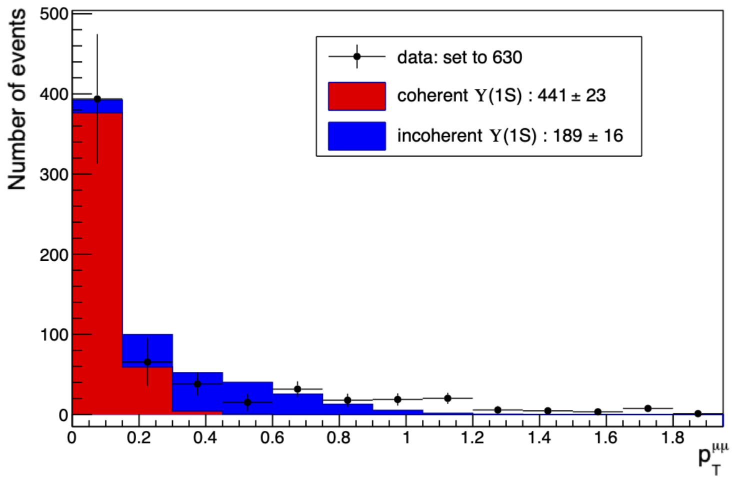

(b)

Figure 63: The $p_{\mathrm{T}}^{\mu\mu}$ distributions obtained with the sideband region subtraction method. The averaged distribution is subtracted from the one obtained in the signal region (9.2 - 9.7 GeV) so that 630 events are left in the $p_{\mathrm{T}}^{\mu\mu}$ spectrum. The distributions obtained from STARLIGHT coherent (red) and incoherent (blue) Υ(1S) MC samples are fitted and the contributions from both processes are obtained. In panel (a) the sideband regions are 8.0 - 9.0 GeV and 10.6 - 11.6 GeV. In panel (b) the right-hand sideband region is 9.9 - 10.9 GeV. Both methods give similar results: 432 $\pm$ 21 coherent Υ(1S) events in panel (a) and 441 $\pm$ 23 coherent Υ(1S) events in panel (b).

4.6 Muon selection efficiency

A critical element of the cross-section measurement is a accurate understanding of the efficiency for selection of used objects. The results obtained from the MC simulation are not fully reliable due to imperfections in the modeling of the detector response. For this reason the data-driven method called "Tag and Probe" is used to evaluate correction factors, which are defined as the ratio of the efficiency obtained with data to the one obtained in MC in a given kinematic range. The Tag and Probe approach measures objects efficiency with use of the resonance such as Z or J/ψ decaying to the two given objects. First the resonance is reconstructed as a pairs of "tags" and "probes". A tag must match tight selection criteria while a probe is defined according to the measured efficiency. Then two categories of events; tags + passing probes (matching the criteria) and tags + failing probes (not matching the criteria) are separately fitted to the resonance signal + background model. The obtained yields for the resonance signal are then finally used to obtain the efficiency for a given selection, which is evaluated as the ratio of the obtained signal yields. The method is used separately for the real data sample and MC simulation and the results are produced in kinematic bins of η and p_{T}. The presented Tag and Probe study covers wide muon kinematic range and can be used by other UPC analyses in CMS that will use 2018 PbPb data, e.g. UPC J/ψ photoproduction or luminosity calibration with UPC QED processes.

4.6.1 Overview and settings

For data, the same dataset is used as the one used for the analysis. The MC sample has been generated using the PYTHIA 8 generator [59]. For this study the J/ψ peak is used and the sample contains head-on hadronic interactions – the measured efficiencies do not depend on the selected resonance or the type of the interaction, but on the kinematics of the muons. Furthermore the J/ψ meson is produced much more abundantly during the collisions than ϒ meson. Muon pairs in the invariant mass range $2.6 < M < 3.5$ GeV are used for this study. The signal function used is a double Crystal Ball where

Table 6: Overview of the settings used to obtain the TnP efficiencies.

Efficiency type	Muon ID	Trigger selection
Probe	track	Soft ID
Passing Probe	Soft ID	Trigger Match
kinematic range	p_{T} in $\lvert\eta\rvert$ bins	p_{T} in $\lvert\eta\rvert$ bins
signal function	Double Crystal Ball	Double Crystal Ball
bkg function	1st order polynomial	1st order polynomial
mass range (GeV)	(2.6, 3.5)	(2.6, 3.5)

both functions have common α, mean and n parameters[3]. The background is fitted with the first order polynomial.

The single muon efficiency is evaluated in two steps, because both muons are required to fulfil the Soft ID, but only one have to be matched to the trigger. The settings are described in the Table 6. The tag is required be within the a acceptance selection[4], pass the Soft ID requirement and

[3] The Crystal Ball probability density function consists of a Gaussian core and a power-law tail and is given by:

$$f(x;\alpha,n,\bar{x},\sigma) = N \cdot \begin{cases} \exp(-\frac{(x-\bar{x})^2}{2\sigma^2}), & \text{for } \frac{x-\bar{x}}{\sigma} > -\alpha \\ A \cdot (B - \frac{x-\bar{x}}{\sigma})^{-n}, & \text{for } \frac{x-\bar{x}}{\sigma} \leqslant -\alpha \end{cases}$$

where

$$\begin{aligned} A &= \left(\frac{n}{|\alpha|}\right)^n \cdot \exp\left(-\frac{|\alpha|^2}{2}\right), \\ B &= \frac{n}{|\alpha|} - |\alpha|, \\ N &= \frac{1}{\sigma(C+D)}, \\ C &= \frac{n}{|\alpha|} \cdot \frac{1}{n-1} \cdot \exp\left(-\frac{|\alpha|^2}{2}\right), \\ D &= \sqrt{\frac{\pi}{2}}\left(1 + \mathrm{erf}\left(\frac{|\alpha|}{\sqrt{2}}\right)\right). \end{aligned}$$

N is a normalization factor and erf is the error function.

[4] The same acceptance region as described in 4.3 is used.

fullfil the trigger[5] requirements. In order to ensure agreement with the low occupancy of the detector for the UPC, events with centrality below 180 are rejected in both data and MC. The centrality in CMS is measured with the number of the detected particles and takes values from 0 to 200, therefore centrality above 180 means 10% of the most peripheral events.

The results are presented in the following muon p_T bins (in GeV): (1.4, 1.9), (1.9, 2.4), (2.4, 2.9), (2.9, 3.4), (3.4, 4.0), (4.0, 5.0), (5.0, 6.0) and (6.0, 10.0), and in three $|\eta|$ ranges: $0 < \eta < 0.8$, $0.8 < \eta < 1.6$ and $1.6 < \eta < 2.4$.

4.6.2 Efficiency of Soft Muon Identification

In the first step the efficiency of a track to match the Soft muon ID criteria is evaluated. The track reconstruction efficiency is assumed to be 100 % in the considered kinematic range. In Fig. 64 the example fits for all, passing and failing probes used for efficiency evaluation for both data and Monte Carlo are presented. The obtained single muon efficiencies for a track to be reconstructed as a muon matching Soft muon ID in muon p_T bins for three $|\eta|$ ranges are shown in Fig. 65.

[5]The same trigger is used for the efficiency studies as the one used in the analysis.

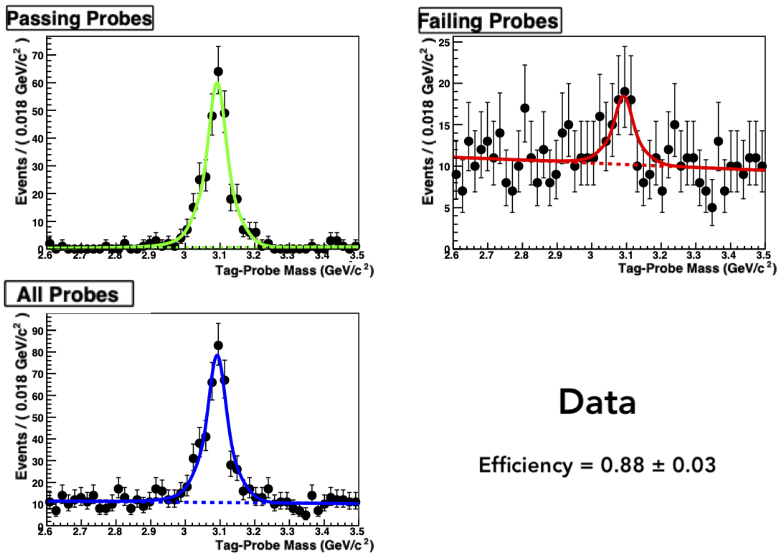

(a)

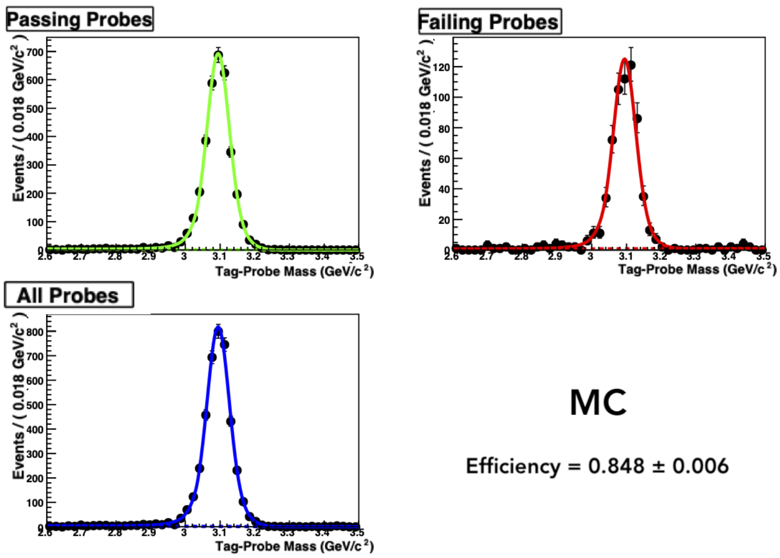

(b)

Figure 64: Example fits for data (panel (a)) and Monte Carlo (panel (b)) for $0.8 < \eta < 1.6$ and 2.9 GeV $< p_{\mathrm{T}} <$ 3.4 GeV bin are presented. Three cases are presented: passing probes, failing probes and all probes.

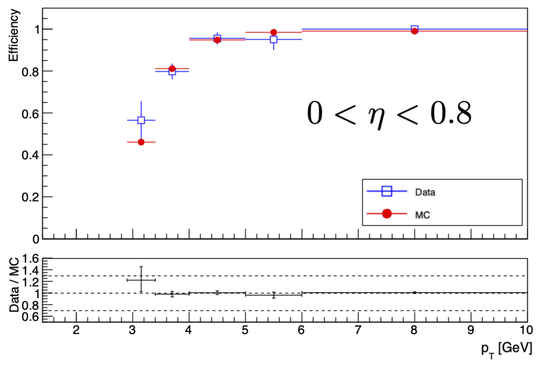

(a)

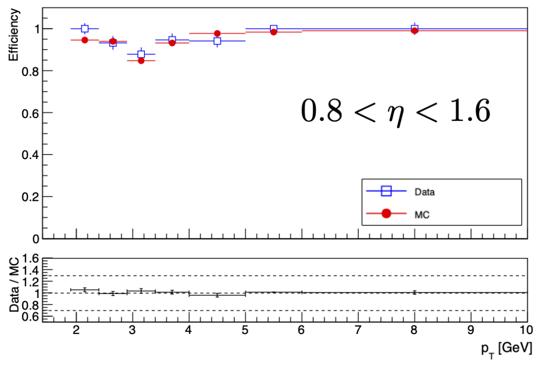

(b)

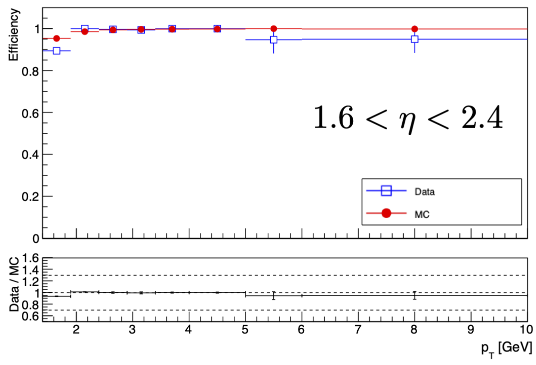

(c)

Figure 65: Single muon efficiencies for a track to to match the Soft muon ID criteria are presented in muon p_{T} bins for the three $|\eta|$ ranges: $0 < \eta < 0.8$ (panel (a)), $0.8 < \eta < 1.6$ (panel (b)) and $1.6 < \eta < 2.4$ (panel (c)).

4.6.3 Triggering efficiency

In the second step the efficiency of a muon fulfilling Soft ID requirements to match the trigger is obtained. In Fig. 66 the example fits for all, passing and failing probes used for efficiency evaluation for both data and Monte Carlo are presented. The obtained single muon efficiencies for the muon matching Soft ID to match the trigger as functions of muon p_{T} for three $|\eta|$ ranges are shown in Fig. 67.

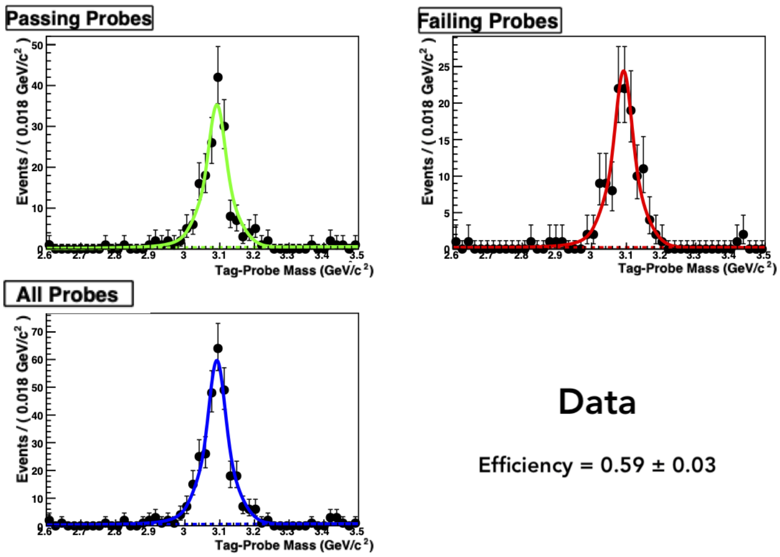

(a)

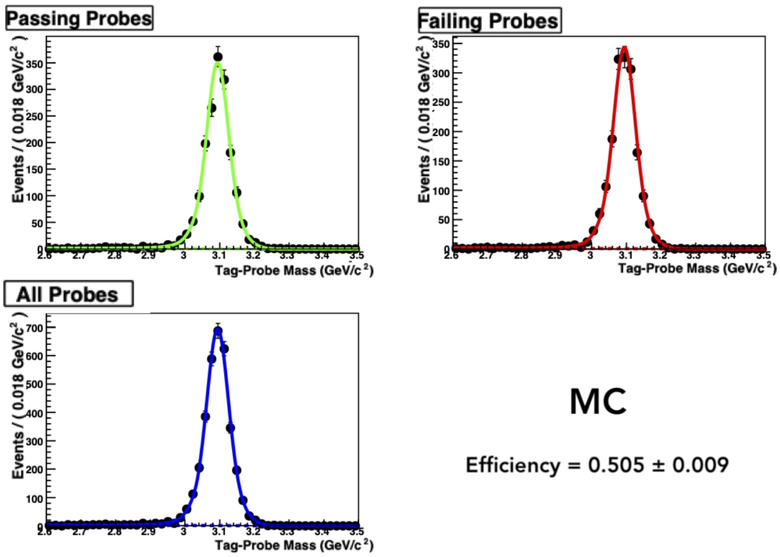

(b)

Figure 66: Example fits for data (panel (a)) and Monte Carlo (panel (b)) for $0.8 < \eta < 1.6$ and 2.9 GeV $< p_{\mathrm{T}} <$ 3.4 GeV bin are presented. Three cases are presented: passing probes, failing probes and all probes.

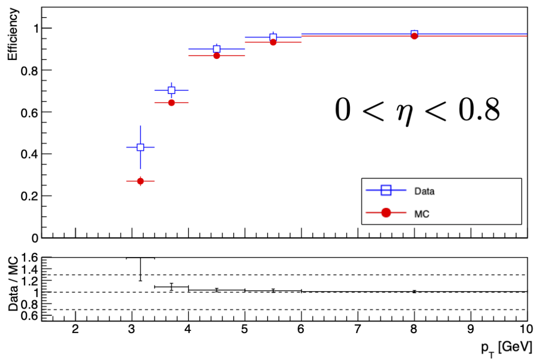

(a)

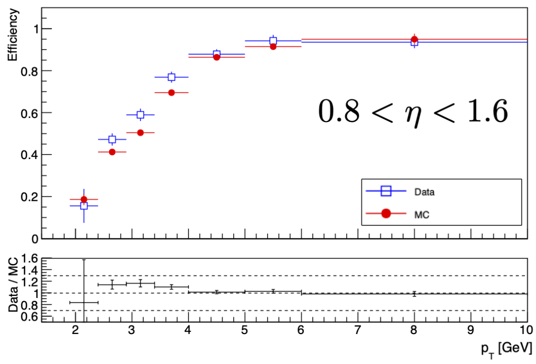

(b)

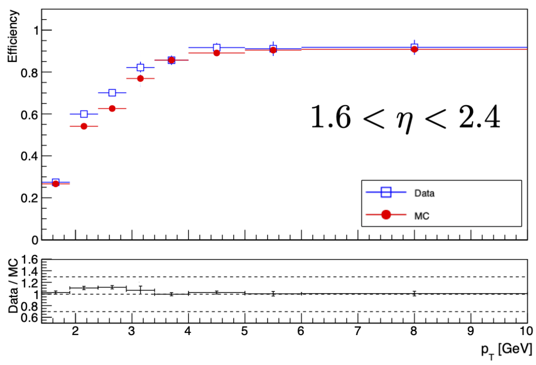

(c)

Figure 67: Single muon efficiencies for a muon satisfying Soft muon ID to match the trigger requirements are presented in muon p_{T} bins for the three $|\eta|$ ranges: $0 < \eta < 0.8$ (panel (a)), $0.8 < \eta < 1.6$ (panel (b)) and $1.6 < \eta < 2.4$ (panel (c)).

4.7 Scale Factors

Because the simulation does not reproduce data exactly there is a need to compensate for the differences originating from these discrepancies and therefore correct the MC modeling. The scale factors (SF) are used to compare the efficiency of a given selection obtained from the data and the MC sample. They are defined with use of the Tag and Probe efficiencies as

$$SF = \frac{\epsilon_{data}}{\epsilon_{MC}}. \tag{16}$$

The scale factors with statistical uncertainties for given p_{T} and $|\eta|$ ranges obtained with the efficiencies presented in this analysis are shown in Tables 7 and 8.

Table 7: Scale factors with statistical uncertainties obtained with the Tag and Probe method for the soft muon ID efficiencies.

	$0 < \|\eta\| < 0.8$	$0.8 < \|\eta\| < 1.6$	$1.6 < \|\eta\| < 2.4$
$1.4 < p_{\mathrm{T}} < 1.9$	–	–	0.9381 ± 0.0051
$1.9 < p_{\mathrm{T}} < 2.4$	–	1.057 ± 0.033	1.0144 ± 0.0046
$2.4 < p_{\mathrm{T}} < 2.9$	–	0.992 ± 0.035	1.002 ± 0.013
$2.9 < p_{\mathrm{T}} < 3.4$	1.22 ± 0.21	1.036 ± 0.040	0.997 ± 0.017
$3.4 < p_{\mathrm{T}} < 4.0$	0.983 ± 0.047	1.015 ± 0.033	1.0024 ± 0.0097
$4.0 < p_{\mathrm{T}} < 5.0$	1.007 ± 0.031	0.963 ± 0.031	1.0018 ± 0.0098
$5.0 < p_{\mathrm{T}} < 6.0$	0.965 ± 0.052	1.0162 ± 0.0024	0.947 ± 0.067
$6.0 < p_{\mathrm{T}} < 10.0$	1.009 ± 0.014	1.009 ± 0.030	0.951 ± 0.067

Table 8: Scale factors with statistical uncertainties obtained with the Tag and Probe method for the triggering efficiencies.

	$0 < \|\eta\| < 0.8$	$0.8 < \|\eta\| < 1.6$	$1.6 < \|\eta\| < 2.4$
$1.4 < p_{\mathrm{T}} < 1.9$	–	–	1.028 ± 0.027
$1.9 < p_{\mathrm{T}} < 2.4$	–	0.83 ± 0.60	1.107 ± 0.029
$2.4 < p_{\mathrm{T}} < 2.9$	–	1.144 ± 0.077	1.119 ± 0.028
$2.9 < p_{\mathrm{T}} < 3.4$	1.59 ± 0.46	1.168 ± 0.063	1.067 ± 0.036
$3.4 < p_{\mathrm{T}} < 4.0$	1.091 ± 0.061	1.105 ± 0.039	0.999 ± 0.027
$4.0 < p_{\mathrm{T}} < 5.0$	1.036 ± 0.030	1.016 ± 0.028	1.028 ± 0.025
$5.0 < p_{\mathrm{T}} < 6.0$	1.025 ± 0.029	1.030 ± 0.031	1.007 ± 0.039
$6.0 < p_{\mathrm{T}} < 10.0$	1.010 ± 0.020	0.985 ± 0.041	1.010 ± 0.040

Since both muons are required to pass the muon ID selection, and either one or both muons can fulfil the trigger requirement there are two scenarios. If one muon (μ_1) passes the trigger requirements and the other does not the correction from the Tag and Probe for that event, C is equal to:

$$C = SF^{\mathrm{ID}}(\mu_1) \times SF^{\mathrm{TRG}}(\mu_1) \times SF^{\mathrm{ID}}(\mu_2). \tag{17}$$

If both muons pass the trigger selection the correction is evaluated as the average, i.e.

$$C = \frac{SF^{\mathrm{ID}}(\mu_1) \times SF^{\mathrm{TRG}}(\mu_1) \times SF^{\mathrm{ID}}(\mu_2)}{2} + \frac{SF^{\mathrm{ID}}(\mu_2) \times SF^{\mathrm{TRG}}(\mu_2) \times SF^{\mathrm{ID}}(\mu_1)}{2}. \tag{18}$$

The scale factors have been applied event by event for the signal data sample with a consideration of each muon's p_{T} and η. The correction obtained from the Tag and Probe method is equal to

$$C_{\mathrm{T\&P}} = 1.0349 \pm 0.0010.$$

4.8 Systematic Uncertainties

In the measurement of the cross-section the following sources of the systematic uncertainty are taken into account:

- the exclusivity selection uncertainty is studied by varying the HF energy deposition requirement by 0.5 GeV. This procedure leads to a 0.6 % uncertainty.
- the influence of the model of the invariant mass fit including the effect the Υ(2S) and Υ(3S) states have on the number of signal events have are studied by comparing the number of obtained signal events with the nominal parameters to the model where Υ(2S) and Υ(3S) states are treated as background (Fig. 60, panel (b)). The contribution from this source is estimated to be 4.8 %.
- the impact on the uncertainty of the separation of Υ(1S) production modes with p_{T} spectrum is estimated by considering different sideband regions used for the signal extraction. With the model, where the right-hand sideband region set to 9.9 - 10.9 GeV (Fig. 63, panel (b)) the obtained contribution from this source to the systematic uncertainty is 1.6 %.
- the uncertainty of the value of the integrated luminosity of the 2018 PbPb data sample obtained by the CMS experiment is 1.9 %. This value has been evaluated by dedicated group in CMS and available on an internal web page[60].
- the uncertainty in the photon flux calculation used in the MC modeling also affects the cross-section. It has been estimated by varying the Pb radius by ± 0.5 fm in the STARLIGHT code and studying its impact on the cross-section in the QED sample with the energy range of the Υ(1S) state. The influence of this studies amounts to 4.0 %.
- the branching ratio of the muon decay of the Υ(1S) meson, $BR_{\Upsilon(1S)\to\mu^+\mu^-}$ = 2.48 ± 0.05 has been taken from the Particle Data Group[5]. Its impact on the systematic uncertainty of the cross-section measurement is 2.0 %.

- the systematic uncertainty associated with the Tag and Probe correction $C_{\mathrm{T\&P}}$ is estimated from the average value of the efficiency difference between data and MC divided by the efficiency for the MC, denoted as $\Delta_{\mathrm{T\&P}}$ and evaluated for all the muons from the data events passing all selection criteria. The total uncertainty is calculated as

$$\mathrm{T\&P}_{\mathrm{syst.uncert.}} = \sqrt{(2\Delta_{\mathrm{T\&P,ID}})^2 + (\Delta_{\mathrm{T\&P,TRG}})^2}, \tag{19}$$

  where $\Delta_{\mathrm{T\&P,ID}}$ represents the contribution from the efficiencies obtained for the soft muon ID selection and $\Delta_{\mathrm{T\&P,TRG}}$ for the trigger requirement. Factor of 2 is due two muons passing the ID requirements. This method of evaluating Tag and Probe correction has been used is following previous UPC analysis in CMS[47]. This contribution led to a 6.0 % uncertainty.

Table 9 summarises all contributions to the total systematic uncertainty which has been evaluated as the quadratic sum of the uncertainties from all 7 sources and is equal to:

$$\Delta_{\mathrm{syst.}} = 9.3\%.$$

Table 9: Overview of the contributions to the systematic uncertainty.

exclusivity selection	0.6 %
invariant mass fit model	4.8 %
separation of Υ(1S) production modes	1.6 %
integrated luminosity	1.9 %
photon flux	4.0 %
branching ratio	2.0 %
Tag and Probe	6.0 %
total	**9.3 %**

5 Results

5.1 Cross-section

The total cross-section for the coherent UPC photoproduction of the $\Upsilon(1S)$ in PbPb collisions at the $\sqrt{s_{NN}} = 5.02$ TeV is given by:

$$\sigma_{\mathrm{PbPb}\to\Upsilon(1S),\mathrm{coh}} = \frac{N_{\Upsilon(1S),\mathrm{coh}} \times C_{\mathrm{T\&P}}}{L_{\mathrm{int}} \times E_{\mathrm{MC}} \times BR_{\Upsilon(1S)\to\mu^+\mu^-}}, \tag{20}$$

where, $N_{\Upsilon(1S),\mathrm{coh}} = 432 \pm 70$, $C_{\mathrm{T\&P}} = 1.0349 \pm 0.0010$, $L_{\mathrm{int}} = 1621.6\ \mu\mathrm{b}^{-1}$, $E_{\mathrm{MC}} = 0.29$, and $BR_{\Upsilon(1S)\to\mu^+\mu^-} = 2.48$. The value obtained in this analysis is

$$\sigma_{\mathrm{PbPb}\to\Upsilon(1S),\mathrm{coh}} = 38.4 \pm 6.2\ (\mathrm{stat}) \pm 3.6\ (\mathrm{syst})\ \mu\mathrm{b}.$$

5.2 Comparison to theoretical predictions

Table 10 presents cross-sections for the photoproduction of the $\Upsilon(1S)$ in PbPb collisions at the $\sqrt{s_{NN}} = 5.02$ TeV obtained with different parametrizations of the gluon distribution and gluon shadowing for nuclear PDFs [61]. The values have been presented for the CMS rapidity range $|\eta| < 2.4$. In order to compare them to the result obtained in the presented analysis the correction factor evaluated from generator level STARLIGHT coherent $\Upsilon(1S)$ sample have been applied to normalise them to the total cross-section (blue values in parentheses). The results presented in Table 10 have been obtained with the LO PDF and LO gluon shadowing (EPS09LO [62] and HKN07LO [63]) and with NLO parametrizations of the shadowing (EPS09NLO [62], HKN07NLO [63] and nCTEQ15 [13]). The nuclear gluon shadowing has a substantial impact on the the UPC $\Upsilon(1S)$ photoproduction in PbPb collisions. In case of CTEQ6L1 [64] gluon PDF the cross-section is reduced by 46% and 40% for EPS09LO and HKN07LO gluon shadowing respectively. The cross-section obtained with CTEQ6M [64] free gluon PDF shows 40%, 39% and 58% reduction respectively for EPS09NLO, HKN07NLO and nCTEQ15 parametrizations. The cross-section evaluated in the presented analysis strongly disfavours results obtained without the gluon shadowing effect. The results for the LO gluon shadowing are also inconsistent with the experimental result. In the case of the NLO gluon shadowing parametrizations, on the other hand, all the results are consistent within the uncertainties with the value obtained in the analysis. All the results together with the cross-section obtained in this analysis are presented in Fig. 68.

Table 10: Table presents results for for models without and with various parametrizations of the nuclear gluon shadowing. Cross section of UPC photoproduction of the $\Upsilon(1S)$ meson in PbPb collisions at $\sqrt{s_{NN}} = 5.02$ TeV are presented. The results are obtained for the CMS rapidity range and the values in parentheses are normalised to the full kinematic range based on a factor obtained from STARLIGHT MC. [61]

Param.	Gluon shadowing σ[μb]			
	w/o shad.	EPS09LO	HKN07LO	
CTEQ6L1	166 (200)	89 (107)	99 (119)	
	w/o shad.	EPS09NLO	HKN07NLO	nCTEQ15
CTEQ6M	62 (75)	37 (45)	38 (46)	26 (31)

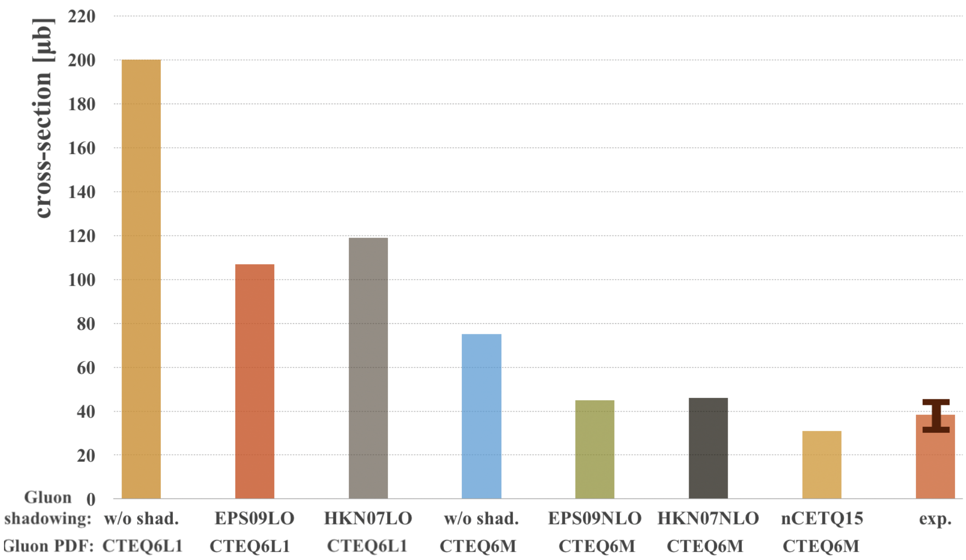

Figure 68: Result of the cross-section $\sigma_{\mathrm{PbPb}\to\Upsilon(1S),\mathrm{coh}}$ obtained in the presented analysis with the total uncertainty together with predictions evaluated for models with various parametrizations, as described in the text.

5.3 Summary

Because of our poor understanding of the nuclear PDFs at a kinematic range of low x and Q^2 there is a great need for results probing this area. This problem can be addressed with the result of the cross-section for the UPC photoproduction of vector mesons. This measurement has been done for J/ψ meson at $\sqrt{s_{NN}} = 2.76$ TeV with CMS PbPb data [50]. In the this analysis the obtained cross-section has been compared against the theoretical predictions and occured to be in a good agreement with model containing effective contribution from the nuclear gluon shadowing. The measurement obtained in the analysis presented in this thesis, presents the first result for the UPC photoproduction of the Υ(1S) meson in PbPb collisions. It strongly disfavours models without nuclear gluon shadowing effect and is consistent with models at the nuclear gluon shadowing effect at NLO. This result constrains theoretical predictions over a new kinematic range, at higher energies and therefore leads to better understanding of the initial state of relativistic nuclei, the nature of nuclear matter and the quantum chromodynamics. An accurate model of the initial heavy-ion state could distinguish QGP effects from those already present in the nuclei. The presented result provides a foundation for future investigations of strongly interacting matter and broaden our understanding of heavy-ion interactions.

For the High Luminosity LHC phase[65], which is planned to start operating at the end of 2027, the CMS experiment has requested an integrated luminosity of 10 to 13 nb^{-1} for the PbPb run at 5.5 TeV. Having larger sample sizes will enable further UPC analyses with substantially reduced statistical uncertainties. In particular a measurement of the coherent UPC photoproduction of the Υ(1S) in rapidity bins with high precision will be possible for the first time. Also higher states, Υ(2S) and Υ(3S) may be measured with the increased data samples.

Acknowledgements

I would like to express my gratitude to my supervisor dr hab. Artur Kalinowski and fellow scientists form the CMS group from the University of Warsaw and Nuclear Centre for Nuclear Research for their hard questions and insightful comments. Special thanks goes to dr hab. Grzegorz Brona, who introduced me to the Heavy-Ion Forward group in CMS. I would also like to thank the group from the Kansas University, where I spent 2 semesters during my PhD studies. Prof. Daniel Tapia Takaki and Prof. Micheal Murray, thank you for this fruitful trips. I am also thankful to other physicists from the CMS collaboration for excellent performance of the experiment and all the suggestions during countless meetings.

My sincere thanks also goes to my friends dr Stanisław Gałęski, dr Michał Olszewski and dr Krzysztof Sielewicz. Thank you for your encouragement and programming tricks.

Last but not the least, I would like to thank my family and my girlfriend for the commitment to my education and all the support during tough moments.

This work was supported by National Science Centre (Poland) grants 2015/19/N/ST2/02697 and 2018/28/T/ST2/00199.

Appendices

A The photon flux on the target nucleus

In order to obtain the photon flux on the target nucleus it is only needed to consider projectile's electromagnetic field E' at the position of the target nucleus. In the projectile's reference frame the position of the target nucleus has coordinates given by

$$x' = -vt', \quad y' = b, \quad z' = 0, \tag{21}$$

where v is velocity between the nuclei and t' is time, the impact parameter b is the distance between centers of nuclei at closest approach. The electric field in that frame of reference is given by:

$$\vec{\mathbf{E}}' = \left(\frac{eZ}{4\pi\epsilon_0 \left((-vt')^2 + b^2 \right)^{3/2}} \right) \left(-vt'\hat{\mathbf{x}}' + b\hat{\mathbf{y}}' \right), \tag{22}$$

where Z is the electric charge of the photon emitting nuclei, e is the fundamental charge and ϵ_0 is the electric constant. There is no magnetic field B because the projectile is at rest and z coordinate can be ignored what simplifies the equation to two dimensions. The field equations can be converted to target's unprimed frame of reference by Lorentz transformations:

$$\begin{aligned} E'_x = E_x, \quad \gamma \left(E'_y/c + \beta B'_z \right) = E_y/c, \quad \gamma \left(E'_z/c + \beta B'_y \right) = E_z/c, \\ B'_x = B_x, \quad \gamma \left(B'_y + \beta E'_z/c \right) = B_y/c, \quad \gamma \left(B'_z + \beta E'_y/c \right) = B_z, \end{aligned} \tag{23}$$

where the Lorentz factor $\gamma = c/\sqrt{c^2 - v^2}$ and $\beta = v/c$. This transformation reduces to:

$$\begin{aligned} E'_x = E_x, \quad \gamma E'_y = E_y, \quad \gamma\beta E'_y/c = B_z, \\ ct' = \gamma ct, \quad x' = -\gamma\beta ct. \end{aligned} \tag{24}$$

The electric and magnetic fields in target nuclei reference frame are then given by:

$$\vec{\mathbf{E}} = \left(\frac{\gamma e Z}{4\pi\epsilon_0 \left((\gamma v t)^2 + b^2 \right)^{3/2}} \right) (vt\hat{\mathbf{x}} + b\hat{\mathbf{y}}) ,$$
$$\vec{\mathbf{B}} = \frac{\gamma \beta e Z b}{4\pi c\epsilon_0 \left((\gamma v t)^2 + b^2 \right)^{3/2}} \hat{\mathbf{z}} = \frac{\gamma \mu_0 v e Z b}{4\pi \left((\gamma v t)^2 + b^2 \right)^{3/2}} \hat{\mathbf{z}}, \tag{25}$$

where μ_0 is the magnetic constant. When nuclei are moving head-on the impact parameter $b = 0$ and there is a factor of γ^2 in the denominator. On the other hand, when vt goes to zero there is γ factor in the numerator, i.e. for the y direction there is a factor of γ^3 higher compared to the x direction (see Fig. 69). The electric field is compressed in the direction of the boost – at ultra-relativistic velocities charged particles produce strong electric field in the plane transverse with respect to the direction of the motion.

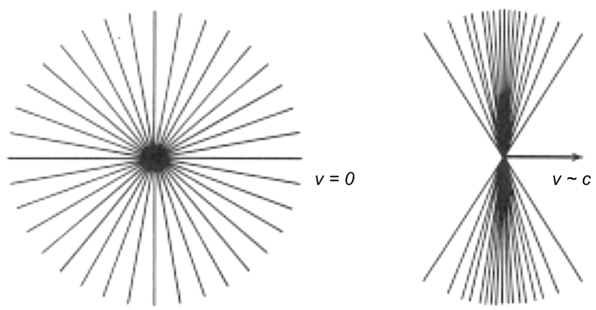

Figure 69: The electric field of charged particle at rest (left) and moving with velocity, v close to the speed of light, c (right).

The electromagnetic fields can be separated into odd and even functions of time, what simplifies the decomposition of the equations into Fourier frequency modes. The odd function decompose into sine functions while even functions decompose into cosine functions. The Fourier transformation integrals are given by:

$$
\begin{aligned}
E_x(\omega) &= \sqrt{\frac{2}{\pi}}\frac{eZ}{4\pi\epsilon_0 b^2}\int_0^\infty \frac{(\gamma vt/b)\sin(\omega t)}{((\gamma vt/b)^2+1)^{3/2}}dt,\\
E_y(\omega) &= \sqrt{\frac{2}{\pi}}\frac{\gamma eZ}{4\pi\epsilon_0 b^2}\int_0^\infty \frac{\cos(\omega t)}{((\gamma vt/b)^2+1)^{3/2}}dt,\\
B_z(\omega) &= \frac{\beta E_y(\omega)}{c}.
\end{aligned}
\tag{26}
$$

The solutions to these integrals are:

$$
\begin{gathered}
u=\frac{\gamma vt}{b},\quad du\left(\frac{b}{\gamma v}\right)=dt,\quad \omega'=\frac{\omega b}{\gamma v},\\
\int_0^\infty \frac{u\sin(\omega' u)}{(u^2+1)^{3/2}}du=\omega' K_0(\omega'),\qquad \int_0^\infty \frac{\cos(\omega' u)}{(u^2+1)^{3/2}}du=\omega' K_1(\omega').
\end{gathered}
\tag{27}
$$

In equation 27 the photon energy can be given by $\hbar\omega$. The x and y components of the electric field are given in terms of ω by:

$$
\begin{aligned}
E_x(\omega) &= \sqrt{\frac{2}{\pi}}\frac{eZ}{4\pi\epsilon_0 b^2}\frac{b}{\gamma v}\frac{\omega b}{\gamma v}K_0\left(\frac{\omega b}{\gamma v}\right),\\
E_y(\omega) &= \sqrt{\frac{2}{\pi}}\frac{\gamma eZ}{4\pi\epsilon_0 b^2}\frac{b}{\gamma v}\frac{\omega b}{\gamma v}K_1\left(\frac{\omega b}{\gamma v}\right).
\end{aligned}
\tag{28}
$$

Since in equation 28 there is an additional factor of γ in the E_y component relative to E_x for $\gamma \gg 1$ the x component of electric field can be neglected. For ultra-relativistic velocities $\beta \approx 1$ and $E_y/c \approx B_z$. Additionally $E_y \approx \gamma E_x$ because $K_0(x)$ is smaller than $K_a(x)$ for all x. In the ultra-relativistic limit:

$$
\gamma \gg 1 \Rightarrow \gamma E_x \gg E_x \Rightarrow E_y \gg E_x. \tag{29}
$$

In this limit the field components reduce to one electric and one magnetic component that are perpendicular to each other. This configuration is identical to a plane wave. The energy of the field per area per time is given by the Poynting vector, which takes a form

$$\vec{\mathbf{S}} \equiv \vec{\mathbf{E}} \times \vec{\mathbf{B}}/\mu_0 = (E_y^2/c\mu_0)\hat{\mathbf{x}} = c\epsilon_0 E_y^2 \hat{\mathbf{x}}. \tag{30}$$

The energy per unit area (fluence) is given by:

$$I(b) = \hat{\mathbf{x}} \cdot \int_0^\infty \vec{\mathbf{S}} d\omega = \int_0^\infty (c\epsilon_0 E_y^2) d\omega = \int_0^\infty \left(\frac{dI}{d\omega}\right) d\omega, \tag{31}$$

and the differential of fluence with respect to ω (spectral fluence) takes the form:

$$\begin{aligned} \frac{dI}{d\omega} = c\epsilon_0 E_y^2 = \frac{e^2 Z^2 c}{4\pi^3 b^2 v^2 \epsilon_0} \left(\frac{\omega b}{\gamma v}\right)^2 K_1^2 \left(\frac{\omega b}{\gamma v}\right) = \\ = \alpha\hbar \left(\frac{Z}{b\beta\pi}\right)^2 \left(\frac{\omega b}{\gamma v}\right)^2 K_1^2 \left(\frac{\omega b}{\gamma v}\right). \end{aligned} \tag{32}$$

The spectral fluence is related to the quantum mechanical formula for the energy of the photon, $E = \hbar\omega$. The relation between the spectral fluence and photon number density is:

$$\frac{dI}{d\omega} d\omega = \hbar\omega N(\omega) d(\hbar\omega) \Rightarrow \frac{1}{\hbar^2 \omega} \frac{dI}{d\omega} = N(\omega). \tag{33}$$

By substituting the equations 32 and 33 the semi-classical formula for the photon flux is obtained:

$$N(\omega, b) = \frac{\alpha}{\hbar\omega} \left(\frac{Z}{b\beta\pi}\right)^2 \left(\frac{\omega b}{\gamma v}\right)^2 K_1^2 \left(\frac{\omega b}{\gamma v}\right). \tag{34}$$

References

[1] M. Tanabashi et al. (Particle Data Group), Review of Particle Physics, Phys. Rev. D 98, 030001, 2019

[2] M. Thomson, Modern Particle Physics, Cambridge University Press, 2013

[3] M. Gell-Mann, A Schematic Model of Baryons and Mesons, Physics Letters, 1964

[4] G. Zweig, An SU(3) Model for Strong Interaction Symmetry and its Breaking, CERN-TH-401, 1964

[5] M. Tanabashi et al., Particle Data Group, Phys. Rev. D 98, 030001, 2018

[6] V. E. Barnes; et al., Observation of a Hyperon with Strangeness Minus Three, Physical Review Letters. 12 (8): 204, 1964

[7] D. Perkins, Introduction to High Energy Physics, Cambridge University Press; 4 edition, 2000

[8] R. P. Feynman, The Behavior of Hadron Collisions at Extreme Energies High Energy Collisions: Third International Conference at Stony Brook, 1969

[9] A. D. Martin, Proton structure Partons, QCD, DGLAP and beyond, Acta Phys.Polon.B39:2025-2062, 2008

[10] B. Badelek, Experimental results on nucleon structure, Summer school lectures, Nuclear Physics Summer School at Stony Brook University, July 2013

[11] H. Paukkunen, Nuclear PDFs Today, Talk given in the Hard Probes 2018 conference, arXiv:1811.01976, 2018

[12] Kari J. Eskola Petja Paakkinen, Hannu Paukkunen, Carlos A. Salgado, EPPS16: Nuclear parton distributions with LHC data, arXiv:1612.05741, 2016

[13] K. Kovarik et al, nCTEQ15 - Global analysis of nuclear parton distributions with uncertainties in the CTEQ framework, Phys. Rev. D 93, 2016

[14] D. de Florian, R. Sassot, P. Zurita and M. Stratmann, Global analysis of nuclear parton distributions, Phys. Rev. D 85, 2012

[15] ALICE Collaboration, Coherent J/ψ photoproduction in ultra-peripheral Pb-Pb collisions at $\sqrt{s_{NN}}$=2.76TeV. Phys.Lett., B718:1273–1283, 2013

[16] V. Guzey, E. Kryshen, M. Strikman, and M. Zhalov. Evidence for nuclear gluon shadowing from the ALICE measurements of PbPb ultraperipheral exclusive J/ψ production. Phys.Lett., B726:290–295, 2013

[17] C. von Weizsäcker, Radiation emitted in collisions of very fast electrons, Z.Phys. 88 612–625, 1934

[18] E. Williams, Nature of the high-energy particles of penetrating radiation and status of ionization and radiation formulae, Phys.Rev. 45 729–730, 1934

[19] A.J. Baltz, G. Baur, D. d'Enterria, L. Frankfurt, F. Gelis, et al. The Physics of Ultraperipheral Collisions at the LHC. Phys.Rept., 458:1–171, 2008

[20] J.G. Contreras and J.D. Tapia Takaki. Ultra-peripheral heavy-ion collisions at the LHC. Int.J.Mod.Phys., A30(08):1542012, 2015

[21] LHC Machine, Lyndon Evans and Philip Bryant 2008 JINST 3 S08001

[22] K. Huübner, Designing and Building LEP, Phys.Rep. 403-404 177-188, 2004

[23] Accelerators at CERN, `https://home.cern/science/accelerators` access Sep 2020

[24] LHC@Home, `http://lhcathome.web.cern.ch/about` access Sep 2020

[25] The CERN accelerator complex, `https://cds.cern.ch/record/2197559` access Sep 2020

[26] LHC superconducting radio-frequency cavity in the LHC tunnel, `https://cds.cern.ch/record/1077038` access Oct 2020

[27] LHC Images, https://lhc-machine-outreach.web.cern.ch/lhc-machine-outreach/lhc_in_pictures.htm access Oct 2020

[28] G. I. Budker, An effective method of damping particle oscillations in proton and antiproton storage rings, Soviet Atomic Energy. 22 (5): 438–440, 1967

[29] Public CMS Luminosity Information, https://twiki.cern.ch/twiki/bin/view/CMSPublic/LumiPublicResults#Overview access Nov 2020

[30] The CMS Collaboration, The CMS experiment at the CERN LHC, JINST 3 S08004, 2008

[31] The ATLAS Collaboration, The ATLAS Experiment at the CERN LHC, JINST 3 S08003, 2008

[32] The ALICE Collaboration, The ALICE experiment at the CERN LHC, JINST 3 S08002, 2008

[33] LHCb Collaboration, The LHCb Detector at the LHC, JINST 3 S08005, 2008

[34] TOTEM Collaboration, The TOTEM Experiment at the CERN LHC, JINST 3 S08007, 2008

[35] LHCf Collaboration, The LHCf detector at the CERN Large Hadron Collider", JINST 3 S08006, 2008

[36] MoEDAL Collaboration, The Physics Programme Of The MoEDAL Experiment At The LHC, Int. J. Mod. Phys. A 29 1430050, 2014

[37] The ATLAS Collaboration, Observation of a new particle in the search for the Standard Model Higgs boson with the ATLAS detector at the LHC, Physics Letters B. 716 1–29, 2012

[38] The CMS Collaboration, Observation of a new boson at a mass of 125 GeV with the CMS experiment at the LHC, Physics Letters B. 716 30–61, 2012

[39] R. R. Wilson. The Tevatron, Fermilab, FERMILAB-TM-0763, 1978

[40] Superconducting Magnet, http://cms.web.cern.ch/news/superconducting-magnet, access: Nov 2020

[41] The CMS Collaboration , Description and performance of track and primary-vertex reconstruction with the CMS tracker, JINST, 9 P10009, 2014

[42] M. Ressegotti, Overview of the CMS detector performance at LHC Run 2, CMS-CR-2018-383, http://cds.cern.ch/record/2649417

[43] A. Benaglia, The CMS ECAL performance with examples, JINST 9 C02008, 2014

[44] The CMS Collaboration, CMS TECHNICAL DESIGN REPORT FOR THE LEVEL-1 TRIGGER UPGRADE, https://cds.cern.ch/record/1556311, access: Nov 2020

[45] The CMS Collaboration, Particle-flow reconstruction and global event description with the CMS detector, JINST 82 P10003, 2017

[46] M. Cacciari, G. P. Salam, G. Soyez, The anti-kt jet clustering algorithm, JHEP 04 063, 2008

[47] The CMS Collaboration, Measurement of exclusive ϒ photoproduction from protons in pPb collisions at $\sqrt{s_{NN}} = 5.02$ TeV, Eur. Phys. J. C 79, 277, 2019

[48] S.R. Klein, J. Nystrand, J. Seger, Y. Gorbunov, J. Butterworth, STARlight: A Monte Carlo simulation program for ultra-peripheral collisions of relativistic ions, Comp. Phys. Comm. 212 (2017) 258

[49] P. Jones, D. Martin, M. G. Ryskin, and T. Teubner, Probes of the small x gluon via exclusive J/ψ and ϒ production at HERA and LHC, JHEP 11 085, 2013

[50] The CMS Collaboration, Coherent J/ψ photoproduction in ultra-peripheral PbPb collisions at $\sqrt{s_{NN}} = 2.76$ TeV with the CMS experiment, Phys. Lett. B 772, 2017

[51] T. Bauer, R. Spital, D. Yennie, and F. Pipkin, The Hadronic Properties of the Photon in High-Energy Interactions, Rev. of Modern Physics 50(2), 1978

[52] M. L. Miller, K. Reygers, S. J. Sanders, and P. Steinberg, Glauber modeling in high energy nuclear collisions, Ann.Rev.Nucl.Part.Sci. 57 205–243, 2007

[53] J. Alwall, A. Ballestrero, P. Bartalini, S. Belov, E. Boos, et al., A Standard format for Les Houches event files, Comput.Phys.Commun. 176 300–304, 2007

[54] J. Allison et al., Geant4 developments and applications, Nuclear Science, IEEE Transactions on 53 no. 1, 270–278, 2006

[55] R. Brun and F. Rademakers, ROOT - An Object Oriented Data Analysis Framework, Proceedings AIHENP'96 Workshop, Lausanne, Sep. 1996, Nucl. Inst. and Meth. in Phys. Res. A 389 81-86, 1997

[56] Worldwide LHC Computing Grid, `https://wlcg.web.cern.ch`, access: Nov 2020

[57] The CMS Collaboration, Description and performance of track and primary-vertex reconstruction with the CMS tracker, JINST 9 P10009, 2014

[58] W. Verkerke and D. P. Kirkby, The RooFit toolkit for data modeling, eConf C0303241 MOLT007, arXiv:physics/0306116, 2003

[59] T. Sjostrand et al, An Introduction to PYTHIA 8.2, Comput. Phys.Commun. 191 159, 2015

[60] Luminosity Physics Object Group, `https://twiki.cern.ch/twiki/bin/viewauth/CMS/TWikiLUM`, access: Feb 2021

[61] Photoproduction of Upsilon in Ultraperipheral Collisions at LHC Run2 energies, arXiv:1711.05999, 2017

[62] E. J. Eskola, H. Paukkunen, and C. A. Salgado, EPS09 — A new generation of NLO and LO nuclear parton distribution functions, JHEP 0904, 065, 2009

[63] M. Hirai et al., Determination of nuclear parton distribution functions and their uncertainties at next-to-leading order, Phys. Rev. C 76, 065207, 2007

[64] J. Pumplin et al., New Generation of Parton Distributions with Uncertainties from Global QCD Analysis, JHEP 07, 012, 2002

[65] G. Apollinari et al., High-Luminosity Large Hadron Collider (HL-LHC): Technical Design Report, CERN Yellow Reports: Monographs, 2017